Laser-Induced Thermal Acoustics: Simultaneous Velocimetry and Thermometry for the Study of Compressible Flows

A thesis accepted by the Faculty of Aerospace Engineering and Geodesy
of the University of Stuttgart in partial fulfilment of the requirements
for the degree of Doctor of Engineering Sciences (Dr.-Ing.)

by

Dipl.-Ing. Felix Johannes Förster

born in Karlsruhe, Germany

main referee: Prof. Dr.-Ing. habil. Bernhard Weigand
co-referee: Prof. Dr.-Ing. Stephan Staudacher
Date of defence: 11th of July 2016

Institute of Aerospace Thermodynamics
University of Stuttgart
2016

Acknowledgments

This thesis results from my time as a research associate at the Institute of Aerospace Thermodynamics (ITLR) at the University of Stuttgart and as a graduate in the Research Training Group GRK 1095 'Aero-Thermodynamic Design of a Scramjet Propulsion System for Future Space Transportation Systems'. The financial support by the German Research Foundation (Deutsche Forschungsgemeinschaft) through this project is gratefully acknowledged.

Firstly, I want to thank Prof. Dr.-Ing. habil. Bernhard Weigand for raising my interest and giving me the opportunity for this work. This thesis benefited greatly from both his superb counsel and supportive nature. It was a constant source of motivation and expertise. I am grateful for his effort not only as my supervisor, but also in his role as the head of the graduate school and as the director of the institute. Furthermore, my gratitude belongs to Prof. Dr.-Ing. Stephan Staudacher for his interest and help. I sincerely enjoyed our discussions throughout the project and am thankful to him for becoming my co-referee. Likewise, I thank Prof. Dr.-Ing. Jens von Wolfersdorf and Dr.-Ing. Grazia Lamanna for the numerous discussions on all aspects of engineering science at the expense of their own valuable time.

No project is carried out in isolation and so I would like to say thanks to my former colleagues – many of them became friends – who generated the positive and productive work atmosphere at ITLR and made my time there unforgettable. I owe special gratitude first of all to my great team mate in the scramjet group, Nils Dröske. He has always been unfailingly cheerful and keen to discuss any problem (challenge) – be it of scientific, technical, administrative or human nature. To me, his opinion was always valuable and in all my time at the ITLR, he proved to be a true ally in facing the ups and downs associated with an experimental thesis at the combustion test facility. Furthermore, I want to thank Steffen Baab for his enterprising spirit that is far from common. Working together was an excellent example for what is possible by persistency in the presence of seemingly unending obstacles. It was hard, exhausting, but fruitful - and ultimately very satisfactory. Likewise, I am thankful for the joint project with Stefan Brack. It was a great opportunity to work in a research field different from my own, and this diversity made work a lot more pleasant. Little did we know at the time in which ways these ideas would become successful.

Special thanks belong to my predecessor Annika Hell who taught me the very peculiar features of the test facility and the LITA system. I would also want to thank her for all the pleasant conversations we had over the years that we were sharing an office.

As any experimentalist, I owe much to the excellent support given by the colleagues in the workshops at ITLR. Running the test facility and fixing broken components (all too often a mere result of running the facility and a frequent source of frustration) was only possible through the constant commitment of Eberhard Mayer and Dennis Nehring as well as the other members of the mechanical workshop: Jürgen Fauser, Olaf Ordner, Atilla Lomlu and Christian Otto. For the same dedication, I want to thank Uli Schwaderer and Thomas Bertnik of the electrical workshop. Their fast and reliable support that included fixing seemingly any piece of electrical equipment – from off-the-shelf desktop computers to cutting-edge measurement devices – is essential for this kind of research. The same gratitude I owe to Birgit Panzer and to Susanne Stegmeier for their support in administrative matters, for teaching me patiently the intricate details of claiming travel expenses and ordering formalities as well as the secrets of bureaucracy in general.

Finally, my deepest gratitude belongs to my family. Their unconditional support throughout my life was essential for me becoming what I am today. I admire their patience over the last five years leading to this thesis, especially during the stressful time of finalizing this thesis. Special thanks I owe to my Dad for patiently proof-reading draft after draft of this thesis.

Karlsruhe, December 2016
Felix Johannes Förster

Contents

List of Figures

List of Tables

List of Symbols

Latin Characters

Symbol	Description	Unit
a	speed of sound	$\mathrm{m\,s^{-1}}$
A	area	$\mathrm{m^2}$
c	speed of light	$\mathrm{m\,s^{-1}}$
D	diameter	m
D_T	thermal diffusivity	$\mathrm{m^2\,s^{-1}}$
f	1.) focal length	m
	2.) degrees of freedom	–
I	signal intensity	a.u.
I_{sp}	specific impulse	s
h	radius of measurement volume	m
$\boldsymbol{k}$	wave vector	–
l	length of measurement volume	m
$\dot{m}$	mass flow	$\mathrm{kg\,s^{-1}}$
M	Mach number	–
N	number of fringes	–
p	pressure	Pa
P_{xx}	power spectral density	a.u.
$\boldsymbol{q}$	grating vector	–
r	recovery factor	–
R	1.) radius	m
	2.) specific gas constant	$\mathrm{J(kgK)^{-1}}$

Symbol	Description	Unit
T	temperature	K
$\mathcal{U}_E$	electrostrictive grating amplitude	–
$\mathcal{U}_T$	thermal grating amplitude	–
v	velocity	$\mathrm{m\,s^{-1}}$
X, Y, Z	axes of a Cartesian coordinate system	m

Greek Characters

Symbol	Description	Unit
Δ	absolute deviation	a.u.
β	shock angle	rad
δ	relative deviation	–
η	beam misalignment	m
γ	ratio of specific heats	–
γ_T	thermalization rate	Hz
Γ	acoustic damping rate	$\mathrm{m^2\,s^{-1}}$
λ	wavelength of laser beam	m
Λ	fringe space	m
ν	frequency of the laser light	Hz
$\nu(M)$	Prandtl–Meyer function	–
Ω	beat frequency	Hz
φ	intersection angle of the interrogation beam	rad
ϕ	phase of electromagnatic wave	rad
Φ	fuel injection ratio: $\frac{\dot{m}_{H_2}/\dot{m}_{O_2}}{\left(\dot{m}_{H_2}/\dot{m}_{O_2}\right)_{\text{stoichiometric}}}$	–
ρ	density	$\mathrm{kg\,m^{-3}}$
τ	pulse duration	s

Symbol	Description	Unit
θ	1.) deflection angle	rad
	2.) crossing angle of the excitation beams	rad
Θ	temperature ratio	–

Subscripts

Symbol	Description
∞	ambient conditions
exc	denotes the excitation beam
$exit$	exit conditions
exp	experimental value
int	denotes the interrogation beam
ref	denotes reference beam
s	incident shock wave
sig	denotes signal beam
st	static conditons
t	stagnation conditions
th	theoretical value derived from the shock wave theory

Abbreviations

Abbrevation	Description
CARS	Coherent Anti-Stokes Raman Spectroscopy
CFD	Computational Fluid Dynamics
CL	Confidence Level
DFG	Deutsche Forschungsgemeinschaft (German research foundation)
DFWM	Degenerate Four-Wave Mixing
DLR	Deutsches Zentrum für Luft– und Raumfahrt (German aerospace center)
DPSS	Diode Pumped Solid State (laser)

Abbrevation	Description
FFT	Fast Fourier Transform
GIP	Gas Induced Particles
GRK	Graduiertenkolleg (Research training group)
HIFiRE	Hypersonic international Flight Research Experimentation program
HyCAUSE	Hypersonic Collaborative Australia/United States Experiment
ITLR	Institut für Thermodynamik der Luft- und Raumfahrt (Institute of Aerospace Thermodynamics)
JAPHAR	Joint Air-breathing Propulsion for Hypersonic Application Research
LDA	Laser Doppler Anemometry
LIF	Laser-Induced Fluorescence
LITA	Laser-Induced Thermal Acoustics
NASA	National Aeronautics and Space Administration
Nd:YAG	Neodymium-doped Yttrium Aluminium Garnet: crystal that is used as a laser medium in solid-state lasers
NIST	National Institute of Standards and Technology
ONERA	Office National d'Études et de Recherches Aérospatiale (French aerospace lab)
OpenFOAM	Open source Field Operation And Manipulation: open source software for computational fluid dynamics
PIV	Particle Image Velocimetry
PREPHA	Programme de Recherche sur la Propulsion Hypersonique Avancée (Research and technology program for advanced hypersonic propulsion)
RANS	Reynolds-Averaged Navier-Stokes (equations)
RefProp	Reference Fluid Thermodynamic and Transport Properties Database
TDLAS	Tunable Diode Laser Absorption Spectroscopy

Abstract

Fast transportation of passengers and cargo to any destination on the globe and even into space is a major achievement of mankind. Its future development will heavily depend on faster and economically as well as ecologically more efficient transportation concepts. Air-breathing propulsion concepts, such as scramjets, provide a promising alternative to conventional systems. With this technology flight vehicles could travel at multiples of the speed of sound, which offers a great potential in the spread of products around the globe. Furthermore, the integration of scramjet engines in space transportation systems is an important supplement to existing rocket-based systems in order to increase the payload and reduce operational costs.

The development of a scramjet engine is, however, challenging and involves the knowledge of many disciplines. One of the most critical problems is a stable and reliable combustion. Experimental investigations significantly contribute to the required understanding of the underlying aerodynamics and combustion mechanisms. Furthermore, quantitative experimental data sets are vital for the validation of numerical simulations, which became an important supplement in today's design and optimization processes. Their advancement also pushes the development of new diagnostic methods to provide more sophisticated experimental data sets.

The flows relevant to this thesis are characterized by high speeds, high temperatures and chemical reactions. Obtaining quantitative data of such a flow field, sufficiently resolved in time and space, is a difficult task for any measurement technique. Laser-Induced Thermal Acoustics (LITA) is seen as a promising diagnostic tool to overcome these problems. Hence, the focus of this thesis is the development, evaluation and application of LITA for the study of compressible flows.

LITA allows non-intrusive and remote measurements of multiple flow quantities that are spatially and temporally resolved. With the setup developed in this thesis, speed of sound, flow velocity, Mach number and – for known gas compositions – temperature are derived from a single measurement. A thorough validation of the setup was conducted to establish the performance of the technique for reference cases at flow conditions comparable to the intended application. Even for the harsh environmental conditions at the combustion test facility, it is verified that very accurate and detailed data sets can be obtained with LITA.

Finally, the validated technique was used in three different applications. In the first case, time-resolved speed of sound, flow velocity and Mach number measurements were conducted in the reaction zone of a chemically reacting H_2/air free jet. Flow profiles were obtained at different axial positions downstream of the nozzle exit, thus showing the evolution of the combustion zone. This was consistent with the dimensions visible in OH^*-chemiluminescence images. Subsonic combustion was proven for the experiment via LITA velocimetry.

The second application is dedicated to the flow field inside scramjet combustor models. Detailed experimental data sets were provided for the validation of an advanced OpenFOAM solver developed at ITLR. In addition, a precise reconstruction of the flow field and the shock system resulting from a jet injected into the supersonic cross flow was possible. Finally, LITA was successfully applied to the scramjet combustor for inlet conditions as required in a combustion experiment.

The last application explored the potential of LITA for shock tube experiments. Measurements were successfully conducted behind the incident and reflected shock wave. Several experiments at different pressures and temperatures were performed to provide a reasonable variation in experimental conditions for the assessment of LITA for shock-heated flows. Furthermore, it allowed to investigate the dependency of the LITA signal intensity on temperature and pressure. The relationship derived here allows to estimate the performance of the LITA system for the expected conditions in future experiments.

Kurzzusammenfassung

Menschen und Güter schnell zu jedem Punkt der Erde und sogar in den Weltraum zu transportieren, ist eine große Leistung der Menschheit. Die weitere Entwicklung wird maßgeblich von schnelleren und ökonomisch sowie ökologisch effizienteren Antriebssytemen abhängen. Luftatmende Staustrahltriebwerke sind eine vielversprechende Alternative zu konventionellen Lösungen. Mit dieser Technologie ausgerüstete Fluggeräte könnten mit einem Vielfachen der Schallgeschwindigkeit fliegen, was die Verbreitung von Gütern rund um den Globus erleichtert. Zudem wäre die Integration von Staustrahlantrieben in Raumtransportsysteme eine wichtige Ergänzung zur existierenden Raketentechnologie, welche die Nutzlast erhöhen und dadurch die Kosten reduzieren würde.

Die Entwicklung von Staustrahlantrieben mit Überschallverbrennung ist jedoch schwierig und erfordert das Wissen vieler Fachgebiete. Eines der kritischsten Probleme ist die Realisierung einer stabilen und zuverlässigen Verbrennung. Experimentelle Untersuchungen helfen dabei, das benötigte Verständnis der zugrundliegenden aerodynamischen und verbrennungstechnischen Prinzipien zu erlangen. Zusätzlich sind experimentelle Datensätze unerlässlich für die Validierung von numerischen Strömungssimulationen, welche einen zunehmenden Anteil an heutigen Auslegungs- und Optimierungsprozessen haben. Für ihre Weiterentwicklung wird auch neue Messtechnik benötigt, um bessere experimentelle Datensätze zur Verfügung stellen zu können.

Die für diese Arbeit charakteristischen Strömungen zeichnen sich durch hohe Geschwindigkeiten, hohe Temperaturen und den Ablauf chemischer Reaktionen aus. Quantitative Messungen mit ausreichender zeitlicher und räumlicher Auflösung sind für solche Strömungsfelder eine Herausforderung für jede Messtechnik. Laser-induzierte thermische Akustik (LITA) ist eine vielsprechende Messtechnik für solche Anwendungen. Daher ist der Fokus dieser Arbeit die Entwicklung, Validierung und Anwendung dieser Messtechnik mit Hinblick auf kompressible Strömungen.

LITA ermöglicht die berühungslose Messung von mehreren Strömungsgrößen mit hoher räumlicher und zeitlicher Auflösung. Mit Hilfe des in dieser Arbeit aufgebauten Systems lassen sich Schallgeschwindigkeit, Strömungsgeschwindigkeit, Machzahl und – für eine bekannte Gaszusammensetzung – Temperatur mit einer einzigen Messung bestimmen. Eine gründliche Validierung des Aufbaus wurde durchgeführt, um seine Leistungsfähigkeit in Vergleichsfällen mit Strömungsbedingungen ähnlich der späteren Anwendung nachzuweisen. Selbst für die rauen Bedingungen an der Verbrennungsversuchsanlage konnten sehr genaue und umfassende Datensätze mit LITA erzielt werden.

Anschließend wurde die validierte Messmethode für drei Anwendungen eingesetzt. Für die erste Anwendung wurden zeitaufgelöste Messungen der Schallgeschwindigkeit, der Strömungsgeschwindigkeit und der Machzahl in der Verbrennungszone eines reagierenden H_2/Luft-Freistrahls durchgeführt. Strömungsprofile wurden für verschiedene axiale Positionen stromab des Düsenaustritts erstellt, um die Entwicklung der Verbrennungszone darzustellen. Der gefundene Verlauf ist deckungsgleich mit der Größe der Reaktionszone, welche aus OH^*-Chemilumineszenzbildern abgeleitet wurde. Mit Hilfe der LITA Geschwindigkeitsmessung wurde für das Experiment eine Unterschallverbrennung nachgewiesen.

Die Untersuchung der Strömungsfelder in den Versuchskanälen zur Überschallverbrennung stellt die zweite Anwendung dar. Detailierte experimentelle Datensätze wurden zur Validierung eines komplexen, numerischen Lösers verwendet, welcher in OpenFOAM am ITLR entwicklet wurde. Es war möglich, das Strömungsfeld und Stosssystem, welches durch die Einblasung quer zum Überschallströmungsfeld entstand, zu rekonstruieren. Zudem wurde nachgewiesen, dass LITA auch in der Brennkammer für Versuchbedingungen, die einem Verbrennungsexperiment entsprechen, erfolgreich angewendet werden kann.

Im letzte Anwendungsfall wurde das Potenzial von LITA für Stossrohrversuche untersucht. Messungen wurden erfolgreich hinter der einfallenden und reflektierten Stosswelle durchgeführt. Mehrere Experimente mit verschiedenen Drücken und Temperaturen ergaben eine ausreichende Variation der Versuchsbedindungen, um die Anwendbarkeit von LITA für stossgeheizte Strömungen eindeutig nachzuweisen. Zudem erlaubten die Experimente, die Abhängigkeit der Signalstärke von Druck und Temperatur zu untersuchen. Die gefundene Beziehung kann zum Abschätzen der zu erwartenden Signalstärke für künftige Experimente verwendet werden.

CHAPTER 1

Introduction

The focus of this thesis is the development, evaluation and application of the optical diagnostic technique LITA for supersonic flow research. This objective is motivated and initiated by the development of an air-breathing propulsion system for high-speed civil transport vehicles and new access-to-space concepts.

In this chapter, the development process of such a propulsion system is addressed together with an overview of the diagnostic methods used to accomplish this task. Firstly, the air-breathing engine types are introduced and their conceptional advantages and constraints are discussed. An overview of past and present research projects is provided to set the research training group GRK 1095 – which was the framework for the present thesis – into perspective to worldwide activities in this field. The second part is dedicated to established diagnostic techniques and their application for combustion experiments. On this basis, the motivation and objectives for this thesis are derived.

1.1 Air-breathing Propulsion Concepts

Since the beginning of the last century, civil aviation continues to shrink the planet by transporting passengers and cargo fast to any destination on the globe. This worldwide exchange of people and goods is the foundation of the globalized market as we know it today. Its future development will heavily depend on faster and economically as well as ecologically more efficient concepts. A milestone within this process and in the history of mankind was reached when flight vehicles were no longer restricted to the planet's atmosphere, but able to cross the edge of space. The ability to bring satellites into the earth's orbit is the key for many modern technologies – including communication, navigation or weather observation – that affect our daily life.

Air-breathing propulsion concepts provide a promising and economical alternative to conventional systems. Flying at multiples of the speed of sound offers a great potential in the spread of products around the globe and as an important supplement to existing space transportation system. Conventional space launch vehicles such as Ariane 5 or Delta IV rely on expendable and, hence, expensive rocket driven systems. Here, the payload takes only a mere fraction (≈ 2 %) of the gross weight at launch. For comparison, sixty percent of the total mass is reserved for the oxidizer and its tanks [67]. Instead of carrying the oxidizer along for the entire ascent, air-breathing engines would consume the oxygen in the surrounding atmosphere for the first part of the trajectory, before the flight vehicle switches to rocket propulsion as the edge of space is reached. Such an approach would reduce the gross launch weight and result in an increased payload. Both effects improve the economical efficiency of the launch vehicle. This potential can be quantified by the specific impulse I_{sp} which is the available thrust normalized by the amount of fuel consumed. Hence, I_{sp} describes the efficiency of a propulsion system in terms of fuel required for the generation of a given momentum. Figure 1.1 shows a comparison between different air-breathing engines and conventional rockets. Figure 1.1 leads to two conclusions. Firstly, it shows the advantage of air-breathing engines in terms of specific impulse. Secondly, an air-breathing propulsion system will consist of several engines operated in sequence. Instead, a single engine can be used for the rocket-propelled vehicle over the entire Mach number regime.

A multi-engine concept would include a turbojet to accelerate from zero velocity to approximately Mach 3, followed firstly by a ramjet up to Mach 6 and then

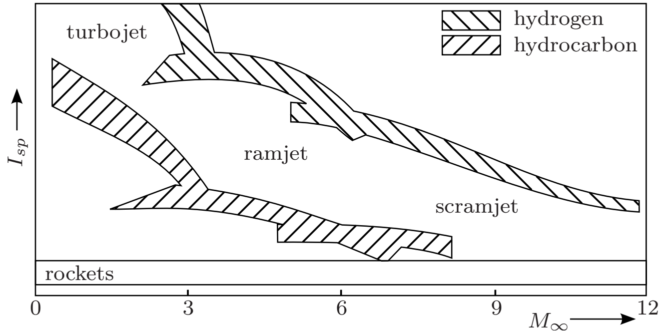

Figure 1.1: Specific impulse of different propulsion concepts over flight Mach number (adapted from [156])

by a scramjet engine for hypersonic speeds [23]. For space transportation, a rocket would be the final stage that takes the vehicle to outer space. Following this sequence, the air-breathing components – turbojet, ram- and scramjet – of the propulsion system are described in more detail below.

Turbojet engines use a thermodynamic cycle based on compression, combustion and expansion to partly convert the chemical energy released during combustion into a propelling jet. A turbojet consists of five major components, namely inlet, compressor, combustor, turbine and nozzle [137]. Using rotating machinery, each step in the cycle is performed simultaneously in contrast to the periodic operation of a reciprocation engine.

The inlet accommodates the flow conditions of the incoming air to the requirements of the compressor. Commonly a fixed inlet geometry is used, which represents a compromise between best overall performance and safe operation over the entire flight envelope. Typically, axial compressors are used to increase the pressure level of the incoming air. Several stages, each consisting of a rotor and stator, are put in series to reach the high pressure ratios required for a high thermodynamic cycle efficiency. Compression is achieved by converting rotational kinetic energy of the rotors into internal energy of the air. The required energy is provided by the turbine and transmitted to the compressor by a shaft that connects both components. After compression, the air is fed to the combustion chamber. The heat release through the combustion adds energy to the thermodynamic cycle. The work output of the engine, and ultimately its cycle efficiency, depend on the temperature level that can be reached in the combustor. On the other hand, the maximal temperature is limited by the thermal loads on the combustor walls and subsequent components. The turbine extracts the rotational energy required to drive the compressors from the internal energy of the hot fluid that comes out of the combustor. Hence, turbines act as exact counterpart to compressors. The last component of a jet engine is the nozzle. The nozzle accelerates the gas flow into a propelling jet that pushes the flight vehicle forward. Ideally, the nozzle expands the gas to ambient pressure, thereby using all the remaining pressure difference. For optimal performance at sub- and supersonic flight speed, a variable exit geometry is required to adapt the nozzle to the respective flight condition.

In summary, thrust is the desired work output for a turbojet. Obviously, losses introduced by any engine component reduce the output and the overall efficiency of the engine. Therefore, the engine is optimized at a design point, usually at cruise condition. At the same time, safe operation must be ensured at any flight conditions. To reach the best compromise becomes more challenging as the flight envelope is stretched to higher flight speed. Additional losses are caused by compressibility effects at the air intake and the exhaust nozzle as result of high flight Mach numbers. Furthermore, the compression of the incoming air causes not only pressure, but also temperature to rise. As high pressure ratios are required for a sufficient cycle efficiency, the thermal loads on the rotating components, that are directly exposed to the gas flow, are significant.

The challenges that result from a pure turbojet engine for supersonic flight are best illustrated using the example of the Olympus 593 engine. Developed to power the Concorde aircraft, this engine was designed to maintain a cruise speed of Mach 2.04. This task required constant afterburner operation, which is one of only two examples in civil aviation. To accommodate for sub- and supersonic flight conditions, the air intake featured a complex systems of moveable ramps and by-pass doors to minimize inlet losses at cruise and ensure a sufficient air flow for take-off. Analogously, the geometry of the exhaust nozzle was adjustable depending on the flight regime and afterburner operation. A high fuel efficiency at cruise was crucial to fulfill the intended payload and range specifications. This set the requirement for a high compression ratio. The resulting thermal loads led to an engine architecture where the blades and disk of the last four compressor stages were already manufactured from high-temperature resistant nickel alloys [136], a material that was normally reserved for turbines at that time. However, these challenges also resulted in an engine design that was at the top of its time – featuring a cycle efficiency of 43 % and thrust output that Sir Stanley Hooker referred to as the “highest thrust of any production turbojet” [88].

At the same time, it gives an impression of the flight speed that can be reached with a pure turbojet propulsion system. Especially the temperatures required for a high cycle efficiency eventually exceed what can be tolerated by the materials. An alternative is to compress the incoming air solely through the vehicle moving at high speed. This offers the advantage to remove those engine components which suffer most from high thermal loads, namely the compressor and the turbine. Such engine concepts are called ram-driven propulsion systems.

Ram-driven engines use the ram effect to compress the fluid prior to combustion – an idea commonly accredited to René Lorin [116]. Instead of an additional mechanical component, a fixed geometry converts the dynamic pressure created by the vehicle’s motion into a higher static pressure. The thermodynamic cycle to describe ram-driven engines is, however, similar to the one of turbojets, as it essentially consists of the same steps, namely compression, combustion and expansion of the gas into a propelling jet. **Ramjet engines** feature a geometric throat in the air intake to decelerate the incoming supersonic flow to subsonic speed. The compression of the gas is achieved by a shock system in the inlet. The shock system is terminated by a normal shock in the throat as illustrated in figure 1.2. This leads to a subsonic flow at the inlet of the combustor. The flow remains subsonic in the combustion process. As the propelling jet must exceed the velocity of a vehicle to produce thrust, the nozzle must accelerate the flow back to supersonic speed. Hence, the engine features a second throat in the exhaust as part of a convergent-divergent nozzle.

Ramjets perform best for flight Mach numbers between 3 to 6. Above Mach 6, viscous and shock-induced losses resulting from the deceleration to subsonic speed in the inlet become a significant penalty. The strong compression also leads to high static temperatures before the combustor, which cause high thermal stresses on the engine structure. In addition, dissociation of the gas consumes parts of the energy intended for thrust production.

The obvious solution is to decelerate the incoming air less if the flight speed exceeds Mach 6. Thereto, the flow must remain supersonic throughout the entire engine including the combustion, which leads to a supersonic combustion ramjet or **scramjet engine**. Since the flow remains supersonic, the divergent part of the nozzle as shown in figure 1.2 is sufficient to accelerate the flow after combustion. Challenges, however, arise from the high speed of the flow inside the combustion chamber, that reduces the available time to mix, ignite and consume the fuel.

Pure ram- and scramjet engines have a narrow flight Mach number range for operation. To extend the range, a so-called **dual-mode scramjet** is suggested. This design features the geometry of a scramjet, but allows ramjet operation at lower Mach numbers. Instead of a physical throat, an oblique shock system referred to as shock-train decelerates the incoming flow to subsonic speed in the isolator (ramjet mode). Sufficient heat release in the combustor causes the subsonic flow to accelerate again and eventually form a thermal throat. Together with the divergent nozzle of the exhaust system, this thermal throat forms a convergent-divergent geometry. This combination allows the gas jet to become supersonic again. In ramjet mode, the shock-train in the inlet is the response of the flow field to the higher back-pressure in the combustion chamber due to the thermal throat. For increasing flight Mach number, this system gets weaker until pure scramjet operation is achieved.

In summary, it must be stressed that neither ram- nor scramjet engines are self-starting. Therefore, it must be a combination of engines to accelerate the

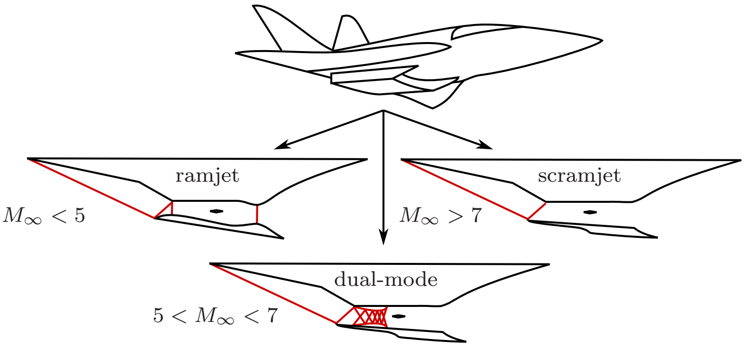

Figure 1.2: Schematic of ramjet and (dual-mode) scramjet engines with characteristic shock structures (red)

ram-driven engine to operational speed either via a turbojet or a rocket. This requires a high level of integration between the propulsion system and the vehicle. Furthermore, the combined engine must accommodate to a wide range of flight conditions including Mach numbers from zero to hypersonic speeds and altitudes from sea level to the top of the atmosphere. Challenges like these were addressed in a number of research programs that were conducted worldwide since the idea of such an engine was first spread.

1.1.1 Selected Past and Present Research Projects

With the end of two world wars, civil research aspects of hypersonic flight gained more importance. To this day, a number of national and international efforts are undertaken to develop a supersonic, air-breathing propulsion system. Fry [54] details the evolution of ram-driven propulsion by providing a comprehensive review of research and technology programs conducted in the last century. Similarly, articles by Waltrup et al. [186] and Curran [22] describe the development of scramjet technology in the United States, Australia, France, Germany, Japan and Russia. More recently, India and China joined the international research community, which shows the enormous scientific and financial effort invested worldwide in hypersonic flight technology. Out of these initiatives, selected research projects are highlighted in the following.

An early conceptional study for a civil, two-stage-to-orbit launch system is the **Sänger II** project initiated as part of the German hypersonic program [87]. In this study, a hypersonic carrier aircraft is intended to carry a second vehicle up to an altitude of approximately 40 km. Both vehicles then separate and only the second stage continues the final ascent to orbit. An air-breathing propulsion system was suggested for the first stage to realize horizontal take-off and landing like a common airplane. The engine was designed to operate in turbojet and ramjet mode to accelerate both stages up to Mach 6.6. A conventional hydrogen-oxygen rocket was selected for the second stage to carry the payload to orbit. The plans for the seconded stage included a manned as well as an unmanned version. A major advantage of the concept was seen in a significant reduction of launch costs as both stages were reusable [102]. Major challenges arose from the aerodynamics in the air inlet system, the thermal loads on the engine components and the overall architecture to integrate both turbo- and ramjet engine into the vehicle. The Sänger II project was terminated in December 1995 together with the German hypersonic program.

The **JAPHAR program** (Joint air-breathing propulsion for hypersonic application research) was started in 1997 as a joint research project between the German and French aerospace centers DLR and ONERA. This cooperation allowed to combine efforts made previously on a national level in the German hypersonic program and its French counterpart PREPHA. The JAPHAR program focused on the feasibility of a hydrogen-fueled dual-mode ramjet engine for a vehicle flying between Mach 4 to 8. This included design studies to integrate the propulsion system in a suitable vehicle [42] as well as extensive ground tests of the engine [38]. The engine features a staged injection via two struts, which was adapted from the configuration studied in the PREPHA project [94]. The results show a transition of the combustion mode from sub- to supersonic combustion depending on the amount of fuel injected and the flight Mach number [38]. The characterization of this dual-mode operation is vital for a realistic prediction of the engine performance at a given flight condition.

Parallel to the activities in Europe, NASA launched the **Hyper-X program** in 1996 to evaluate the potential of air-breathing engines for space transportation systems. Besides conceptional studies and ground testing of components, the program included flight experiments of a dual-mode scramjet demonstrator at Mach 5, 7 and 10 [53]. Here, a B-52 was used as carrier aircraft for the X-43 test vehicle and its booster rocket. At the desired altitude, the demonstrator was dropped and accelerated by the booster rocket before the scramjet engine started operation. Out of three flight experiments, two were successfully conducted in 2004. During the first flight in 2004, the scramjet engine was operational for 11 seconds and accelerated the X-43 vehicle up to Mach 6.8. On the second flight, the test vehicle reached Mach 9.68 – a new record for the X-43 [182]. The flight tests were continued with the X-51 Waverider. At its first flight in 2010, the X-51 maintained a flight velocity of Mach 5 for approximated 210 seconds, which is considered the longest flight time for a dual-mode scramjet-powered vehicle [138]. Two additional flights conducted in 2011 and 2012 failed due to technical problems. These results show the great achievements of the program, but also demonstrate the complexity, costs and challenges associated with such flight experiments.

The **HyShot program** was initiated by the University of Queensland, Australia, and suggested a cost-effective alternative to flight tests launched from a carrier aircraft. The Australian research activities in hypersonic flight has its origin in the work of Ray Stalker and his colleagues, who established impulse facilities for ground testing [160]. This development resulted in the free-piston driven shock tunnel T4, which is capable of simulating flight conditions for scramjet experiments up to orbital velocity [133]. The HyShot program was designed to correlate ground tests in the T4 with actual flight experiments [157]. These flight experiments used a highly ballistic trajectory, where the test vehicle was firstly carried to high altitudes by a rocket. The vehicle then rotated and the scramjet experiments were conducted during the almost vertical re-entry. The use of a commercial single stage rocket reduced launch costs significantly. Challenges, however, arise from the complex re-entry maneuver required for a precise orientation of the test vehicle during descent. The recorded flight data included pressure and temperature measurements as well as the flight state of the vehicle, namely position, velocity and orientation. These flight experiments provided vital data for the comparison of flight and ground tests as well as the evaluation of numerical predictions.

The HyShot program initiated the subsequent programs **HyCAUSE** [185] and **HIFiRe** [92]. Furthermore, the parabolic trajectory was incorporated in related programs such as **Hy-V** [62] and more recently **SCRAMSPACE** [9]. These programs express not solely Australia's ambitions, but are collaborations between Australia and the United States as well as other partner universities and research organizations worldwide.

1.1.2 Research Training Group GRK 1095

The framework of the research conducted for this thesis was the GRK 1095 (Research Training Group). Initiated in 2005 and funded by the German research foundation (DFG), the objective of the project was the aero-thermodynamic design of a scramjet propulsion system for future space transportation systems [188]. Together with the aforementioned research projects, it shows the great international effort invested in future reusable space transportation systems and scramjet propulsion as key technology for hypersonic flight.

To reach this objective, the goal of the GRK 1095 was the development of a scramjet demonstrator that fully integrates all required engine components such as inlet, isolator, combustion chamber and nozzle. The strong interactions between all engine elements prevented a separate development of the components. Instead, interdisciplinary collaboration was required to achieve a reliable operation of the engine in supersonic combustion mode. The GRK 1095 provided the framework for this collaboration, which included the University of Stuttgart, the RWTH Aachen, the Technical University München and the German aerospace center (DLR) in Cologne [56].

The scramjet demonstrator is designed for Mach 8 and 32 km altitude. The results of the GRK 1095 should provide the foundation for a possible flight experiment following the parabolic flight trajectory established by the HyShot program. Different scientific areas emerged within this design process. This included aero- and gasdynamics for the inlet and nozzle design, unsteady flow phenomena such as shock boundary-layer interaction as well as aerothermodynamics and combustion science to achieve a stable supersonic combustion. Furthermore, the overall system was investigated.

A key aspect of the GRK 1095 was to develop its own experimental, analytical and numerical methods and tools. This approach allowed to obtain numerical and experimental data sets in such detail as required for the tasks. Another aspect was that the analytical and numerical tools could be validated with reference experiments that were performed within the project. Although obtaining experimental data is challenging for the high temperatures and velocities associated with supersonic combustion, it is a crucial element for CFD validation. The former was a particular objective for this thesis.

1.2 Current State of Research

This overview of the research initiatives provides an impression of the effort associated with the development of such a flight vehicle. Experimental data obtained during testing play an important role in the design and development process. In the following, this role is further addressed together with a brief outline of the established diagnostic techniques, which are commonly used to achieve this task. Their application as found in literature illustrates the motivation and resulting objectives for the present work.

1.2.1 The Need of Experimental Data

The flows relevant to this development and to this thesis are characterized by supersonic speed, high temperatures and on-going chemical reactions. Supersonic combustion experiments are challenging for any measurement technique, as temperature and flow velocity are inherently high. Furthermore, the flow field under study is complex, as effects of chemical reactions, fluid dynamics, heat and mass transfer processes coincide and, more importantly, interact.

Ground tests allow a detailed investigation of engine components under defined conditions. This is particularly useful for isolating a certain aspect and providing a better understanding of the underlying phenomena. Examples may include the design of the intake, the injection scheme and the mixing process in the combustor or the nozzle performance. Although ground facilities are limited in reproducing realistic flight conditions, such tests are vital to verify operation prior to a flight experiment.

In addition, experimental data are important to validate numerical predictions. Complementary CFD simulations become an invaluable tool in the design and optimization process. Especially the development of scramjet engines depends heavily on numerical predictions as so far all experiments – either ground or flight tests – are conducted with small sub-scale demonstrators. CFD has the potential to extrapolate the obtained results to real-size engines. Considering computational time and costs, RANS simulations are the most practical approach for an engineering design tool. These numerical predictions apply mathematical models of the reality to account for turbulence, diffusion, the thermodynamic state, chemical reactions and so on [7]. Therefore, experimental data of test cases conducted for similar flow conditions are required to develop and validate these models.

To accurately predict reactive high-speed flows, the applied models must account for a number of individual aspects, including turbulence, compressible mixing, interaction between turbulence and chemistry and the combustion mechanism itself [58]. The progress in speed and memory of computers allows the development of more realistic physical models, which pushes experimentalists to provide suitable data for validation of these models [55]. Experimental configurations to realize such flow fields often employ axisymmetric coaxial free jets due to the good access and the advantages resulting from its symmetry.

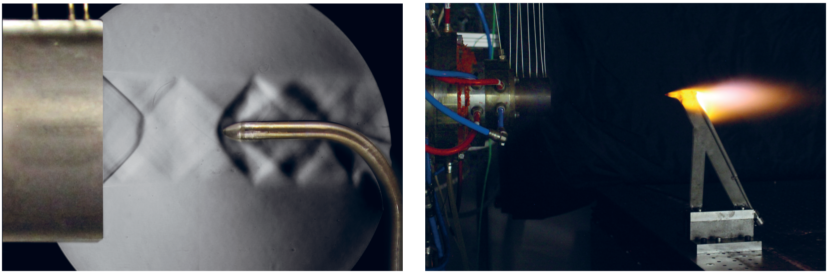

Figure 1.3: Bow shock and its reflections for a Pitot probe in a supersonic jet (left). Flame structures induced by the flow field around the high-temperature probe (right)

Which diagnostic tool is the measurement technique of choice often depends on the application and the flow parameters required for validation.

Schlieren and shadowgraphs, for instance, are useful to visualize the flow structures, but are qualitative in nature. Obtaining quantitative data inside the flow field sufficiently resolved in time and space, however, is a difficult task for such hostile environments. To uniquely specify the flow, information about the velocity field, the thermodynamic properties and the chemical composition is necessary. Usually a combination of techniques is desirable to obtain a complete data set. The following provides an overview of conventional (non-optical) and optical techniques to perform this task. A focus is put on techniques that allow to derive temperature and velocity. As most optical methods show a dependency on the spectral properties of the test gas, their use for concentration measurements is commented if applicable.

1.2.2 Intrusive Diagnostic Techniques

Physical probes are a well-established approach for obtaining quantitative data inside a gas flow [179]. These probes may measure pressure [135], temperature [107] or allow to extract gas samples at a certain position in the flow field that are used to analyze the gas composition [111]. A variety of flow quantities can be derived from such measurements, including static and total pressure, temperature, flow velocity and direction as well as species concentration.

While a valuable and straight-forward diagnostic tool, physical probes interfere with the flow field, which limits their application to high-enthalpy or reacting flows. This results in two major constraints. Firstly, the probe must be able to mechanically withstand the gas temperatures. Secondly and more importantly for the flow investigated in this thesis, the presence of the probe influences the flow field under study. While water-cooling [117] or high-temperature resistant materials [13, 159] can extend the operation limits even to extremely hostile environments, the intrusive nature is inevitable. This is particularly negative for supersonic flows, where generated shock waves substantially alter the flow field, as well as combustion experiments, since chemical reactions are strongly linked to the fluid dynamics. Both effects are illustrated in figure 1.3. Heat transfer into the probe structure and catalytic effects on its surface may further disturb the combustion.

Particle image velocimetry (PIV) is a widely used technique for velocimetry as full systems and post-processing solutions became commercially available over the past decades. Grant [64] provides a comprehensive review of the technique and its evolution. Briefly summarized, a laser sheet illuminates particles seeded into the flow field. The velocity is determined from the displacement of these particles observed in two subsequent images. The flow field is, hence, not directly probed, but determined under the assumption that it coincides with the flow path of the particles, which imposes several requirements on the seeding system and tracer particles used [122]. However, if the assumption is justified, the technique excels, as planar measurements of the velocity field are provided. Recent developments include pressure [180] and temperature measurements [46] for well-conditioned environments.

PIV is predominately used for incompressible flows. For high-speed flows, appropriate particle seeding becomes a difficult task. Main aspects are that particles are not uniformly dispersed and lack behind the flow field [173]. A recent review of physical and technical challenges that emerge from PIV measurements in supersonic flows is given by Scarano [147].

1.2.3 Optical Diagnostic Techniques

Optical diagnostic techniques provide the distinct advantage to investigate a flow phenomenon without disturbing the system. For all optical techniques, the information transfer occurs via the propagation of light. In its most basic form this is achieved by studying the natural light emission of a self-luminous object, e.g. a flame, which was reported as early as 1857 by Swan [169]. This approach is still in practice today and known as chemiluminescence.

In more sophisticated techniques, the medium is exposed to laser light and its response to the applied field is analyzed in order to determine the thermodynamic and fluid dynamic state of the medium. The textbooks of Demtröder [37] and Eckbreth [41] provide a comprehensive description of the fundamentals of laser-based diagnostics and spectroscopy.

In the following, a brief introduction of established techniques is given. The selection is based on the recommendations given by Eckbreth [41] and on the overview of spectroscopic techniques for aerospace flows by Danehy et al. [36] as well as for aerodynamic measurements by McKienzie [120]. Kiefer and Ewart provide an excellent review of their application with respect to species detection [99].

Linear Diagnostic Techniques

For these techniques, a linear approximation of the interaction between the laser light and the medium is possible. This results in a signal intensity that is directly proportional to the power of the input beam. The interactions with the medium include absorption, emission and scattering of the incident light. The following techniques rely on one or a combination of these effects.

Tunable Diode Laser Absorption Spectroscopy (TDLAS) uses the absorption of laser light along its beam path as it passes through the medium under study. The intensity ratio between absorbed and transmitted light is described via the Beer-Lambert law as a function of the spectral properties of laser as well as of the thermodynamic and the fluid dynamic state of the gas. A more detailed description of the absorption process can be found in [2] and [5]. For a narrow-line laser source, the absorption becomes species-specific, as the wavelength of the laser light must access a certain molecular absorption line. This allows simultaneous measurements of species concentration and temperature. Modified setups include velocity and pressure as measurands (e.g. [134]).

Over the last decades, TDLAS advanced to one of the most important types of absorption-based techniques. This is further supported as fiber-optic telecommunication systems made lasers and detectors for the near-infrared spectrum widely available [70]. Combustion diagnostics benefit from this development, as strong absorption lines of reaction products such as carbon oxides [187] and water [115] are present in this wavelength regime.

Two advantages of TDLAS shall be highlighted. Firstly, inexpensive low-power lasers can be used in a straightforward setup consisting essentially of a diode laser and a detector. This results in a robust sensor that can operate in harsh combustion systems including scramjets [115], internal combustion engines [192], gas turbines [112] and industrial coal gasifiers [168]. Secondly, TDLAS excels regarding temporal resolution as rapid tuning diode lasers achieve repetition rates in the kHz [113] and MHz regions [106]. Such effectively continuous measurements are especially important for short-duration experiments in impulse facilities, e.g. shock tubes.

While TDLAS offers an excellent temporal resolution, a major constraint is its lack of spatial resolution. As absorption occurs along the entire optical path of the laser beam, the measurement represents a line-of-sight average. Furthermore, the flow properties are found as function of the shape of spectral features characteristic for the species probed. Accurate measurements require precise knowledge of the response of the absorption spectrum to the thermodynamic and fluid dynamic state of the test gas. Elevated pressures, for instance, may further complicate the post-processing [168], as initially separate features overlap due to pressure broadening of the absorption lines.

Laser-Induced Fluorescence (LIF) is a spectroscopic technique that combines absorption and emission of light. In contrast to the natural emission used for chemiluminescence, the molecules of the investigated test gas are first excited by a strong laser pulse. The return of the excited molecules to a lower electronic state causes a spontaneous photon emission. The intensity of the emitted light correlates to gas properties such as temperature, mole fraction of the excited species, pressure and velocity. Out of these dependencies, the focus is usually on concentration [158] and temperature [44] as measurands. Pressure and velocity measurements are less common, but possible as, for instance, demonstrated by Hiller and Hanson [86]. A review on the application of LIF for combustion gases is provided by Hanson et al.[71].

A key feature of LIF is that planar measurements are possible, since a laser sheet similar to PIV is used for excitation. Furthermore, even minor species concentrations ($<1\%$) can be detected. For qualitative measurements, it provides a simple way to visualize the species distribution in a flow field (e.g. [11, 194]).

Quantitative measurements, however, require an elaborate calibration of the signal intensity to isolate the dependency on the concentration of the excited species, the temperature and the pressure. Furthermore, it is necessary to account for the excitation dynamics and energy transfers between the molecules in the post-processing. Especially collisional quenching affects the signal intensity as it causes a non-radiant return of excited molecules to ground state. Contribution of quenching is often difficult to quantify, which prevents an easy derivation of flow quantities from the signal intensities [132]. The interpretation of the signal intensity might be further complicated if absorption causes the energy of the excitation laser to decrease as the light sheet passes through the flow field. At the same time, re-absorption of the fluorescence signal by the surrounding flow occurs for overlapping emission and absorption spectra. Together with the dependency of intensity on the thermodynamic state of the gas, all these effects must be quantified in the calibration.

Another constraint is that light emission is incoherent in phase and direction. Therefore, only a fraction of it is collected by the detection system. As a consequence, high-power, pulsed lasers are required for sufficient signal intensity. Weak signals may be distorted if the object under study is self-luminous, e.g. flames. In addition, the laser must be tunable to access molecular resonance lines of the species of interest, which is either a substance naturally found in the investigated flow (e.g. hydroxyl radicals) or a molecular seed such as toluene or iridium.

Raman spectroscopy is another incoherent diagnostic technique. In contrast to TDLAS and LIF, it is based on light scattering. Raman scattering is inelastic, as energy is exchanged with the molecules. The direction of energy transfer depends of the relaxation of the excited molecules. Relaxation to a state above the originating state marks a energy transfer towards the molecule (Stokes-Raman scattering), relaxation to a lower state implies an energy transfer to the scattered photon (Anti-Stokes scattering). As a consequence, the frequency of the scattered light is shifted to higher or lower wavelengths. By analyzing the Raman shift, temperature and species concentration are determined [41].

Raman scattering features a relatively easy setup, calibration and signal analysis compared to the non-linear techniques presented in the next section. Furthermore, the technique involves only one excitation beam, so that a single high-power laser is sufficient. This laser source can radiate at a fixed wavelength, as no absorption lines need to be accessed. However, its most important feature in comparison to LIF is that Raman scattering is not sensitive to collisional quenching.

The major disadvantage is the very low signal intensity, which restricts the application to major species. This is as inelastic scattering is an inherently weak form of interaction, but also as the scattering occurs in all directions like for LIF. Hence, good optical access and large collection optics are necessary, while the latter makes the technique sensitive to stray light and natural emission of the subject under study.

Non-Linear Diagnostic Techniques

The aforementioned techniques are categorized as linear optical techniques, as the signal intensities scale with the input intensity. To overcome the discussed constraints, the search for other diagnostic approaches resulted in the development of so-called non-linear techniques, which promise higher signal levels. While a linear treatment is accurate for most optical phenomena, the interaction between the medium and the applied fields for these techniques requires a non-linear description. The contribution of higher-order terms is usually small and thus negligibly, unless, for instance, the applied field intensities of the input beams are high. The observed vis-a-vis development of diagnostic techniques and laser sources is partly due to this need for intense laser light.

The proposed increase in signal intensity is, however, less a consequence of non-linearity, but of the generation of a laser-like signal beam. For LIF and Raman, the light emission occurs incoherently, namely random in phase and direction. For the techniques detailed in the next part, the signal generation results from an interaction of three input beams that forms a fourth beam. This process is known as four-wave mixing. The beating of the three incoming fields promotes the radiation of the fourth beam in phase so that constructive signal growth will occur. As the signal is only generated in the direction of the signal beam, almost all of it can be collected even with limited optical access. At the same time, stray light or flame luminescence is easily separated. It is this coherent nature of the signals that gives the higher signal-to-noise ratios.

Coherent Anti-Stokes Raman Spectroscopy (CARS) was derived from spontaneous Raman scattering to overcome some of its constraints. Due to the requirement of high light intensities, the laser beams are usually focused into a measurement volume. This results in temporally and spatially resolved point measurements. CARS is predominantly used for temperature measurements. For dual-pump setups, major species concentrations are obtained simultaneously, e.g. nitrogen in fuel/air reactions [41]. An overview of CARS in comparison to Raman scattering is given by Lempert and Adamovich [110] for high-enthalpy flows. Roy, Gord, and Patnaik [141] highlight recent advances made in applying CARS to reacting flows.

CARS requires two or even three high-power lasers at different wavelengths, out of which at least one laser source is tunable. Gas properties are found from the shape of spectral features and the intensity of the CARS signals in comparison with a calculated spectrum [130]. Excited-state populations and inter-molecular energy transfer govern the signal analysis for CARS. The measurement, hence, relies on the accuracy of theoretical models fitted to the experimental spectrum and thus on the molecular and linewidth data used for the spectral simulation. Quantum-mechanical treatment makes the calculation of the theoretical spectra complex and time consuming, especially if multiple species are involved [24].

As the post-processing, also the experimental setup of CARS is complex and requires a substantial amount of experience. Furthermore, it consists of very expensive equipment including high-class laser systems, spectrometers and low-noise CDD cameras. It is the combination of expensive equipment as well as complex setup and post-processing that is the major drawback of CARS.

Degenerate Four-Wave Mixing (DFWM) is another example for a four-wave mixing technique. Motivation for the development of DFWM is to combine the advantages of CARS for thermometry with the sensitivity for minor species concentrations found for LIF [17]. For DFWM, all beams that participate in the mixing process have the same frequency. This results in a simpler experimental setup. Furthermore, only one pulsed, possibly tunable laser is required.

While the setup is less complex than CARS, the post-processing is comparable to CARS as molecular dynamics and excited-state populations also govern the theoretical model. Like CARS, DFWM is less sensitive to quenching than LIF [34]. Especially in high pressure environments, however, collisional quenching prevents some energy of the input beams from being coupled into the signal. This energy deficit causes a change of the bulk properties of the medium. This effect leads to a *parasitic* signal superimposed to the DFWM signal [39], but also forms the basis of the diagnostic tool that is subject of this thesis.

1.2.4 Application to Supersonic Flow Research

The application of these diagnostic methods is highlighted in the following. As mentioned before, free jet experiments are good examples for reference experiments in mixing and combustion studies. Early work with respect to supersonic combustion includes the free jets investigated by Cohen and Guile [16] and Evans, Schexnayder Jr, and Beach Jr [45] in 1969 and 1978, respectively. For these experiments, air was heated using pre-combustion and accelerated in a nozzle to supersonic speed. Hydrogen was injected parallelly through a coaxial nozzle resulting in turbulent mixing with the hot air stream and ultimately ignition. Data were obtained by water-cooled pressure and gas sampling probes yielding the total pressure distribution and major species concentrations along axial planes downstream of the nozzle exit. Together with data sets of subsonic flames, these experiments were used for the validation of numerical predictions [45]. Although limitations arise from the use of intrusive diagnostics, it is still valuable as reference case even for recent work, for instance [125] in 2003 – partly due to the lack of alternatives.

Cheng et al. [14] summarized the advances made in the 1980s for sub- and supersonic diffusion flames. It is emphasized that optical techniques are particularly desirable to study such combustion processes, since non-intrusive measurements of temperature and multi-species concentrations are possible with sufficient spatial and temporal resolution. These considerations led to the experiment published 1994 in [15], which became probably the most common test case for supersonic lifted diffusion flames [58, 124, 125]. Combining ultraviolet Raman scattering with predissociative LIF allowed to measure mean values and fluctuations of temperature, major species concentration and OH-radicals simultaneously. Two-dimensional velocity data of the flow field were added later by Dancey [32]. A schematic of the burner is shown in figure 1.4 together with the nominal operation conditions used for the experiment. As for the aforementioned experiments, pre-combustion is used to reach the static temperatures in the air flow required for autoignition.

While multiple parameters are measured, the importance of this experiment is mainly due to the fact that the fluctuations of temperature and species concentrations were obtained simultaneously and together with the mean values. This is vital for the validation of numerical methods as it resolves the turbulence-chemistry interaction. The importance is highlighted by Gerlinger et al. [57] using the example of a probability density function approach to model turbulent reactive flows.

Uncertainties in the experimental boundary conditions arise, however, from the pre-combustion [125]. This so-called vitiated air is contaminated with radicals and reaction products of the combustion process, e.g. water, which are known to influence the ignition delay times of the subsequent combustion experiment significantly [61, 167]. The effect on the Cheng experiment is studied in [58]. Here, the authors prove that these radicals must be considered for an accurate prediction of the ignition point. Another undesirable aspect is that the inner nozzle was not properly centered in the experiment [15]. For a supersonic flow, even a small change in geometry can alter the shock pattern and, hence, influence the temperature field and flame strongly. As a result, a distinct asymmetry in the measurements is found. Therefore, the comparison of numerical predictions and experimental data is difficult.

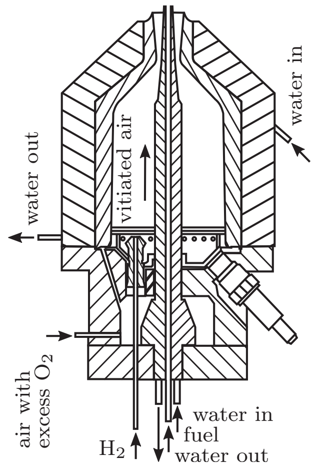

Figure 1.4: Geometry of the burner used in [15]

	vitiated air	H_2
D_{exit}	17.78 mm	2.36 mm
$\dot{m}$	0.0963 kg/s	$3.62 \cdot 10^{-4}$ kg/s
T_{st}	1250 K	545 K
p_{st}	107 kPa	112 kPa
M_{exit}	2	1
v_{exit}	1420 m/s	1780 m/s

Table 1.1: Experimental conditions used by Cheng et al. [15]

Regardless of these drawbacks, the experiment is even in 2009 referred to as the only experiment providing temperature and concentration fluctuations and as one of the most important supersonic combustion test cases for CFD validation [58]. As such, it is in use even for most recent work [119].

A cooperation of the George Washington University and NASA Langley Research Center was initiated to provide an alternative to the Cheng experiment. Their approach also used symmetric coaxial nozzles to obtain high-quality experimental data. The work started with mixing experiments conducted in 1999. Here, the focus was on the mixing of cold air flows with Helium used as surrogate for hydrogen [26]. Measurements obtained from Pitot, total temperature and gas sampling probes were used for the validation of numerical codes developed at the same time [25, 27]. Jet experiments for supersonic combustion were suggested in 2005 within the framework of the Test and Evaluation/Science and Technology program [55]. Furthermore, the program includes the development of the required diagnostic and numerical tools. The validation experiments consist of a laboratory-scale experiment [28] with dimensions similar to the nozzle investigated by Cheng et al. [15] for developing and testing the diagnostic methods. In addition, a large-scale version was built for use at the direct connect supersonic combustion facility [29]. The dimensions of the large-scale experiment are comparable to the mixing nozzle investigated in this thesis. Both combustion experiments use vitiated hot air for the main flow, while hydrogen or ethylene are injected as fuel through the co-flow. A comparison of the nozzles used for the mixing and combustion experiments is given in figure 1.5.

For diagnostics, CARS was seen as the most promising technique. In a first step, a setup originally used for thermometry [68] was extended to a dual-pump configuration for simultaneous concentration measurements [128, 170] in a supersonic combustor. Later, the CARS technique was combined with a interferometric Rayleigh scattering system to include velocity measurements. A first demonstration of the combined techniques for a Hencken flat flame burner was reported in 2006 [8].

Within the progress of the program, preliminary results were presented for the small- [28, 171] and large-scale nozzle [35, 172]. While this includes limited data collected for a reacting flow in the case of the laboratory burner, measurements in the large-scale nozzle were only possible without the co-flow activated. For the large-scale nozzle, challenges arise from the hostile environment, the strong decline of the signal intensity with temperature, the resulting low signal-to-noise ratio and beam steering effects due to the turbulent flow. Practical considerations with respect to its operation also favored the use of the smaller burner.

Further improvements regarding the signal quality of the CARS systems allowed more detailed investigations for laboratory experiments using both nitrogen and hydrogen for the co-flow. The results were published in 2012 including mean values and fluctuations of temperature and species concentration of nitrogen, oxygen and hydrogen along five axial planes [118]. This highlights the importance of the study as the most promising investigation of combustion in high speed flows in addition to the experiment conducted by Cheng et al. [15]. No velocity measurements were conducted, as only the CARS part of the combined setup was used. Furthermore, a drawback of the small-scale nozzle is that the size of the CARS measurement volume is typically 1–2 mm, which is in the order of the nozzle dimensions. Unfortunately, no measurements of the large-scale nozzle with reactive flow are reported so far to the knowledge of the author.

Instead the CARS system was used for investigations in a dual-mode scramjet combustor developed at the University of Virginia [30, 31]. This direct-connect combustor is similar to the combustion chamber investigated within the GRK 1095 and is a good example for application of optical diagnostics for ducted flows. Besides the CARS measurements conducted at this facility, applied techniques include PIV [63], schlieren visualization [103] and TDLAS [154].

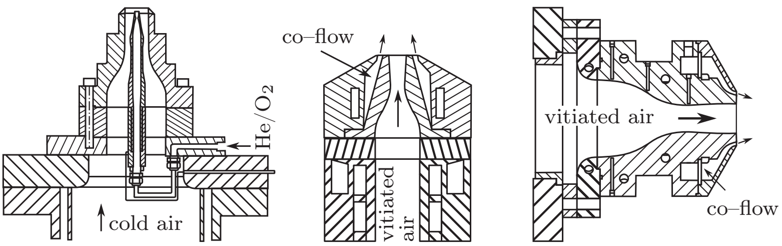

	mixing nozzle	lab-scale burner	large-scale nozzle
D_{center}	10 mm	10 mm	63.5 mm
$D_{co-flow}$	60.47 mm	18 mm	113.9 mm
center flow	95%He/5%O_2	vitiated air	vitiated air
co-flow	air	H_2/ C_2H_4/air	H_2/ C_2H_4/air
$T_{t,center}$	$\approx$ 300 K	$\approx$ 1850 K	$\approx$ 1850 K
$T_{t,coflow}$	$\approx$ 300 K	$\approx$ 300 K	$\approx$ 300 K
$M_{exit,center}$	1.8	0.75/1/1.6/2	1.6
$M_{exit,coflow}$	1.8	$\leq$ 1	$\approx$ 0.07
Reference	[26]	[28, 29]	[29]

Figure 1.5: Nozzle geometries for mixing and combustion jet experiments

Besides the activities in the United States, a number of fundamental investigations were conducted at the combustion test facility at the Institute of Aerospace Thermodynamics (ITLR). This test facility, which is described in more detail in 3.1, has the distinct advantage that the air is heated electrically to prevent contamination with pre-combustion products. An influence of vitiated air on ignition delay times and flame stabilization is hence avoided. Within the framework of the collaborative research center SFB 85 (1972–1985), experimental and numerical investigations of a premixed, shock-ignited hydrogen/air flame were conducted in this facility [96]. Spontaneous Raman scattering was used to measure temperature profiles at different axial positions [95, 97].

This research was continued in the subsequent program SFB 259. Besides mixing and combustion studies for scramjet combustion chambers, the focus was laid on designing an individual supersonic combustion jet experiment for providing fundamental data for CFD validation [183]. Pulsed Raman scattering was used to obtain species concentrations in the flame [98]. For this work, a previous design of the nozzle used in this thesis was investigated. In cooperation with the Institute of Combustion Technology, DLR Stuttgart, the applicability of the CARS technique at the test facility was investigated, where similar challenges as described by Tedder et al. [172] were encountered which resulted in deteriorated signals.

1.3 Motivation and Objectives of this Thesis

The GRK 1095 continues the research on basis of the work conducted in the collaborative research centers. This includes the development of optical diagnostic techniques and the investigation of compressible, turbulent, chemically reacting free jets. This is of special interest as shown in the last section, since reference experiments for high-speed reacting jets are rare [58] in general, but in particular for large-scale nozzles. Due to the challenges encountered with the Raman and CARS systems, LITA was chosen as a diagnostic tool. The reasons for selecting LITA as a promising alternative for supersonic flow research are discussed in more detail in section 4.5 within the context of the signal generation and processing. Preliminary LITA measurements in heated air/air free jets were conducted by Schlamp et al.[152, 153], but were limited to static temperatures below $T_{st} \leq 540\,\mathrm{K}$. However, it motivated to choose LITA as a diagnostic method within the GRK 1095.

The GRK 1095 comprises three subsequent project phases, in which LITA was successively improved. The author's work and the results presented in this thesis are subject to the last phase. In the first generation of the GRK 1095, a pulsed LITA system was set up to conduct time-averaged measurements of the speed of sound. This setup was used for sub- and supersonic air jets as well as mixing jets (air/air, He/air, CO_2/air) with an inlet total temperature up to $T_t \approx 600\,\mathrm{K}$ [139]. In the second phase, LITA was further refined for the use in the test facility. This allowed to increase the inlet total temperature up to $T_t \approx 1300\,\mathrm{K}$ for measurements in a supersonic air/air jet as well as a compressible, chemically reacting H_2/air jet. Furthermore, laminar premixed subsonic flames in a laboratory-scale burner were conducted. In all experiments, time-averaged speed of sound measurements were obtained [77].

Based on the achievements in the previous studies, the motivation and objectives of this thesis include further development and validation of the technique as well as its application for combustion diagnostics and other experimental configurations:

Development: Three objectives are pursued. Firstly, an extension of the setup is intended to include velocity and – together with the speed of sound – Mach number measurements. Secondly, single-shot capability is essential to provide time-resolved data of the flow field in contrast to the time-averaged measurements conducted so far. The last point concerns the everlasting chase for better signal-to-noise ratios. This is particularly important for extending the application of LITA to ducted flows, where the power of the input beams is limited by the windows.

Validation: A quantification of the measurement uncertainty is required under laboratory as well as under test conditions. This includes the verification of the accuracy of velocity and speed of sound measurements by comparison to reference measurements obtained from an additional technique and the investigation of the influence of the harsh conditions at the test facility on the precision of LITA. Furthermore, operational limits for the setup must be addressed by analyzing the dependency of the signal intensity on pressure and temperature.

Application: With these improvements made, the objective is to add velocity information to the free jets investigated previously. This is especially desirable for the chemically reacting jet experiment [183]. Furthermore, time-resolved measurements will include information about the fluctuations of the measured quantities to provide better experimental data for CFD validation [58]. Secondly, the ability to measure within ducted flows unlocks entirely new applications apart from free jets. The scramjet combustor is an example that comes naturally to mind, since it is developed in the same research project. However, other applications apart from supersonic flow research are possible as well.

To achieve these objective, the following steps were conducted, which reflects the structure of this thesis. Firstly, the physical fundamentals and experimental facilities are introduced in chapters 2 and 3, respectively. The LITA technique is described in chapter 4 together with the optical setup developed for this work. Several reference cases were investigated to provide confident knowledge of the performance of the LITA technique for the intended application (chapter 5). The validated setup was then used in three different applications, namely the reacting free jet, the scramjet combustor and shock tube experiments (chapter 6). The thesis concludes with a discussion of the obtained result with respect to the initial objectives (chapter 7).

1.4 Publications

The work conducted for this thesis has partially been published in conference proceedings and journals. This includes the evaluation of the LITA setup for free jets [47, 78] and ducted flows [48, 50] as well as results obtained with additional measurement techniques developed for the application at the test facility [13, 49, 51].

CHAPTER 2

Physical Fundamentals

This chapter provides an overview of the flow phenomena investigated in the present thesis. This includes an introduction to compressible flow in general, supersonic nozzle flows and shock-heated flows.

2.1 Compressible Flow and the Speed of Sound

Fluids in motion play a central role in many technical applications. Fluid dynamics offer a mathematical framework to describe the flow field and to calculate various fluid properties. This typically involves flow velocity, pressure, density and temperature as functions of time and space. Theses equations are derived in a number of textbooks and the reader is referred to literature for a detailed description, e.g. [3, 189].

With respect to the flows investigated in this thesis, the important point to make is that gases at a high flow velocity can experience a significant change in fluid density. Incompressible fluids such as liquids feature a negligible density change due to motion. This assumption is also acceptable for a gas flow, but only at low flow velocities. At higher velocities, the gas density is not an independent parameter, but becomes a function of pressure and temperature, which couples it to the flow velocity.

Referring to a flow velocity as low or high implies a reference. The measure to distinguish between the incompressible and compressible behavior of the gas is given by the speed of sound. The speed of sound refers to the propagation velocity of a small disturbance, i.e. a sound wave, through a medium. The propagation process is associated with a compression and decompression of the medium along the direction of travel. As the amplitude of a sound wave is small, the change in thermodynamic state can be approximated by a reversible and adiabatic process. Together with the conservation of mass and momentum, the general definition is found according to equation 2.1, where s denotes an isentropic process.

$$a^2 = \left(\frac{\partial p}{\partial \rho}\right)_s \tag{2.1}$$

Equation 2.1 allows to derive the speed of sound of any fluid for a given equation of state $p = p(T,\rho)$. In case of an ideal gas, combining the equation of state ($p = \rho R T$) with an isentropic change of state ($p/\rho^\gamma = const.$) results in

$$a = \sqrt{\gamma R T}. \tag{2.2}$$

The speed of sound determines how fast a fluctuation can travel through the medium. Comparing the flow velocity to this propagation velocity allows an objective measure whether compressibility effects must be considered. The corresponding dimensionless quantity is the ratio of flow velocity and speed of sound, i.e. the Mach number.

$$M = \frac{v}{a} = \frac{\text{flow velocity}}{\text{speed of sound}} \tag{2.3}$$

The Mach number is particularly useful to classify the different flow regimes. For $M < 0.2$, the flow is typically considered incompressible as the resulting error is acceptable. At higher Mach numbers, a compressible treatment is compulsory. Furthermore, the Mach number allows to distinguish between subsonic ($M < 1$) and supersonic flow ($M > 1$). The latter implies that the velocity of the information propagation in the fluid is below the flow velocity, thus preventing any fluctuation to travel upstream. This restriction is responsible for flow phenomena characteristic for supersonic flow, which are presented in the next section.

2.2 Nozzle Flow

The transition from sub- to supersonic flow is illustrated using the example of a convergent-divergent nozzle. In addition to the ideal gas behavior, the following assumptions are made: The flow field is assumed to extend only in a single direction (one-dimensional flow), to be constant over time (steady-state flow), to have a negligible viscosity (inviscid flow) or heat exchange with its environment (adiabatic flow). The following set of equations describes the flow properties as function of Mach number and the ratio of specific heat capacities $\gamma = c_p/c_v$ [189].

$$\frac{T_t}{T_{st}} = 1 + \frac{\gamma - 1}{2} M^2 \tag{2.4}$$

$$\frac{p_t}{p_{st}} = \left(1 + \frac{\gamma - 1}{2} M^2\right)^{\frac{\gamma}{\gamma - 1}} \tag{2.5}$$

$$\frac{\rho_t}{\rho_{st}} = \left(1 + \frac{\gamma - 1}{2} M^2\right)^{\frac{1}{\gamma - 1}} \tag{2.6}$$

In equations 2.4-2.6, the indices t and st denote the total and static state, respectively. For the total state, the fluid velocity is zero and all kinetic energy is converted into internal energy as conservation of energy requires. The total state may be seen as the maximum potential, while the static values depend on the portion of energy stored in the motion of the fluid.

These equations allow to describe the flow in a pipe with a varying cross section, i.e. a nozzle, as a function of the Mach number, the total state conditions at inlet and the respective cross section. As transfer of mass or energy is excluded, the conservation of mass requires a constant mass flow for the pipe. Therefore, equation 2.7 must apply for any cross section A:

$$\begin{aligned} \dot{m} &= v \rho A \\ &= \frac{M}{\left(1 + \frac{\gamma - 1}{2} M^2\right)^{\frac{\gamma + 1}{2(\gamma - 1)}}} \sqrt{\frac{\gamma}{R T_t}} p_t A \end{aligned} \tag{2.7}$$

If the flow reaches $M = 1$, the flow is referred to as choked. Parameters at this sonic condition are denoted with an asterisk superscript $()^*$. Then, equation 2.7 reduces to

$$\dot{m} = \left(\frac{2}{\gamma + 1}\right)^{\frac{\gamma + 1}{2(\gamma - 1)}} \sqrt{\frac{\gamma}{R T_t}} p_t A^* \tag{2.8}$$

for $M = 1$ and the critical cross section A^*. The cross section ratio is found by dividing the two equations 2.7 and 2.8 using the fact that the mass flow is constant.

$$\frac{A}{A^*} = \frac{1}{M} \left[\frac{2}{\gamma + 1} \left(1 + \frac{\gamma - 1}{2} M^2\right)\right]^{\frac{\gamma + 1}{2(\gamma - 1)}} \tag{2.9}$$

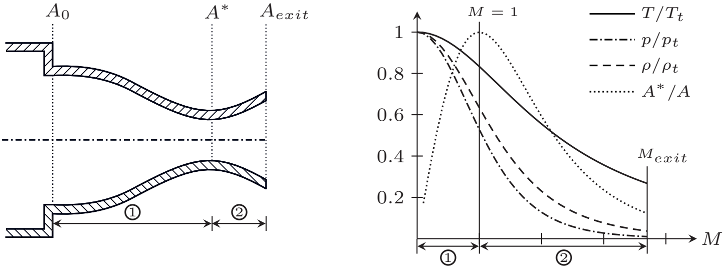

Figure 2.1: Nozzle flow associated with a convergent-divergent nozzle contour

For a given mass flow, this cross section ratio A/A^* is ≥ 1 for $M > 0$. The minimum cross section is found for the sonic condition at $M = 1$ and $A = A^*$. At any other cross section ratio with $A/A^* \neq 1$, both a subsonic ($M < 1$) and supersonic solution ($M > 1$) are found for equation 2.9. This implies that in order to accelerate a flow to supersonic speed the nozzle contour requires a contraction of the cross section down to A^*, which is followed by an expansion towards the nozzle exit. The term convergent-divergent nozzle reflects this relationship. Figure 2.1 shows a schematic of such a nozzle contour together with the evolution of the thermodynamic properties for $\gamma = 1.4$.

In reality, the nozzle is finite in length with a given exit cross section. Therefore, the nozzle flow must accommodate to ambient conditions once it leaves the nozzle as a free jet. The evolution of flow properties along the nozzle as shown in figure 2.1 represents a special case where the static pressure at the nozzle exit matches the ambient pressure. This is not necessarily the case for real applications. Therefore the respective nozzle flow will depend on the nozzle pressure ratio p_∞/p_t for a given fluid and nozzle contour [189].

In the following, the special case of the pressure-matched, axisymmetric, supersonic free jet penetrating into a quiescent environment is considered. The axial development of the jet velocity downstream of the nozzle exit is shown in figure 2.2 together with radial profiles at several axial positions.

First considerations of this kind were published, for instance, by Tollmien [178]. Generally, the three regions are identified as illustrated in figure 2.2. The first region after the nozzle exit is referred to as core region (1). It features a potential core (a) with approximately the same flow properties as at the exit of the nozzle. It is surrounded by a growing shear layer (b), where mixing with the ambient air takes place. This results in an increase of the jet diameter

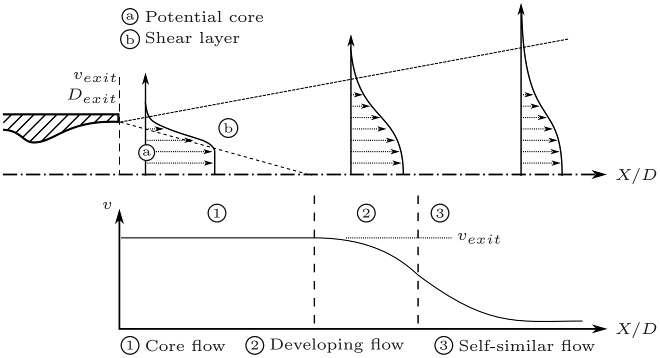

Figure 2.2: Free shear layer evolution for a pressure-matched, supersonic jet penetrating into a quiescent ambient

at a constant opening angle [65]. Further downstream, a transition (2) to a self-similar velocity profile occurs, as the shear layer reaches further towards the jet center line. This leads to a self-similar dispersion (3) of the velocity profile based on the center line velocity and the jet diameter at the respective axial position.

A correlation to estimate the length of the potential core has been published in [126]. Here, the end of the core flow region is defined by the center line velocity falling below 90 % of the exit velocity. The velocity profile at the nozzle exit is assumed to be rectangular, thus neglecting boundary layer effects in the nozzle. For an exit Mach number of $M = 1.5$ provided by the nozzle used in chapter 5, this correlation predicts the existence of a potential core up to $X/D \approx 9$.

These findings only apply to a pressure-matched free jet. If the static pressure at the nozzle exit differs from the ambient conditions, the pressure level adjusts accordingly. For a supersonic exit velocity, this occurs via a shock and expansion system, if the exit pressure is below (overexpanded jet) or above (underexpanded jet) the ambient pressure. Figure 2.3 illustrates the resulting flow pattern for both types.

It should be noted that all considerations so far imply a sufficiently high total pressure at the nozzle inlet to choke the flow and accelerate it to supersonic speed towards the nozzle exit. Starting at the design pressure ratio for a pressure matched jet, the gradual decrease of the inlet total pressure leads first

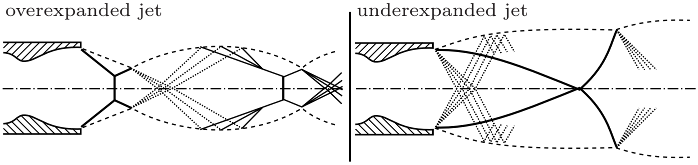

Figure 2.3: Example of the shock (solid lines) and expansion (dotted lines) system associated with an overexpanded and underexpanded free jet

to the aforementioned overexpanded jet and then to a migration of the shock into the nozzle towards the throat. Further reduction results in subsonic flow throughout the entire nozzle.

2.3 Supersonic Flow Phenomena

Shocks and expansions are distinct features of supersonic flow. Shock waves are often observed as oblique shocks when the supersonic flow encounters an object in the flow. An example with respect to scramjet engines is a strut injector to insert fuel directly into the center flow as illustrated in figure 2.4. Unlike in subsonic flow, upstream propagation of information is not possible for supersonic flow. While a subsonic flow would gradually adapt upstream of the object, the adaption takes place directly at the object in supersonic flow via a sudden change in flow properties. This change occurs within a very short distance, typically several times of the mean free path of the molecules. Therefore, shocks can be treated as a discontinuity associated with an increase in entropy.

The change in flow conditions is more severe if the shock angle β is steeper. The extreme case is a normal shock ($\beta = 90^\circ$), which will be addressed together with the description of the shock tube experiment in section 2.4. For an oblique shock as in figure 2.4, the relationship between the free stream Mach number, the deflection angle θ and the shock angle β is given by

$$\tan\theta = 2\cot\beta\left[\frac{M^2\sin^2\beta - 1}{M^2(\gamma + \cos 2\beta) + 2}\right]. \tag{2.10}$$

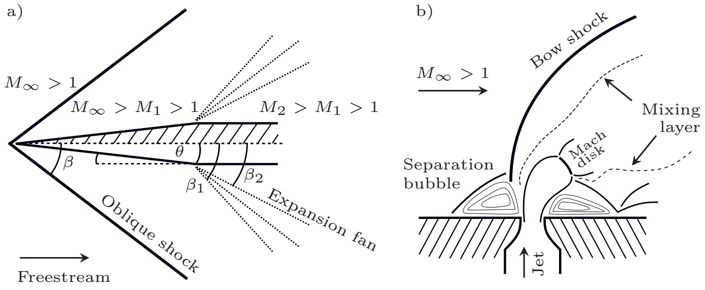

Figure 2.4: Shock and expansion patterns illustrated using the example of a strut (a) and wall injection (b) for a scramjet engine

If the deflection angle is further increased, the oblique shock eventually detaches and takes a curved form, hence referred to as bow shock. Figure 2.4 also illustrates this shock type, but for an alternative injection scheme, namely wall injection. Here, the blocking object is the injection jet, which penetrates into the supersonic cross flow. The jet and the large recirculation zones before and after the injection port cause the shock to detach and form a bow shock in front of the mixing region. This results in large subsonic zones and a fuel insertion only close to the wall, but is significantly simpler to realize than strut injection.

While shocks are associated with a decrease in the flow Mach number and an increase in pressure and temperature, expansion fans act in an opposite way. As the flow passes over the corner at mid-length of the strut in figure 2.4, the surface turns away from the flow, thus acting as a geometrical expansion. This causes the Mach number to increase and, therefore, temperature and pressure to decrease. In contrast to the sudden shock, this acceleration takes place gradually, as the expansion fan consists of an infinite number of discrete Mach waves between the boundary Mach waves at β_1 and β_2. For this reason, expansion fans – as opposed to shock waves – are represented through an isentropic process. The Mach number and the deflection angle are coupled via the Prandtl-Mayer function $\nu(M)$ by

$$\theta = \nu(M_2) - \nu(M_1) \tag{2.11}$$

with

$$\nu(M) = \sqrt{\frac{\gamma+1}{\gamma-1}} \arctan \sqrt{\frac{\gamma-1}{\gamma+1}\,(M^2-1)} - \arctan \sqrt{M^2-1}. \tag{2.12}$$

2.4 Shock-Heated Flows

While shocks are often undesirable in a supersonic flow, they are particularly useful to generate high pressure and temperature environments in a shock tube experiment. These conditions are obtained by deliberately generating a normal shock wave, which rapidly compresses the test gas. Therefore, shock tubes are widely used in a variety of scientific applications, where such environments are required. This includes, for instance, shock induced flows [91], combustion chemistry [69], fluid disintegration studies [4] and re-entry physics [90].

A shock tube is divided into two compartments separated by a thin diaphragm. Filled to different initial pressures, the high-pressure and low-pressure sides of the shock tube are referred to as driver and driven section, respectively. As the diaphragm bursts, the system must quickly accommodate to the experienced pressure gradient. This results in a shock wave traveling into the driven section and a counter-propagating expansion fan. Figure 2.5 illustrates the different states during an experiment in a location-time (x,t) plot. Following the conventional nomenclature, states 4 and 1 correspond to the initial conditions in the driver and driven section. State 2 describes the flow field behind the incident shock wave, where the test gas is not only compressed and heated, but also accelerated towards the shock tube end wall. The shock wave reflects at the end wall of the test section. As the shock front travels back, the test gas is compressed a second time, which results in a quiescent environment, but at high pressure and temperature (state 5). The contact surface represents the gas interface of driver and driven gas if both sections are filled with different gases. The temporal evolution of the gas properties observed at a fixed location, e.g. the measurement position, is shown on the right of figure 2.5.

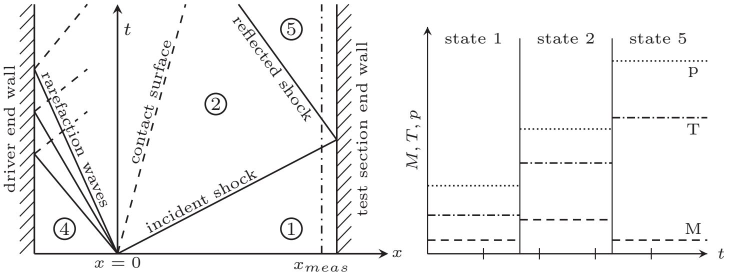

Figure 2.5: Flow conditions in a shock tube experiment

The velocity of the incident shock waves v_s and the speed of sound of the driven gas in state 1 form the shock Mach number $M_s = v_s/a_1$. The shock velocity is governed by the ratio of the initial pressures p_4/p_1 and the thermodynamic properties of the test gases. Assuming a one-dimensional (normal) shock, inviscid flow and ideal gas behavior, the pressure, temperature and Mach number after the incident shock can be calculated as a function of the shock Mach number [129]. In these equations, f denotes the degrees of freedom of the gas molecules. For an ideal gas, f is set to 3 or 5 for a monatomic (e.g. argon) or a diatomic gas (e.g. nitrogen), respectively.

$$\frac{p_2}{p_1} = \frac{(2+f)M_s^2 - 1}{1+f} \tag{2.13}$$

$$\frac{T_2}{T_1} = \frac{(M_s^2 + f)[(2+f)M_s^2 - 1]}{(1+f)^2 M_s^2} \tag{2.14}$$

$$M_2^2 = \frac{M_s^2 + f}{(2+f)M_s^2 - 1} \tag{2.15}$$

As the shock wave reaches the end of the driven section, it reflects off the end wall and travels back. The strength of this reflected shock wave is such that the velocity induced by the incident shock wave is compensated. Due to the boundary condition $v_5 = 0$, the initial shock Mach number also governs the gas properties in state 5. For the pressure and temperature behind the reflected shock, this results in equation 2.16 and 2.17.

$$\frac{p_5}{p_1} = \frac{[(2+f)M_s^2 - 1][(3+f)M_s^2 - 2]}{(1+f)(M_s^2 + f)} \tag{2.16}$$

$$\frac{T_5}{T_1} = \frac{(2M_s^2 + f - 1)[(3+f)M_s^2 - 2]}{(1+f)^2 M_s^2} \tag{2.17}$$

CHAPTER 3

Experimental Setup

This chapter provides an overview of the test facilities that were used for the experiments and their operational range. This includes long-duration as well as impulse facilities. As both types have individual requirements and challenges for applying the LITA technique, these aspects are addressed together with the description of the facility.

3.1 Combustion Test Facility

The combustion test facility at ITLR is a long-duration, direct-connect facility. Figure 3.1 shows an overview of the facility and its components. A screw compressor provides a continuous supply of compressed air. After compression, the air is dried in a dehumidifier and heated in a three staged electric heating system. The heated air is fed to the test section selected for the experiment. In addition, four pressure tanks with a total volume of $8\,\mathrm{m}^3$ store air at a pressure of $10\,\mathrm{MPa}$ as a back-up air supply to allow an emergency shut down of the heating system at all times.

The nominal operation range of the test facility is an air flow with a maximum total temperature of $T_t = 1300\,\mathrm{K}$ and a maximum mass flow of $\dot{m} = 1.45\,\mathrm{kg/s}$ at a maximum total pressure of $p_t = 1\,\mathrm{MPa}$. The key features of this facility are its continuous operation as well as the electric heating system which allows very long test times with clean, hot air. These are desirable for a number of applications such as combustion experiments, cooling studies and validation of new measurement techniques. Especially for combustion experiments, the electric heating system is important as it prevents contamination of the test gas with spurious radicals left from pre-combustion as in the case for vitiated air facilities.

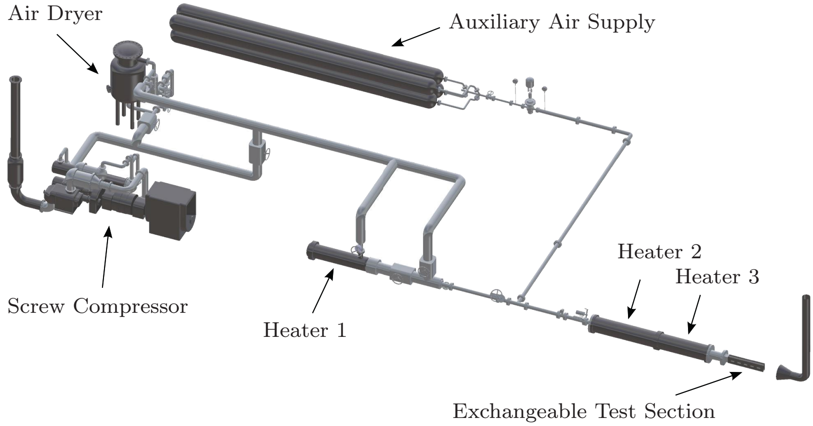

Figure 3.1: Combustion test facility at ITLR

Besides these advantages, several distinct disadvantages of the test facility with respect to the application of optical measurement techniques exist. The test facility is the major source of distortion for the carefully aligned optical system. This is as strong vibrations are induced which cause the mounting elements to loosen. In addition, the acoustic pressure of the gas jet makes protective shielding of the optical setup necessary to prevent a misalignment of the laser beams. This is particularly important for hot gas experiments as the heater requires up to two hours to reach the desired gas temperature. At the same time, the LITA signal intensities are lowest for hot gas experiments. Whether the remaining alignment is still sufficient to take measurements can only be verified after the experimental conditions are reached.

Furthermore, laser and detection equipment are typically designed for use in a laboratory. The environmental conditions differ significantly for the test facility which regularly affects the operation of the equipment. Similar effects are observed due to the electric field caused by the large electrical current going through the heater coils, which tends to interfere with sensitive electronic equipment. With the main flow activated, the entire air in the testing area circulates which causes particles and dust to raise. Once in the air, these particles disturb the laser beams. Secondly, the deposition of dust particles on the surface of optical elements quickly destroys the thin coating, when the particles are hit by the high power laser.

3.2 Free Jet Nozzles

To investigate different types of supersonic free jets, two convergent-divergent nozzles were used. The first nozzle generates a pressure-matched free jet as reference for the validation of the LITA measurements by comparison with conventional intrusive probes. The second nozzle features a primary and secondary flow path, which allows to mix a second test gas into the main flow. This nozzle is used for the combustion experiments.

3.2.1 Supersonic Nozzle

Figure 3.2 shows the supersonic nozzle mounted at the test facility together with a cross-sectional view. This convergent-divergent nozzle has an exit diameter of $D_{exit} = 32.18\,\mathrm{mm}$ and generates a free jet with an exit Mach number of approximately $M = 1.5$ at its design pressure ratio $p_\infty/p_t = 0.2724$. The nozzle is made of stainless steel. Originally only the mounting was water-cooled. As high temperature free jets were intended for the validation process, the cooling system was extended to the entire nozzle to prevent the nozzle contour from deformation due to the thermal loads. The contour design is based on the method of characteristics as introduced by Prandtl and Busemann [3] and corrected by the absolute displacement thickness. Total pressure and total temperature are measured at the nozzle plenum to characterize the inlet conditions.

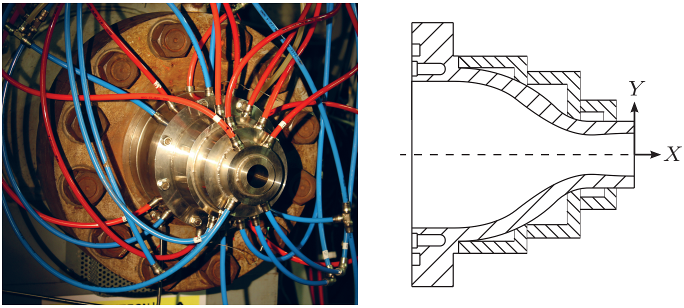

Figure 3.2: Supersonic nozzle: mounted in the test facility (left) and its cross-sectional view (right)

3.2.2 Supersonic Mixing Nozzle

Figure 3.3 illustrates the supersonic mixing nozzle. It represents an improved model of the nozzle design investigated in the SFB 259 [183]. Compared to the nozzle above, it differs in such as it features an outer and inner nozzle of which only the outer nozzle has a convergent-divergent contour. The main flow coming out of the heater system is referred to as co-flow and is accelerated in the outer nozzle. At its design pressure ratio $p_\infty/p_t = 0.1977$, the co-flow reaches approximately $M = 1.45$ at the nozzle exit. The exit diameter is $D_{exit} = 31.4\,\mathrm{mm}$ which makes it comparable in size to the nozzle presented by Cutler et al. [29]. It differs in that the second test gas is supplied through the inner nozzle. The contour of the inner nozzle is convergent, which accelerates the center jet up to $M = 1$. Air or, in case of the combustion experiments, hydrogen can be used as second test gas. All parts of the nozzle are made of stainless steel and water-cooled. The inlet conditions of both nozzles are characterized by total pressure and total temperature measurements in the subsonic parts. At the end of the nozzle, the flame holder confines the flow to the exit diameter of the nozzle. The flame holder supports the mixing of the co-flow and center jet, which stabilizes the flame in the combustion experiments. It contains seven additional pressure taps for static wall pressure measurements.

3.3 Test Channels

In addition to free jets, ducted flows are investigated within this work. This provides the additional obstacle that the optical access is limited to the windows of the test channels. The damage threshold of the windows restrict the maximal admissible power of the laser beams. Several test channels were used to achieve different objectives.

3.3.1 GIP Channel

The Gas Induced Particles (GIP) channel was originally designed to study mixing processes for the production of nano particles [193]. This reference also provides a detailed description of the test channel and its geometry. In brief, the channel consists of a rectangular convergent-divergent nozzle with a throat of 20 mm. The nozzle section is followed by two segments with fixed opening angles of 0.23° and 1.5°, respectively. The width of 40 mm remains

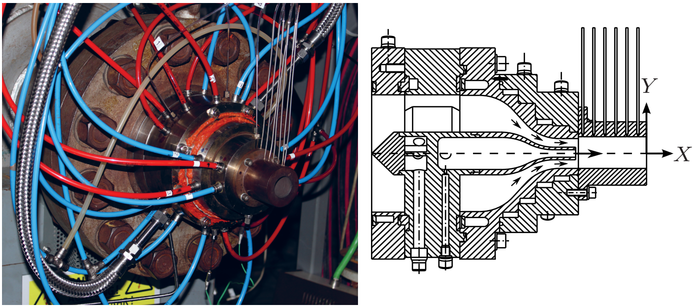

Figure 3.3: Supersonic mixing nozzle: mounted in the test facility (left) and its cross-sectional view (right)

constant for the entire channel. It was selected as simple modifications were sufficient to provide optical access to the sub- and supersonic regions of the nozzle simultaneously. This allows to probe the flow field as it accelerates from low velocity to supersonic speed. Uncooled and made of aluminum, the test channel is restricted to cold flows.

3.3.2 Scramjet Combustion Chamber

Figure 3.4 shows a schematic of the model combustor developed at ITLR. The combustion chamber is divided into four segments. The cross section is constant for the first segment and opens at a fixed angle of 1° in the second segment. Variable opening angles are possible for the two subsequent segments, but both are set to 2° for the present work. The first segment starts with a height of 35.4 mm while the width remains 40 mm for the entire combustor. Exchangeable inserts allow to mount different Laval nozzles which provide flow Mach numbers ranging from 1.7 to 2.5. The channel is manufactured from copper and water-cooled in order to withstand the high flow temperatures. LITA measurements were conducted through quartz windows in the channel side walls (marked gray in figure 3.4).

The chamber features two fuel injection stages to study different injection schemes. The first stage allows to either use a lobed strut injector or wall injection via small holes in the top and bottom wall. In both cases, the injection starts at $x_1 = 513\,\mathrm{mm}$ behind the throat of the nozzle. A more detailed description of the geometry of the strut injector can be found in [51].

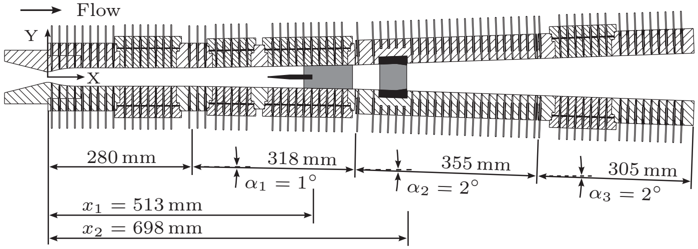

Figure 3.4: Cross-sectional view of the scramjet combustion chamber at ITLR

Both strut and wall injection have been investigated in the present work. The second stage consists of a symmetric wall-bound ramp configuration where fuel is injected at $x_2 = 698\,\text{mm}$.

3.3.3 Modular Supersonic Channel

The modular supersonic channel was built in addition to the scramjet combustion chamber. Its geometry is identical to the combustion chamber except that the channel height remains constant after the nozzle segment. Therefore, the segments can be rearranged or replaced which increases the flexibility of the channel. Even without any form of cooling system, moderately heated flow conditions can be investigated as the channel is made of stainless steel.

This channel was investigated as the experimental data were required for the validation of a numerical solver developed by Dröske [40]. Otherwise, all measurements would have been obtained for the scramjet combustor. As the differences in geometry have little implication on the measurements presented in this study, the channel is only mentioned here for the sake of completeness. All details about its geometry and the developed numerical solver can be found in [40].

3.4 Shock Tube Facility

Figure 3.5 shows the double-diaphragm shock tube at ITLR. The shock tube was designed for fluid disintegration and fuel mixing studies under realistic engine conditions [165]. It features a 3 m long driver section with an internal diameter of 72 mm. The following driven section is 9.4 m long. Before the 1 m long test section, a transition from round to square cross section is made using a skimmer. The edge length of the test section is 50 mm. Besides the improved optical accessibility since flat windows can be used, this allows to dispose part of the incoming boundary layer into the dump tank. Several pressure transducers are mounted along the test section to monitor the transient pressure traces which are used to determine the shock mach number.

The shock tube provides test times of 2–5 ms. After the reflected shock wave, pressures of up to 5 MPa and temperatures of up to 2000 K are reached. A variable-area insert in the driver section compensates for the attenuation of the incident shock wave due to boundary layer effects [166]. This supports a uniform post-shock flow with constant thermodynamic conditions over the entire test time.

Shock tube facilities are desirable for the evaluation of new measurement techniques as they generate reproducible test conditions at high temperatures and pressures. On the other hand, only a single experiment with a short test time is possible before the shock tube needs to be refilled. This implies a precise timing of the measurement and acquisition equipment as the diaphragm bursts and, hence, the incident shock wave is arbitrary in time. Especially for the low repetition rate of the high power lasers used in the LITA setup, this is a difficult task which required a special trigger logic to be developed [50]. Similar to the combustion test facility, vibrations – in this case mainly induced by initial diaphragm burst and the reflection of the shock wave at the end wall of the test section – were a second concern. Their interference was diminished by isolating the optical setup from the shock tube support structure.

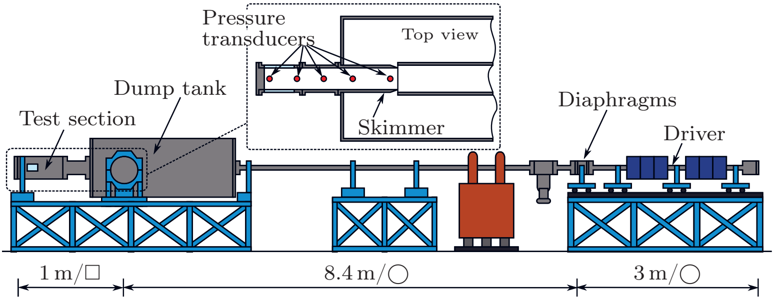

Figure 3.5: Shock tube facility at ITLR (adapted from [165])

CHAPTER 4

Laser-Induced Thermal Acoustics

In order to assess the results presented in this thesis, the development process with respect to LITA is summarized at first. Then, a brief overview of the generation mechanisms for the LITA signals and their dependency on the flow properties is provided. Their implementation in the experiment is discussed, which includes a description of the optical setup and the data processing. The key features of LITA, that led to its selection as the measurement technique of choice for this work, are summarized at the end of this chapter.

4.1 Developments in the LITA technique

Following the rise of laser-based methods in the last decades, LITA emerges from advances made in the development of four-wave mixing techniques. Four-wave mixing refers to a process, in which two crossed beams cause a small perturbation in the refractive index of a test medium. These spatially periodic perturbations scatter light of a third input wave into a fourth signal beam from which the physical properties of the test medium are derived. The dynamics of such laser-induced gratings are the basis of LITA and described in detail in [43].

LITA signals are often observed in DFWM applications, where high molecular collision rates of the test gas cause an undesired distortion of the bulk gas properties and result in a parasitic signal [39, 131]. Significant progress in establishing LITA as an independent measurement techniques was made in the nineties. During this time, several pioneers contributed in deriving analytical expressions to reproduce the time and intensity history of the LITA signals. This includes the research groups around Cummings at Caltech [18, 20], Paul and Williams at Sandia National Labs [131, 191] as well as Stampanoni and co-workers at the Paul-Scherer-Institute [162, 163]. Since then, LITA has been demonstrated to measure speed of sound [18, 20], temperature [73, 79], transport properties [21, 114], species concentration [100, 151], pressure [76, 164] and flow velocity [127, 149].

Examples for a systematic characterization of the technique's performance are measurements in the static gas atmosphere of a test cell [18, 164] or tube furnaces [73, 161]. Velocimetry is demonstrated for small gas jets, for instance in [74, 79, 184]. Several studies investigate the potential of LITA for combustion diagnostics in laboratory burners [12, 72, 81]. Non-reacting fuel mixing is, for instance, studied in [100, 140, 155] for a gaseous propane jet injected into an inert atmosphere. Recent developments in LITA for temperature and concentration measurements as well as other molecular physics applications are outlined in the 2011 review of Kiefer and Ewart [99] together with a comparison to other four-wave mixing techniques.

The research group around Hart and Herring at NASA Langley focuses on aerodynamic applications for LITA, also in comparison to more established techniques like PIV and LDA. This includes the evaluation of the technique for different nozzle flows [85] and the characterization of the velocity field around a high-lift configuration of an airplane wing [93]. Measurements of temperature, Mach number and pressure are realized for an undistorted flow in a supersonic wind tunnel [76, 82]. The same setup is used to observe the step change in flow properties across a one-dimensional oblique shock wave [84] which shows the potential for off-body measurements in supersonic flow research. A similar idea is pursued by Mizukaki et al. [123] who conducted temperature measurements behind small spherical shock waves generated by high-voltage discharge [123]. Sander et al. suggested the use of LITA in shock tube facilities [144] and presented first results for post-reflected shock temperature measurements [145].

In general, LITA excels for measurements under harsh environmental conditions, where signals are deteriorated and low in intensity, as it has a number of desirable features summarized at the end of this chapter. Further examples for such applications are rocket nozzle flows [80], piston engines [190] or turbulent supersonic free jets [47, 78] as investigated at ITLR.

At ITLR, we follow the development process started originally by Cummings [19]. His analytical expression of the LITA signal allows accurate gas-phase measurements of the speed of sound and diffusion properties under consideration of finite-beam size effects resulting from the use of focused laser beams [20]. Schlamp extended this models to include velocimetry and account for beam misalignment [149, 150]. He introduced the LITA technique at ITLR and conducted a first evaluation of the technique for supersonic free jets [152, 153] generated at the institute's test facility. This marked the start for applying LITA in the GRK 1095. For the two previous phases of this research project, the technique was established for turbulent supersonic [139] and chemically reacting free jets [77], which forms the foundation of the present work.

This overview intends to give the reader an idea of the divers applications that emerge with the technique becoming more and more established. Many contributions of these research groups are relevant for the work in this thesis, but have not been addressed in the required detail yet. Instead the approach chosen here is to provide this information together with individual objectives of the results presented in the chapters 5 and 6. This allows for a better discussion of the novel aspects of this work with respect to the published state of art.

4.2 LITA Fundamentals

Being a laser-based optical measurement technique LITA inherently involves the field of physical optics. This includes the description of light as an electromagnetic radiation, the approximation of laser beams as Gaussian beams and other phenomena such as interference and light scattering. A thorough treatment of these optical fundamentals that includes the governing equations is provided for instance in [143] and [1]. However, this is neither mandatory nor expedient to explain the principles of LITA. Especially for the dependency of the LITA signals on the flow properties as addressed in section 4.2.3, a physically intuitive interpretation of the underlying mechanisms is intended instead. Their mathematical implementation required to derive an analytical expression of the LITA signals is addressed in detail by Cummings [19].

Generally, the LITA signal is generated as light interacts with the fluid, and vice versa. This allows to distinguish two phases in the signal generation. Firstly, strong laser pulses are used to generate perturbations of the test medium via opto-acoustic effects. In a second step, the temporal evolution of these perturbations is observed by scattering light off these structures into a signal beam via acousto-optic effects.

4.2.1 Excitation Phase

For the first phase, two so called excitation beams are crossed, which results in an interference pattern due to the superposition of the two waves as illustrated in figure 4.1. Both laser beams feature a Gaussian intensity profile and propagate in the x,$y-$plane with the direction specified through the wave vector $\boldsymbol{k}$. The

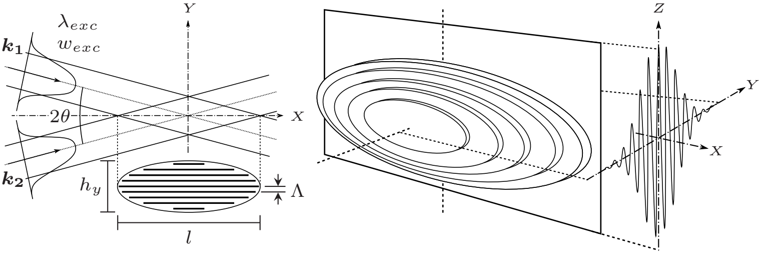

Figure 4.1: Interference pattern due to the crossed excitation beams

wave vectors of the two excitation beams intersect the $x-$axis under the crossing angle θ.

Depending on the beam radius w_{exc}, the dimensions of the intersection region in x-, y- and z-direction are given by

$$l = w_{exc}/\sin\theta, \quad h_y = w_{exc}/\cos\theta, \quad \text{and} \quad h_z = w_{exc}, \tag{4.1}$$

respectively. For small crossing angles, the assumption $h = h_y = h_z$ is justified, which results in an ellipsoidal intersection volume illustrated on the right side of figure 4.1. The distribution of the electric field intensity forms a grating and results from constructive and destructive interference of the two electromagnetic waves. For excitation beams at the wavelength λ_{exc}, the spacing of the fringes in the interference grating is given by

$$\Lambda = \frac{\lambda_{exc}}{2\sin\theta}. \tag{4.2}$$

This spatially periodic distribution of high and low intensity is "written" into the test medium in form of a density grating, which scatters light of a second laser source. As the density grating is congruent with the interference pattern, the dimensions of the intersection region derived above also define the measurement volume of LITA.

The susceptibility of the gas describes the response to the applied field. While various non-linear interactions between a test medium and the radiation of the interference structure are possible, the density grating arises mainly from the opto-acoustic effects electrostriction and thermalization[1]. Electrostriction and

---

[1] Other non-linear interaction such as photophoresis and thermophoresis exist, but are of minor importance.

thermalization are associated with the real and imaginary parts of the complex gas susceptibility.

Electrostriction describes the contraction of a medium due to the polarization of molecules in an applied electrical field [10]. This contraction accelerates the gas molecules towards and away from the regions of high field intensity. As the contraction depends on the applied electric field, it translates into a density grating that represents the fringe spacing of the interference pattern of the electromagnetic waves. Its temporal evolution is interpreted as two acoustic waves packages that propagate perpendicular to the planes of the grating and in opposite directions. The density grating results from a superposition of these two waves and their periodic constructive and destructive interference. Since we are looking at small density fluctuations, they propagate at the local speed of sound and decay at the acoustic damping rate.

Thermalization arises if the wavelength of the excitation beams accesses a molecular resonance line of the test medium. Laser energy is then absorbed by the molecules and converted into thermal energy as the molecules return from excited state to ground state via collisional quenching. This process must be sufficiently fast with respect to the time scales of the LITA signal. If the time required for the thermalization process and the pulse duration of the excitation beams is infinitesimally small, the temperature of the test gas follows directly the intensity distribution of the interference pattern. At this initial state of the grating formation, no bulk displacement of the test gas has occurred yet and, hence, no density grating exists. This response can be interpreted as a thermal grating superimposed to two acoustic wave packages, so that they all cancel each other out initially. As for electrostriction, the temporal evolution of the grating at any later point in time is modulated by the interference of the counter-propagating acoustic wave packets, but superimposed to an additional, stationary thermal grating. In addition to the acoustic waves decaying at the acoustic damping rate, the thermal grating decays by thermal diffusion. In this process, the distortions of the gas due to the density grating are small – typically around 20 µPa [84] and 1 K [149] for the acoustic waves and thermal grating, respectively – which allows to classify LITA as a non-intrusive technique.

This overview of the grating formation already highlights some distinct features of LITA. In contrast to absorption-based techniques, LITA signals can be created even in the absence of a molecular absorption line via electrostriction. Hence, no spectral information of the test gas and no tunable laser source are required to access a particular resonance line. For the same reason, no molecular seed as typically applied for LIF [195] is necessary. Furthermore, LITA excels where increased collisional quenching is present, for instance, in high pressure environments. This enhances the grating formation and, therefore, the signal life time, while the opposite applies to the quantum-mechanical gratings used for DFWM and CARS [89].

4.2.2 Interrogation Phase

In the interrogation phase, the dynamics of the previously induced density grating are observed. It has been said above that the density grating modulates the gas susceptibility, which can be interpreted as a change of the local refraction index according to the structure of the grating. A third input beam referred to as interrogation beam originates from a second laser source. The third beam is partially scattered off these structures and into a fourth beam. The scattering process is only effective for a precise angular orientation of the input waves as shown in figure 4.2. Here, φ represents the intersection angle of the interrogation beam and the x-axis, analogously to the definition of the crossing angle θ. The wave vector $\boldsymbol{k}$ defines the incoming excitation (*exc*) and interrogation (*int*) beams as well as the exiting signal beam (*sig*). In a similar way, the grating is described by the grating vector $\boldsymbol{q}$ which is perpendicular to the fringes of the grating and in direction of the acoustic wave propagation.

The geometry is important, as it ensures that the signal generated at a given fringe is in phase with that of the subsequent fringe. Only then the re-emitted wave field interferes constructively to a strong coherent signal beam that radiates only in one direction specified by $\boldsymbol{k_{sig}}$. The resulting requirement is called phase matching condition and is visualized geometrically in figure 4.2. Mathematically, it is expressed as a combination of the excitation beams as well as the interrogation and signal beams to form the grating vector.

$$\pm\left(\boldsymbol{k}_{exc,1}-\boldsymbol{k}_{exc,2}\right)=\pm\left(\boldsymbol{k}_{int}-\boldsymbol{k}_{sig}\right)=\boldsymbol{q} \qquad \text{with } |\boldsymbol{q}|=2\pi\Lambda^{-1} \qquad (4.3)$$

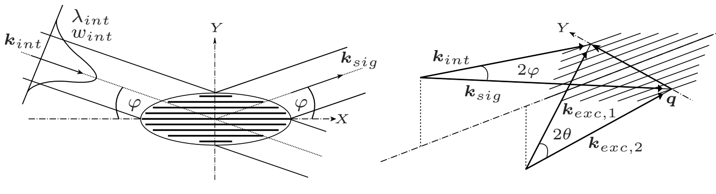

Figure 4.2: Scattering of the signal beam for the phase matching condition

The phase matching condition is equivalent to equation 4.4 which represents the better known Bragg condition. The Bragg law was originally developed to describe the scattering of electromagnetic waves on the atomic lattice of crystalline solids, i.e. another form of grating.

$$\frac{\sin\varphi}{\sin\theta} = \frac{\lambda_{int}}{\lambda_{exc}} \tag{4.4}$$

The phase matching is the only constraint for the wavelength selection of excitation and interrogation beam, as LITA signals can arise from non-resonant excitation via electrostriction. This requirement is actually beneficial, as it facilitates the separation of excitation and signal beams by the use of optical filters. In addition, it ensures much stronger signals than for other optical techniques that also employ linear light scattering, e.g. Raman and Rayleigh scattering. Here, the signal is radiated in all directions rather than in the form of a single strong signal beam with low divergence.

Other techniques like CARS and DFWM also benefit from the coherent nature of their signal beams. However, the signal intensity is still higher for LITA, as signal arises from a grating induced in the bulk properties rather than quantum state distribution of the molecules. De-phasing of the molecular quantum state is orders of magnitudes faster than the decay rates of LITA signals, which are dominated by viscosity and diffusion. Nevertheless, the signal life time of LITA remains in the order of $\mathcal{O}(100\,\mathrm{ns})$ which provides a suitable temporal resolution for most engineering and combustion applications.

4.2.3 Deduction of Flow Properties

As grating formation, evolution and the scattering of light off it have been addressed, the last aspect is to establish the relationship between the LITA signal and the desired flow properties. For the following considerations, it is more practical to express the wavelength of the laser light in terms of the frequency $\nu = c/\lambda$ where c is the speed of light.

Electrostrictive Signals

In a first step, only signals arising purely from electrostriction are considered. As shown above, the grating dynamics are represented by two counter-propagating acoustic wave packages. For a quiescent test medium, the acoustic waves travel at the speed of sound. The signal beam scattered off the wave packages experiences a Doppler shift as it is observed by a stationary photo detector. In its classical limit ($v << c$), the Doppler shift $\Delta\nu$ is given by

$$\Delta\nu(v_\parallel) = 2\nu\frac{v_\parallel}{c} \tag{4.5}$$

where ν is the initial frequency of the light and $v_\parallel$ the velocity component of the moving object in direction of the scattered light. As shown for the phase matching condition above, the angle of the signal beam is equal to the intersection angle φ of the interrogation beam. Therefore, the velocity component of the acoustic wave in direction of the signal beam is $v_\parallel = a\sin\varphi$. Together with equations 4.2 and 4.4, it can be shown that the Doppler shift is equal to the frequency of the acoustic wave $\Delta\nu(a) = \nu_a = a/\Lambda$. The principle is the same as for an acousto-optic modulator, also known as Bragg cell, which is a device to control the intensity and frequency of a laser beam.

As two wave packets with opposite velocity vectors are present, the signal beam consists of light rays shifted up $[\nu]_+$ or down $[\nu]_-$ in frequency depending on the respective wave packets as shown in figure 4.3. The initial laser frequency ν is in the order of $\mathcal{O}$(GHz) and is impossible to resolve with available electronic components. The same applies to the small Doppler shift superimposed to this carrier frequency. A device to isolate the Doppler shift from the initial laser frequency is a non-linear frequency mixer. This is inherently achieved

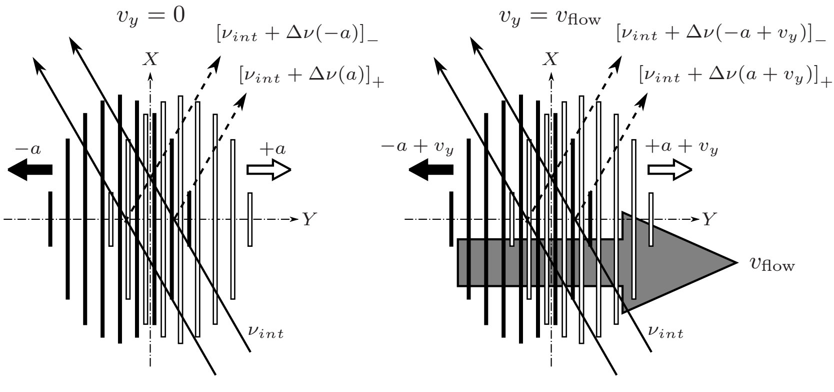

Figure 4.3: Light scattered off the two counter-propagating acoustic wave packets for quiescent (left) and flowing test gas (right)

by detecting the linear superimposed beams with a square-law detector, i.e. a photo diode. The interference of beams on the surface of the detector results in an output voltage modulated at the difference $\nu_+ - \nu_-$ of the frequencies of the incoming light, i.e. at the beat frequency. The beat frequency is now in the order of $\mathcal{O}$(MHz) and, hence, easily detected even with standard electronic circuits. Ω is used to denote the beat frequency and distinguishes it from the laser frequency ν. The resulting beat frequency Ω_{2a} is twice the Doppler shift, as

$$\Omega_{2a} = [\nu_{int} + \Delta\nu(a)]_+ - [\nu_{int} + \Delta\nu(-a)]_- = 2\Delta\nu(a) = \Delta\nu(2a) \tag{4.6}$$

applies. As the Doppler shift is equal to the frequency of the acoustic wave, the speed of sound is derived from the beat frequency via

$$a = \frac{\Omega_{2a}\Lambda}{2} = \Omega_a\Lambda. \tag{4.7}$$

This approach also holds if a test medium is moving at a flow velocity v_y perpendicular to the density grating. Then the wave packets travel at $v_+ = |a + v_y|$ and $v_- = |-a + v_y|$ as illustrated on the right of figure 4.3. However, the beat frequency Ω_{2a} remains unchanged as equation 4.6 yields

$$\Omega_{2a} = \Delta\nu(a + v_y) - \Delta\nu(-a + v_y) = 2\Delta\nu(a). \tag{4.8}$$

This is excepted as the difference in Doppler shift relies on the relative velocity of the wave packets which is still the same. Thus, the present detection scheme – referred to as homodyne detection – is only sensitive to the speed of sound of the test medium and features no dependency on the flow velocity. Instead heterodyne detection is required for LITA velocimetry. Here, an additional reference beam is introduced at the initial frequency ν_{int} of the interrogation

	homodyne		heterodyne	
$v_y = 0$	1: $\nu_{int} + \Delta\nu(a)$	$\Delta_{1,2} = \Delta\nu(2a)$	1: $\nu_{int} + \Delta\nu(a)$	$\Delta_{1,2} = \Delta\nu(2a)$
	2: $\nu_{int} + \Delta\nu(-a)$		2: $\nu_{int} + \Delta\nu(-a)$	$\Delta_{1,3} = \Delta\nu(a)$
			3: $\nu_{ref} = \nu_{int}$	$\Delta_{3,2} = \lvert\Delta_{1,3}\rvert$
$v_y \neq 0$	1: $\nu_{int} + \Delta\nu(a + v_y)$	$\Delta_{1,2} = \Delta\nu(2a)$	1: $\nu_{int} + \Delta\nu(a + v_y)$	$\Delta_{1,2} = \Delta\nu(2a)$
	2: $\nu_{int} + \Delta\nu(-a + v_y)$		2: $\nu_{int} + \Delta\nu(-a + v_y)$	$\Delta_{1,3} = \Delta\nu(a + v_y)$
			3: $\nu_{ref} = \nu_{int}$	$\Delta_{3,2} = \Delta\nu(a - v_y)$

Table 4.1: Summary of the beat frequencies for electrostrictive signals

beam. The reference beam is mixed with the signal beam, either by aligning it colinearly to the signal beam or via a fiber coupler. As now light at three frequencies is present, additional beat frequencies are found as a combination of the incoming waves. The reference beam provides an absolute velocity reference in this process, as its frequency is not changed during the signal generation. While Ω_{2a} of the two light rays of the signal beam is the same as for the homodyne detection, only the mixing with the reference beam causes beat frequencies at $\Omega_1 = \Delta\nu(-a + v_y)$ and $\Omega_2 = \Delta\nu(a + v_y)$ that include a velocity information. They result from the different absolute propagation speed of the wave packages and are used to derive the flow velocity and Mach number. An overview of all beat frequencies for homodyne and heterodyne detection is given in table 4.1. Flow velocity, like the speed of sound, is derived via the fringe spacing Λ, while the quotient of both, i.e. the Mach number, is obtained independently from Λ according to

$$v_y = \frac{\Omega_2 - \Omega_1}{2}\Lambda \tag{4.9}$$

$$M = v_y/a = \frac{\Omega_2 - \Omega_1}{\Omega_2 + \Omega_1}\,. \tag{4.10}$$

Equations 4.9 and 4.10 are derived under the assumption of a subsonic flow velocity. Once the flow Mach number exceeds unity, both acoustic wave packets must travel in the same direction as the fluid. As a consequence, Ω_1 and Ω_2 migrate towards higher frequencies if the flow velocity increases further. The change of direction is reflected by a change of sign, which results in

$$v_y = \frac{\Omega_2 + \Omega_1}{2}\Lambda > a \tag{4.11}$$

$$M = \frac{\Omega_2 + \Omega_1}{\Omega_2 - \Omega_1} > 1 \tag{4.12}$$

for the flow velocity and Mach number. An experimental demonstration of the transition from sub- to supersonic flow is provided with the results in section 5.2.

It should be mentioned that the measurement principle is identical to other Doppler based velocimetry techniques such as, for instance, LDA. The distinct difference, however, is that particle seeding is not required. Instead the particles are replaced by the density grating, but with the advantage that it is induced only at the position of the measurement and only for the time of the measurement. As LITA requires neither molecular nor particle seeding, it can be regarded as a truly seedless technique.

Thermal Signals

If thermalization due to resonant excitation beams is present, the approach remains the same. However, it includes more waves at different frequencies. Starting with a quiescent test medium, the density grating consists of two counter-propagating acoustic waves but with an additional, yet stationary, thermal grating. The signal beam is scattered off each acoustic wave as well as off the thermal grating. While the signal rays associated with the acoustic waves are again Doppler shifted in frequency, the light scattered off the stationary thermal grating remains at its initial frequency ν_{int}. Therefore, even for homodyne detection light at three frequencies $\nu_+ = \nu_{int} + \Delta\nu(a)$, ν_{int} and $\nu_- = \nu_{int} + \Delta\nu(-a)$ is present which results in beat frequencies at $\Omega_a = \Delta\nu(a)$ and $\Omega_{2a} = \Delta\nu(2a)$. The situation does not change if a reference beam at ν_{int} is added for heterodyne detection. Hence, there is no difference between homodyne and heterodyne detection for resonant LITA signals in quiescent test gas as shown in table 4.2.

Velocimetry is, however, still not possible for homodyne detection – even with the additional beam from the thermal grating. As the test medium is in motion, the thermal grating now propagates along with the flow at the velocity v_y. This shifts again all present beams for flow velocity v_y and, as a consequence, the flow velocity based Doppler shifts are canceled in the resulting beat frequencies for homodyne detection (see table 4.2). Instead heterodyne detection is again required to provide an absolute reference ν_{int}. However, the presence of the thermal grating is the reason that a beat at $\Omega_v = \Delta\nu(v_y)$ is found in addition to the other velocity dependent beat frequencies at $\Omega_1 = \Delta\nu(a - v_y)$ and

	homodyne		heterodyne	
$v_y = 0$	1: $\nu_{int} + \Delta\nu(a)$	$\Delta_{1,2} = \Delta\nu(2a)$	1: $\nu_{int} + \Delta\nu(a)$	$\Delta_{1,2} = \Delta\nu(2a)$
	2: $\nu_{int} + \Delta\nu(-a)$	$\Delta_{1,3} = \Delta\nu(a)$	2: $\nu_{int} + \Delta\nu(-a)$	$\Delta_{1,3} = \Delta\nu(a)$
	3: ν_{int}	$\Delta_{3,2} = \lvert\Delta_{1,3}\rvert$	3: ν_{int}	$\Delta_{1,4} = \Delta\nu(a)$
			4: $\nu_{ref} = \nu_{int}$	$\Delta_{3,2} = \lvert\Delta_{1,3}\rvert$
				$\Delta_{3,4} = 0$
$v_y \neq 0$	1: $\nu_{int} + \Delta\nu(a + v_y)$	$\Delta_{1,2} = \Delta\nu(2a)$	1: $\nu_{int} + \Delta\nu(a + v_y)$	$\Delta_{1,2} = \Delta\nu(2a)$
	2: $\nu_{int} + \Delta\nu(-a + v_y)$	$\Delta_{1,3} = \Delta\nu(a)$	2: $\nu_{int} + \Delta\nu(-a + v_y)$	$\Delta_{1,3} = \Delta\nu(a)$
	3: $\nu_{int} + \Delta\nu(v_y)$	$\Delta_{3,2} = \lvert\Delta_{1,3}\rvert$	3: $\nu_{int} + \Delta\nu(v_y)$	$\Delta_{1,4} = \Delta\nu(a + v_y)$
			4: $\nu_{ref} = \nu_{int}$	$\Delta_{3,2} = \Delta\nu(a - v_y)$
				$\Delta_{3,4} = \Delta\nu(v_y)$

Table 4.2: Summary of the beat frequencies for thermal signals

$\Omega_2 = \Delta\nu(a + v_y)$. The last beat frequency is directly related to the net velocity of the flow and results from the propagation of the thermal grating. In total, table 4.2 shows frequency components at Ω_1, Ω_{v_y}, Ω_2, Ω_a and Ω_{2a} which makes it difficult to associate all frequencies found in the spectrum correctly. However, if thermal gratings dominate, only Ω_{v_y} and Ω_a are typically observed. Analogously to electrostriction, the local speed of sound and flow velocity are obtained using the fringe spacing Λ. The ambiguity for sub- and supersonic flow vanishes, as ν_{v_y} gives the flow velocity independently from a.

$$v_y = \Omega_{v_y}\Lambda \tag{4.13}$$

$$a = \Omega_a\Lambda \tag{4.14}$$

$$M = v_y/a = \Omega_{v_y}/\Omega_a \tag{4.15}$$

Thermometry

It is shown that LITA provides measurements of the local speed of sound and of the flow velocity. The ratio of both quantities results in the flow Mach number. The last remaining flow property derived for the results presented in this thesis is the flow temperature. This quantity is not measured directly, but derived from the speed of sound measurement via the equation of state. This implies that the gas composition is known. Therefore, temperature measurements are only presented for experiments conducted in air or in a pure test gas, where this requirement is met.

The conversion is performed either using tabulated values of the equation of state provided by the standard reference database RefProp [109], or via the assumption of ideal gas behavior to justify the use of equation 2.2.

The first approach is used for the pressure cell experiments in section 5.1 and for shock tube experiments in 6.3, as the high pressure environment requires to account for the pressure dependency of the speed of sound in real gases.

An obstacle to the second approach is that – even for an ideal gas – γ is a function of temperature, which is, a priori, unknown. Therefore, an iterative procedure is conducted by estimating an initial γ to calculate a first temperature. This temperature is then used to correct γ before the next iteration. Three iterations are typically sufficient to reach convergence. This approach is used for all experiments with air as test gas that exceed 500 K in total temperature.

4.3 Optical Setup

The optical setup is illustrated in figure 4.4 as it was used for the last experiments. A pulsed Nd:YAG laser serves as source for the excitation beams. The laser is operated at the more powerful first fundamental, which results in an excitation wavelength of $\lambda_{exc} = 1064\,\mathrm{nm}$. A Spectra Physics Quanta Ray Lab-130/10 ($I_{\max} = 450\,\mathrm{mJ}$, $\tau_{\mathrm{pulse}} = 10\,\mathrm{ns}$, 30 GHz linewidth) is used as excitation laser except for the shock tube experiments, where it is replaced by a Continuum Powerlite 8010 ($I_{\max} = 1650\,\mathrm{mJ}$, $\tau_{\mathrm{pulse}} = 7\,\mathrm{ns}$, 30 GHz linewidth) for convenience. The arrangement of optical components allows to split the output beam and to adjust the optical path length of both resulting beams. An efficient grating excitation requires both beams to be equal in intensity and to a difference in the respective beam path lengths smaller than the coherence length of the laser [162]. For the same reason, the output polarization is set perpendicular to the crossing plane [142].

A continuous wave DPSS laser (Coherent Verdi V8, $\lambda_{\mathrm{int}} = 532\,\mathrm{nm}$, 5 MHz linewidth) is used as interrogation laser. All beams are arranged in a forward folded BOXCARS configuration to achieve phase matching as illustrated before in figure 4.2. This allows the use of a single focusing lens to achieve intersection of all beams at the location of the measurement volume. A beam expansion is added to the excitation beam path to adjust its beam diameter with respect to the interrogation beam. This is mandatory for measurements in ducted flows, as it gives the operator control over the region of high laser intensity, which is ideally located at some distance to the windows of the test cell.

In all experiments, the same arrangement of the input beams is used. Instead the crossing angle, and hence the fringe spacing, is varied via the focal length of the used lens, being either 700 mm or 1000 mm. The focal lengths are selected with respect to the bandwidth of the available detectors and maximum speed of sound expected in the experiment. For the 700 mm lens, the corresponding crossing angle and fringe spacing is $\theta = 0.024\,\mathrm{rad}$ and $\lambda = 21\,\mu\mathrm{m}$, respectively. This changes to $\theta = 0.017\,\mathrm{rad}$ and $\lambda = 28.5\,\mu\mathrm{m}$ for the larger focal length. The exact values are derived from a calibration at known conditions prior to the experiment.

Based on the beam waist and crossing angle of the excitation beams, the dimensions of the measurement volume are found according to equation 4.1. This results in an ellipsoidal measurement volume approximately 300 µm in diameter. Due to the difference in crossing angle, its length is either about 8 mm or 12 mm for the 700 mm and 1000 mm lens, respectively. This is a conservative estimation, as only the portion of the grating illuminated by the

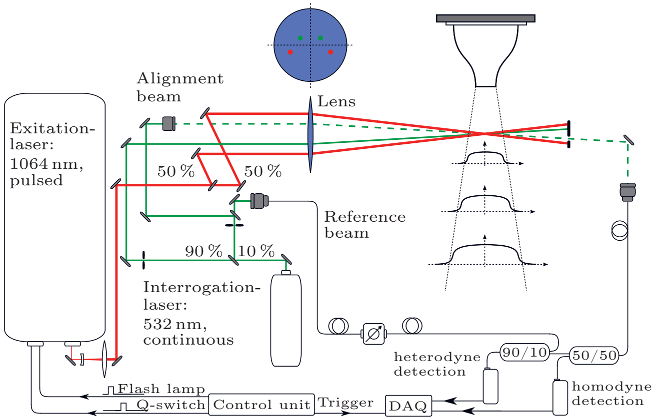

Figure 4.4: Optical setup of the LITA system

interrogation beams would contribute to the signal. Furthermore, excitation and interrogation beams are slightly tilted towards each other, as this supports spatial separation of the weak signal and the strong input beams.

The scattered signal beam is spatially and spectrally filtered and directed to the detector via single-mode fibers and couplers. A DC-coupled receiver with an avalanche photodiode (Thorlabs APD110 [177]) is used in most experiments. In addition, a faster AC-coupled receiver (Thorlabs AP210 [176]) was acquired for situations where the frequency of the LITA exceeds the bandwidth limit of the standard detector. The voltage signal of the detectors is recorded by a 400 MHz bandwidth digital oscilloscope (LeCroy, Waverunner 400Xi).

The reference beam required for heterodyne detection is split off the interrogation beam to minimize phase noise. Its intensity is adjusted to the signal beam intensity via a variable attenuator. Mixing the signal and reference beams is either achieved in a fiber coupler as shown in figure 4.4, or by aligning the reference beam colinearly to the signal beam. In the later configuration, the reference beam is equal to the alignment beam, as it mimics the signal beam path. This is used as alignment aid for the detector-side optics.

The output power of the excitation laser ranges typically from 80 mJ to 120 mJ. For ducted flows, the limit is set by the damage threshold of the windows. However, even for measurements in open flows, a power constraint arises due to ionization of the test fluid. This reaction is accompanied by an intensive light emission, which deteriorates the LITA signal and must therefore not occur during a measurement. For the interrogation beam, the power typically varies from 1 W to 6 W to ensure a signal-to-noise ratio of 10 or better.

4.4 Signal Post-Processing

Generally, two schemes are available to interpret the LITA signals. As shown in section 4.2.3, the flow properties are represented in different frequency components that compose the signal. Therefore, the first approach is to use a frequency analysis to isolate the dominant frequencies in the intensity modulation of the LITA signal. The second approach analyses the signal in the time domain by comparing the recorded signal to a theoretical model derived by Cummings and co-workers [19, 148].

4.4.1 Frequency Analysis

The frequency analysis is performed via a fast Fourier transform algorithm. This is a common approach in engineering, as it allows to effectively compute the power spectrum of a discretized signal. To reduce computational effort, the data is zero-padded in the time domain to obtain a power-of-two number of samples. This also results in a finer grid spacing of the frequency spectrum, which is beneficial for subsequent routines that automatically detect the frequency peaks in the spectrum. The obtained frequencies are then used to derive the flow properties. An example of experimentally obtained LITA signals and computed frequency spectra is included in section 5.2 to illustrate their dependency on the flow velocity.

It should be noted that the fast Fourier transform algorithm assumes the input signal to be periodic over the number of samples. While being periodic in its oscillation, the damped shape of the LITA signal prevents a truly periodic treatment. For aperiodic input data, the discontinuity in the data sequence results in frequency leakage, where the contribution of originally a single frequency component is smeared out over the neighboring grid points. As it is not required to determine the exact contribution of each frequency component, but sufficient to derive the central frequency of it, this effect is not critical. A detailed overview of different frequency analysis algorithms and their influence on processing LITA signals is provided in [6].

4.4.2 Theoretical Signal Fit

For this post processing approach, an analytical expression is used to describe the LITA signal in both intensity and time history. The measurement is made by comparing the theoretical signal to the experimentally recorded signal. Those parameters which yield the best fit of calculated and recorded signals represent the measured flow quantities.

The theoretical model used in this work is derived by Cummings and co-workers. Extensions have been made by Schlamp with respect to LITA velocimetry. For their work, the focus was on the development of LITA as a measurement technique and thus provides a much more elaborate discussion of the governing equations than what is required here. Therefore, only a brief overview is given in the following and the reader is referred to the work published in [19, 20] and [148–150].

As said above, the LITA signal arises from a spatially periodic perturbation in the fluid bulk properties. This justifies the use of the conservation equations of hydrodynamics to describe the evolution of the density grating in time and space. The signal is obtained by linearized light scattering on these structures. The involved equations are far simpler than the quantum-mechanical treatment required to accurately model excited-state populations and inter-molecular energy transfer, which governs the equations of CARS and DFWM signals. Therefore, simple models of electrostriction and thermalization are sufficient to describe the grating formation. Due to the movement of the polarized molecules in the applied electrical field, electrostriction is modeled as a dipole moment that acts as a forcing term in the differential momentum equation. Thermalization results from an energy transfer from the laser light to the flow molecules via absorption and is, hence, treated as a source term in the energy equation.

However, the use of linearized equations of hydrodynamics and light scattering also implies some assumptions that must be respected in the experiment. Hydrodynamics imply a continuous fluid, where the mean free path of the molecules is orders of magnitudes larger than the fringe spacing of the induced grating. This limits the application with respect to measurements at very low densities, for instance in near vacuum applications. Electrostriction and thermalization are assumed to be the only grating formation mechanisms. The time required to establish the grating initially must be negligible with respect to the oscillation period and life time of the signal. This implies the use of a short-pulse excitation laser. Furthermore, all laser beams are assumed as Gaussian beams with plane wave fronts that coincide at the point of intersection.

As a consequence, good beam profiles and alignment must be realized in the optical setup.

Under these assumptions, the resulting analytical expression has been shown to accurately predict experimental signals, including finite beam effects that result from the use of focused excitation beams [20]. The theoretical signal is defined by eighteen parameters as listed in table 4.3. The first set of parameters is associated with the geometry of the optical setup. This includes the wavelength and beam diameters of both the excitation and interrogation beams as well as their crossing angle. Furthermore, it is possible to account for misalignment of the grating and the interrogation beam in direction of the grating vector. These parameters are constant for a given setup and are obtained in the calibration for which all thermodynamic parameters are known.

Heterodyne detection requires the specification of the reference beam. Three parameters describe the reference beam in intensity, wavelength and phase. The last two parameters are in relation to the interrogation beam. These parameters are also fixed for a given setup.

In contrast, the signal intensity changes from shot to shot, for instance due to variation in the laser output power and other non-idealities. As a consequence, the grating strength, and thus the signal intensities, vary as well. For this reason, the magnitude of thermal and electrostrictive gratings are treated as floats to scale the intensity of the theoretical signal to the required level. In a similar way, a trigger delay is introduced to match the time vector of the LITA signal to the time base setting of the data acquisition unit.

The last six parameters describe the thermodynamic properties of the test fluid. This includes the speed of sound, the flow velocity, the transport properties – acoustic damping rate and thermal diffusivity – as well as the thermalization rate and the ratio of specific heats. Provided that all aforementioned parameters are known for a given optical setup, the fitting of the thermodynamic parameters represents the flow properties of interest in an experiment. In a similar way, signals recorded for known thermodynamic conditions allow to characterize the setup specific parameters.

A least squares analysis is used to obtain the best fit of the analytical model to the experimentally recorded signal. The free parameters are varied to minimize the square sum of the difference between the model and the measurement for each data point. The Levenberg-Marquardt algorithm as described in detail in [175] and elsewhere is chosen to perform this optimization. Initial guesses for the parameters as well as upper and lower boundaries, in which it is physically sound to vary the fitting parameters, are provided as input for the fitting

geometric parameters	λ_{exc}	wavelength of excitation beam
	w_{exc}	beam waist of excitation beam
	λ_{int}	wavelength of interrogation beam
	w_{int}	beam waist of interrogation beam
	θ	crossing angle
	η	beam misalignment
reference beam	I_{ref}	intensity
	$\Delta\nu_{ref}$	frequency shift
	$\Delta\phi_{ref}$	phase shift
floats	$\mathcal{U}_E$	electrostrictive grating amplitude
	$\mathcal{U}_T$	thermal grating amplitude
	τ	trigger delay time
thermodynamic parameters	a	speed of sound
	v	flow velocity
	Γ	acoustic damping rate
	D_T	thermal diffusivity
	γ_T	thermalization rate
	γ	ratio of specific heats

Table 4.3: Summary of theoretical signal parameters following the notation of Cummings [19]

routine. This is required as the parameters found by the algorithm feature a minimal residuum, which is not necessarily the global minimum of the target function. Out of the implemented thermodynamic parameters, only the flow velocity and the speed of sound are obtained in the experiments presented in this work. However, the model is successfully used for all validation cases in chapter 5 and shown to provide accurate measurements for a wide range of flow conditions. Examples of fitted and recorded signals are presented as part of the validation cases. The remaining parameters, in particular acoustic damping rate and the thermal diffusivity, represent the potential of the technique for more universal measurements, but were not the focus of the current work.

4.5 Selection Criteria for LITA

LITA is a non-intrusive and seedless technique. In the configuration used for this thesis, it allows a temporally and spatially resolved measurement of the local flow velocity, speed of sound, Mach number and – for known gas composition – temperature. All quantities are obtained simultaneously. Hence, it is possible to derive mean and fluctuation parts of the flow properties at discrete points in the unsteady flow field.

These features are desirable in general, but have particular implications for the present application. Benefits resulting from non-intrusive and seedless techniques for supersonic, high enthalpy flows are addressed by highlighting the restrictions of intrusive techniques in section 1.2.2. Obtaining multiple flow properties simultaneously and time resolved provides comprehensive experimental data sets of the flow field.

With respect to other laser-based techniques, LITA benefits from relatively strong signals. Furthermore, it excels in strong quenching environments that are present in this work for the combustion experiments and the shock-heated flows. Furthermore, there are no constraints for a given setup with respect to the spectroscopic properties of the test gas. No extensive spectral information of the test gas is, hence, required as non-resonant signals can be generated via electrostriction. On the other hand, an extension to multiplex LITA is easily possible to include spectroscopic aspects in the measurements. For such configurations, the high signal intensity allows the application even for tracer species.

LITA is a robust optical technique for measurements under harsh environmental conditions, which most certainly applies to the situation at the ITLR combustion test facility. This is due to the flow quantities being represented in the signal frequency which is less affected by stray light and other distortions than intensity based measurements. Frequency analysis is a common tool in engineering, so that efficient solvers are readily available. In addition, a more sophisticated post processing might be chosen if signals with sufficient quality are obtained for the desired application. Although not pursued in this work, the theoretical model fit also allows to include additional measurement quantities.

CHAPTER 5

Validation

Confident knowledge of its performance is the first step in applying a new measurement technique. For this purpose, a set of reference cases is investigated to establish the accuracy and precision of the setup. The reference cases are selected as follows:

I. Measurements at well-defined thermodynamic conditions to establish the performance of the technique and the setup used

II. Investigation of an accelerating flow to demonstrate simultaneous velocity and temperature measurements with LITA

III. Investigation of a representative test case to compare LITA to a more established measurement technique

These reference cases are chosen to allow for a thorough validation with respect to flow conditions comparable to the intended application. A focus is set on the determination of flow velocity and temperature as measurands as well as on the investigation of ducted and free jet flows at all relevant temperature levels. For each reference case, a review of the contributions of other researchers is presented as far as the experiments are comparable. This represents the state of the art found in literature to the best of the author's knowledge and sets the standard to which the results obtained in this work are discussed.

5.1 High-Accuracy LITA Measurements in a Controlled Thermodynamic System

The objective of the first validation case is to isolate the contribution of the setup and the applied post-processing to the overall uncertainty of the technique. For this purpose, measurements in a laboratory environment are conducted, where external sources of uncertainty, e.g. distortions due to vibrations or other negative influences from the test facility, are minimized as far as possible. Furthermore, the measurements are obtained for a well-defined and accurately controlled thermodynamic system to provide a well-known reference for comparison and evaluation. A variation of the measured quantity is desirable to demonstrate consistency of the obtained accuracy and precision.

Besides establishing the performance of the LITA technique, the absence of external distortions is required for a meaningful comparison between the setup used here and by other researchers. This is important for complying with the benchmark set in literature. Here, Cummings provided the most extensive evaluation of LITA for the determination of gas properties. In his contributions, he stated an accuracy of 0.1–0.5 % for the speed of sound [18–20]. More recently, Stevens and Ewart [164] report high-quality temperature and pressure measurements derived from laser-induced gratings. Based on the values stated for the temperature measurement, an accuracy for the speed of sound of 0.21 % is calculated together with a single-shot precision of 0.08 %. Other examples reporting a comparable performance are references [73] and [76] which shows that the given range is still state of the art. As will be shown below, the LITA setup developed in this work is competitive to these results with an overall accuracy of less than 0.05 % and one standard deviation (precision) for single shots below 0.1 %.

Experimental Setup

A crucial task is to establish a known reference system with an uncertainty well below the uncertainty pursued for the measurement device. For the uncertainty range stated above, this requires a test cell in which the speed of sound is known to within 0.1 m/s at least. This is a difficult task as a first estimation shows. Assuming ideal gas behavior for the test gas, the speed of sound is only a function of temperature. Hence, the required accuracy in speed of sound implies that the temperature in the test cell is constant within 0.2 K for air. This uncertainty margin can be reached, although it would require a very accurate temperature control. However, it remains difficult to ensure a homogenous temperature field throughout the entire test cell. For these reasons, a different approach is chosen in this work, which exploits the fact that the speed of sound of a real gas exhibits also a weak dependency on pressure. Unlike temperature, the pressure distribution of the static gas atmosphere inside the test cell is always homogeneous. For the experiments, the speed of sound is varied by stepwise increasing the pressure in the test cell. The test gas is supplied from a gas bottle stored at the laboratory at ambient temperature. This gives a reproducible thermal boundary condition, provided that enough time is allowed for the gas to reach thermal equilibrium and return to ambient temperature again before the respective measurement is taken. Another advantage of this approach is that the speed of sound can be varied in small increments due to its weak pressure dependence, which will reveal the high sensitivity of the LITA technique.

Argon is used as a test gas, as it has several desirable properties. Firstly, argon is monoatomic, non-polar, and its atoms have spherical shape. This provides a certain molecular simplicity, which is of great importance in the prediction of thermodynamic properties. Considered as a reference fluid with well-known properties, argon is a common choice to calibrate new apparatuses for thermodynamic measurements. For the present application, the advantage of argon compared to other technical gases, such as nitrogen, lies in its low heat capacity, which reduces the time to reach thermodynamic equilibrium.

The speed of sound in argon at the respective pressure is obtained from the thermodynamic standard reference database NIST RefProp [109]. In the case of argon, RefProp uses the equation of state of Tegeler et al. [174] to predict the thermodynamic properties. For the speed of sound at the temperature and pressure range investigated here, the authors state an overall uncertainty of ±0.02 % for their equation of state, which is within the required range.

Measurements were obtained for a pressure range of 0.6 to 3.4 MPa. For the LITA setup, a 700 mm focusing lens was employed, resulting in a fringe spacing of ≈21 µm. Careful alignment of all beams with respect to the windows of the test cell ensured that stray light and reflections were minimized. This allowed to record purely homodyne LITA signals, to which the theoretical signal could be fitted using the least-squares optimization routine.

Results

To give an impression of the degree of agreement between recorded and theoretical signals, typical signal traces are shown in figure 5.1 for a single shot measurement in argon at 1.8 MPa. Due to the high pressure and, hence, density of the gas, the interference grating induces a strong density perturbation resulting in a strong grating with a high reflectivity. As a consequence, the recorded signal features a long life time and high peak intensity, orders of magnitude stronger than the noise level of the detector. The theoretical signal is based on the analytical expression introduced in section 4.4.2. Both signals feature an excellent agreement with deviations less than 15 %. The model accurately reproduces the oscillation and the decay rate of the recorded signal. The speed of sound used to calculate the theoretical signal with the best fit gives the speed of sound measured in the experiment.

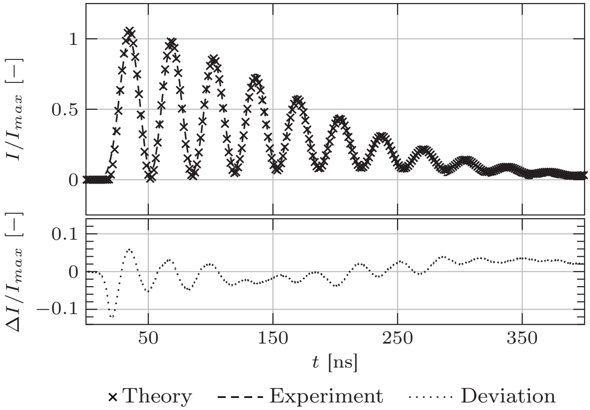

Figure 5.1: Comparison of recorded and theoretical signals for argon at 1.8 MPa

Figure 5.2 summarizes the speed of sound measured at different pressure levels in comparison to the prediction of the standard reference database. The LITA setup was calibrated for the 0.6 MPa measurement. Five additional measurements at higher pressure levels were conducted to investigate the performance of the technique. Calibrating for the 0.6 MPa case reduced the uncertainty due to the ambient temperature measurement. All subsequent LITA measurements were conducted once the gas temperature in the test cell returned to the same value that was defined as ambient temperature for the calibration measurement. At each pressure level, 20 single shot measurements were recorded and averaged for figure 5.2. In addition, the deviation (absolute mean error) between the LITA measurement and the database is shown together with the uncertainty (margin of error) associated with the measurement. The margin of error represents the radius of the confidence interval calculated for the corrected sample standard deviation of the single shot measurements and Student's t-distribution for $n-1 = 19$ degrees of freedom and a 95 % confidence level.

The deviations stay within the uncertainty of measurement for all investigated cases. In summary, the LITA setup features an overall accuracy of less than 0.05 % with a standard deviation (precision) for single shots below 0.1 %. The deviations found are in the same order as the uncertainty in the equation of state used as reference. Hence, the uncertainty in the reference may contribute substantially to the overall deviation. This shows that the limit of what is feasible with this approach is reached and further evaluation would require an even more accurate reference system.

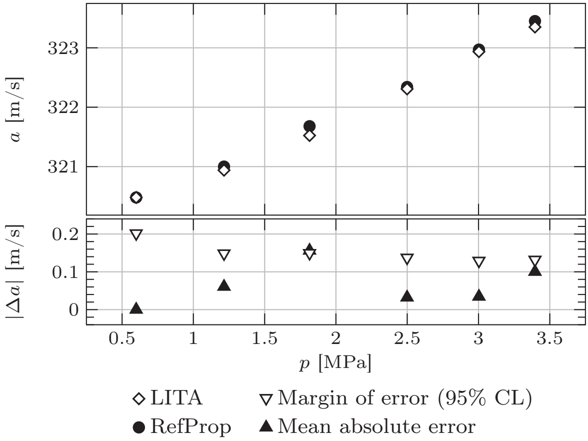

Figure 5.2: Speed of sound in argon at elevated pressures: LITA measurements in comparison to the NIST standard reference database

5.2 Sub- to Supersonic Ducted Flow

The next step is to extend the LITA setup for the velocity measurements. First measurements using the theoretical model of Cummings were presented by Schlamp. With this approach, an uncertainty of less than 0.5 % is reported for low subsonic speeds ($M \leq 0.1$)[150]. More common, however, is to use the frequency analysis for post-processing. Here, the state of the art is considered to be the contributions of Hart et al. For subsonic flow ($M \leq 0.5$), they reported a maximum deviation in Mach number of 0.2–2 % [74, 75]. In a more recent publication, the same authors report an improved value of 0.2 % for supersonic flow with Mach numbers ranging from 1.4 to 2.2 [76]. It should be noted that these results were obtained for a large-scale wind tunnel with a 1.3 m x 1.3 m test section rather than a small, confined test channel as used here.

To allow for a thorough validation at low and high flow velocities, the flow was probed as it accelerates through a convergent-divergent nozzle. This test case demonstrates the capability of LITA to obtain velocity and temperature simultaneously during the transition from sub- to supersonic speed. The reference for comparison with the measurements was provided by a numerical simulation of the channel flow. Again, the LITA setup used here is competitive to the benchmark found in literature. Using a frequency analysis, the velocity measurements and computations agree within 3 % for subsonic flow and within 0.25 % once the Mach number exceeds unity. Larger deviations for the subsonic flow are attributed to the strong acceleration in the convergent part of the nozzle and the resulting uncertainty in the respective reference. In addition, it is shown that similar results can be achieved fitting the theoretical model to the recorded signals.

Experimental Setup

The GIP channel was selected for the first ducted flow experiments. As detailed in section 3.3.1, this test channel features a similar rectangular geometery as the combustion chamber, but instead allows optical access to the sub- and supersonic regions of the rectangular nozzle. Measurements are obtained in the symmetry plane along the center line of the channel. The measurement position is shifted in direction of the main flow throughout the entire nozzle to observe the flow accelerating from low subsonic to supersonic speed with the transition occurring in the throat of the nozzle. The measurements were conducted for the nominal inlet conditions specified by a total temperature of 380 K and a total pressure of 200 kPa.

The reference is provided by a 2D numerical simulation of the flow field. The Reynolds-averaged Navier-Stokes equations are solved on a structured grid using the k-Ω turbulence model. The simulation was conducted by Wohler [193]. This reference also provides a more detailed description of the numerical setup.

Measurements were obtained for a Mach number range of 0.25 to 1.2. To include velocity measurements, a LITA setup was changed to heterodyne detection via a reference beam. All beams were focused using the 700 mm lens. To isolate the dominant frequencies, the LITA signals were transferred to frequency domain using an FFT. As detailed in section 4.2.3, this allows to derive the flow velocity as well as the local speed of sound and, hence, the Mach number. Assuming air as an ideal gas, the temperature can be calculated from the speed of sound. All parameters are derived for the same moment in time from a single measurement.

Results

Figure 5.3 shows the measured Mach number and static temperature in comparison to the numerical prediction. For each axial position, 100 single shot measurements were obtained. As in section 5.1, the average of measurements and the numerical prediction are shown together with absolute deviation and the radius of the 95 % interval. The dashed line illustrates the nozzle throat.

The comparison shows good agreement between experiment and simulation. Deviations exceeding the uncertainty of the measurements are only found for the velocity measurements at subsonic speed. This is probably due to the steep velocity gradient in that section, which makes the measurement more prone to small errors in the alignment of the measurement volume with the center line of the channel. This is further supported by the fact that this is not observed for the smaller velocity gradient towards the end of the test section. At the same time, the observed deviations are a factor of two smaller in this region.

An interesting point regarding the temperature measurements is that at first higher temperatures with respect to the predicted values are measured. This difference gradually decreases as measurements are taken further downstream, where eventually temperatures lower than predicted are found. Since this effect is reproducible, a mere measurement uncertainty is not very likely. It might represent the heat loss into the environment, which is not taken into account by the simulation as adiabatic walls are assumed.

Figure 5.4 illustrates the effect of an increasing flow velocity on heterodyne LITA signals. The signals were recorded at different axial positions and are shown in the time and frequency domains. The frequency spectrum features several dominant frequencies. These beat frequencies result from the interference of the light scattered off the two counter-propagating wave packets and the reference beam. Ω_1 is associated with the wave packet that travels in opposite direction to the flow field and, hence, propagates at lower speed. On the other hand, Ω_2 is linked to the second wave packet propagating with the flow field. The difference of both frequencies is caused by the Doppler shift and is, therefore, a function of the flow velocity. Ω_{2a} remains only a function of speed of sound

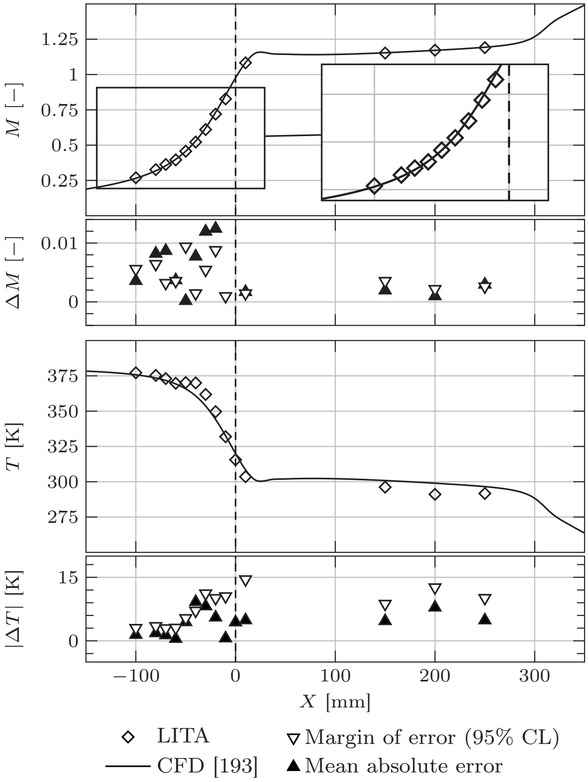

Figure 5.3: Mach number and temperature evolution in a convergent–divergent nozzle flow: LITA measurements in comparison to numerical predictions

as it represents the (unaffected) propagation speed of the two wave packets relative to each other.

With the flow exceeding Mach 1, both wave packets travel in the same direction. As a consequence, Ω_1 as well as Ω_2 increase for higher flow velocities. Figure 5.4 also shows an effect of the flow Mach number reaching unity. Here, it is not possible to separate Ω_2 and Ω_{2a}. Even for $M \approx 1.2$ in figure 5.4 h), it is not possible to identify two peaks, although a starting separation is visible. For the present measurements, the knowledge of the velocity increase along with

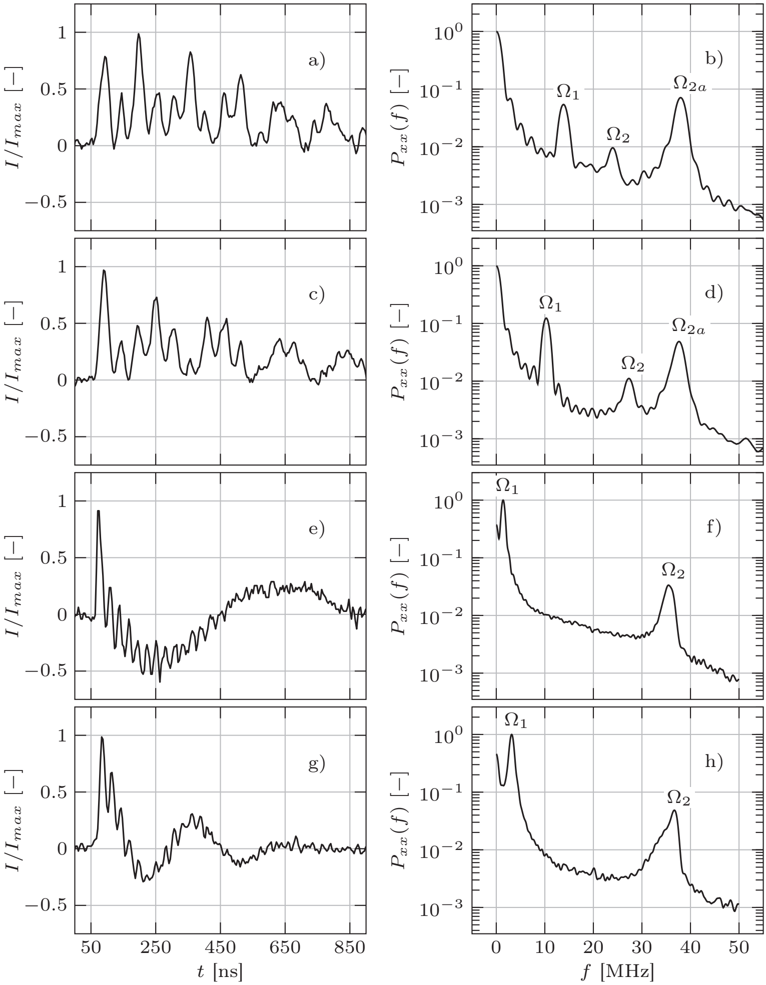

X	−100	−50	+10	+250
M	0.27	0.46	1.08	1.19
Signal	a)	c)	e)	g)
FFT	b)	d)	f)	h)

Figure 5.4: LITA signals in the time and frequency domain at different axial positions and flow Mach numbers

the axial position is used to solve this ambiguity. Although it is not used in these experiments, a fixed frequency shift between interrogation and reference beam (e.g. via a Bragg cell) eliminates this constraint. This is important in situations where no general knowledge about the flow field is available.

An alternative post-processing approach is to fit the theoretical model to the recorded signal as seen in the last section. However, several parameters have to be added to the fitting procedure to reproduce heterodyne signals. This significantly increases the computational effort and time. For this reason, this approach was only applied for the last axial position. Furthermore, it is only intended to demonstrate that the theoretical model can also be used for supersonic flows in addition to the work of Schlamp et al. [150] for low speed flows.

The comparison between experimental and theoretical signal is shown in figure 5.5. Larger deviations are found here than for measurements in quiescent gas. In contrast to the signal intensity, the signal oscillations are still reproduced well, which is the major factor for an accurate velocity measurement. Table 5.1 lists the flow quantities measured using the frequency analysis and the theoretical model fit in comparison with the numerical prediction. It shows that similar results can be obtained with both approaches. Furthermore, it demonstrates that the theoretical model allows an analytical description of the recorded LITA signals for a wide range of flow conditions.

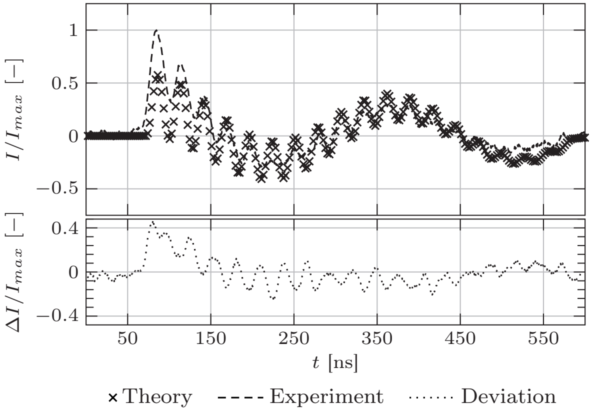

Figure 5.5: Comparison of recorded and theoretical signals for heterodyne detection at $X = +250\,\mathrm{mm}$

	a [m/s]	T [K]	v_x [m/s]	M [-]
CFD	345.19	296.55	411.87	1.193
FFT	342.30	291.69	407.42	1.190
Fit	341.78	290.73	411.53	1.204
$\lvert\delta_{\text{FFT}}\rvert$	0.84 %	1.67 %	1.09 %	0.25 %
$\lvert\delta_{\text{Fit}}\rvert$	1.00 %	2.00 %	0.09 %	0.90 %

Table 5.1: Post-processing based on frequency analysis (FFT) and theoretical model fit (Fit) compared for heterodyne detection at $X = +250$: Deviations are given with respect to the numerical predictions

5.3 Supersonic Free Jets

The last test case is the validation of LITA for the investigation of turbulent free jets. Especially at high temperatures, this imposes high requirements on the LITA setup as, firstly, the highest level of external distortions is present in this case and, secondly, the achievable signal intensity decreases significantly for higher gas temperatures. For this validation case, both velocity and temperature measurements with LITA are compared to a second, established measurement technique, namely pitot and total temperature probes. The investigation is conducted for three temperature levels characterized by the total temperature at inlet, and are referred to as cold (T_t=292 K), heated (T_t=550 K) and hot conditions (T_t=1100 K).

Examples found in literature are often not comparable with respect to the jet dimensions, featured flow velocities and temperatures or environmental conditions at the test facility used. Especially, investigations for large-scale nozzles and hot inlet conditions ($T_t \geq 1000$ K) are rarely reported. Kozlov et al. used heterodyne detection to investigate a small subsonic jet generated in a 1.5 mm by 22 mm rectangular nozzle [105]. Gas temperatures and flow velocities are obtained up to 600 K and 100 m/s, respectively [104]. Another example for a small nozzle is [127] where similar temperatures and flow velocities are reported.

For larger jets, signal quality reduces drastically due to steering of the beams through the density gradients in the turbulent flow. This effect was identified as main source of distortion in [85]. The investigated nozzle is 15 mm in diameter and, hence, roughly half the diameter of the ITLR nozzles. Therefore, beam steering was a similar constraint for first homodyne LITA measurements at

ITLR [152, 153]. These experiences resulted in using the more powerful, pulsed lasers not only for excitation, but also for the interrogation beam to boost the signal intensity [121]. Such a setup was used for the subsequent work at ITLR, which allowed to investigate free jets up to 550 K inlet total temperature at first [139] and finally up to 1300 K [77, 78]. All investigations were obtained with a homodyne setup and, hence, limited to measure speed of sound and temperature, respectively. Furthermore, the pulse duration of the interrogation beam is too short to observe the signal for its entire lifetime. As a consequence, the grating is induced multiple times, but with an increasing time shift between excitation and interrogation laser. Hence, a different segment of the signal is probed each time [77, 121]. This assembly of the entire signal from segments obtained in multiple shots prevents time-resolved measurements, as such a signal can only represent an average measurement over the entire sampling period. Using a continuous interrogation beam as in this work allows to record the entire signal at each single shot, but must accommodate that the power of the interrogation beam is multiple orders of magnitude lower.

This review shows the relevance of the following investigations as a separate validation case and clarifies the objectives that need to be addressed. As none of the previous studies at ITLR involved velocity measurements, this is a major aspect. Temperature measurements were already compared to probe readings by Rosenko [139], but only for up to 550 K inlet total temperature and for the homodyne setup with pulsed interrogation laser. As the setup used here is heterodyne with a continuous interrogation beam, the temperature measurements are shown for all three temperature levels. Additional homodyne signals were recorded for the hot conditions to supplement the previous work.

Experimental Setup

The free jets were generated using the supersonic nozzle described in section 3.2.1. Table 5.2 lists the inlet conditions for the individual free jets. The advantage of this nozzle is that it produces a pressure-matched free jet with no initial shock and expansion system ($p_{st} = p_\infty$). This allows to use intrusive probing in a supersonic flow, as it is possible to correct the measurements for the bow shock generated by the presence of the probe.

Commercial probes were used for the cold and heated jet. A combination of pitot and total temperature probes allows to determine the flow Mach number and the static temperature. The data processing is presented in more detail in appendix A together with an analysis of the respective measurement uncertainty as function of the initially measured quantities. For the hot jet, special high temperature resistant probes were developed as part of this thesis. Equivalent performance of both probe sets was verified in a separate evaluation described in appendix B. For the measurements, the probes were mounted on a motorized three-axis traverse that also held the LITA setup. This allowed to investigate the free jets with both techniques on the same test run to eliminate day-to-day variation of the test facility. Furthermore, it reduced the uncertainty in the measurement position relative to each technique.

The LITA setup used heterodyne detection and a 700 mm focusing lens for the cold and heated jets. For the hot jets, a 1000 mm focusing lens was required due to the available bandwidth of the detector. This results in a slightly larger fringe spacing of ≈30 µm than used so far. Again, a frequency analysis was used to determine dominant frequencies in the LITA signal and to derive the velocity and the static temperature simultaneously. This involves the iterative procedure to find $\gamma(T)$ for a given speed of sound at an a priori unknown static temperature as described in section 4.2.3.

Following the discussion in section 5.2, the theoretical model is not used for heterodyne signals. Instead it is used to post-process the homodyne signals recorded for the hot free jet. This demonstrates that the theoretical model is also applicable for high temperature investigations and represents a consistent supplement to the work in [139].

Measurements were taken at three planes downstream of the nozzle exit at $X/D = 1$, 3 and 5, where D is the diameter of the nozzle exit. For each plane, measurements are taken in radial direction starting from the symmetry line. The radial positions are normalized by the exit radius R of the nozzle.

Results

The Mach number and static temperature distributions (normalized by the ambient temperature) obtained for LITA and the probes are shown in figures 5.6, 5.7 and 5.8 for the cold, heated and hot free jet, respectively. The values

	T_t [K]	p_t [kPa]	T_∞ [K]	p_∞ [kPa]
cold	292	352.4	294	96.0
heated	550	350.6	295	95.5
hot	1110	354.0	292	96.5

Table 5.2: Flow parameters for the supersonic free jets

represent the mean of 16 measurements for the cold and heated jet, and 10 for the hot jet. LITA measurements are presented together with the sample standard deviation of the mean. So far the 95 % interval was chosen to indicate the uncertainty in the measurement as the random error in those measurements was the main source for variation. However, free jets feature a much higher turbulence than the flows in the validation cases shown before, which causes a true scatter in the measurement. The standard deviation is used here instead to highlight that the variation is a feature of the observed flow rather than the measurement itself. The temporal resolution of the probes is not sufficient to resolve fluctuations in the flow. Therefore, the absolute uncertainty due to the measurement error as derived in section A.3 is shown. This also provides a scale to rate the deviations between both techniques.

The same LITA setup was used for the cold and heated free jet. The signal-to-noise ratio was approximately 30 for the cold free jet and decreased to 10 for the heated jet due to reduced signal intensity and lifetime . This decrease prohibited experiments in the hot free jet without refinements of the setup. In a second measurement campaign, the improved setup yielded values in this range for the hot free jet as well. As adjustments in the setup were required, the temperature dependency of the LITA signal intensity could not be fully investigated. Instead it was made the object of a separate study and is addressed in more detail in section 6.3.2.

For all free jets, a core flow with approximately homogenous flow conditions in radial direction is found. This region diminishes for axial positions further downstream, as the mixing process between the core flow and the ambient air results in a growing shear layer. Figure 5.9 compares LITA measurements for all temperature levels at an axial position of $X/D = 3$ to illustrate the effect of the inlet total temperature on the jet dimension. The thickness of the shear layer increases visibly with the inlet temperature. It is also shown that the Mach number in the core flow is almost constant and that the inlet temperature mainly causes a static temperature variation as intended. The comparison of both techniques shows a consistent result for all temperature levels. The best agreement between LITA and probe measurements is seen for the core flow, while the discrepancy increases for the shear layer. However, this is expected as the probe tips represent a large obstacle in this flow region. With head diameters of a few millimeters, they are in the order of the shear layer thickness. Furthermore, the subsonic speed allows the information of the blockage to travel upstream. Both effects cause a low spatial resolution for the probes. On the other hand, the test volume contributing to the LITA measurement is approximately 300 µm. Therefore, a better spatial resolution can be expected for the LITA technique. The largest deviations are, in fact,

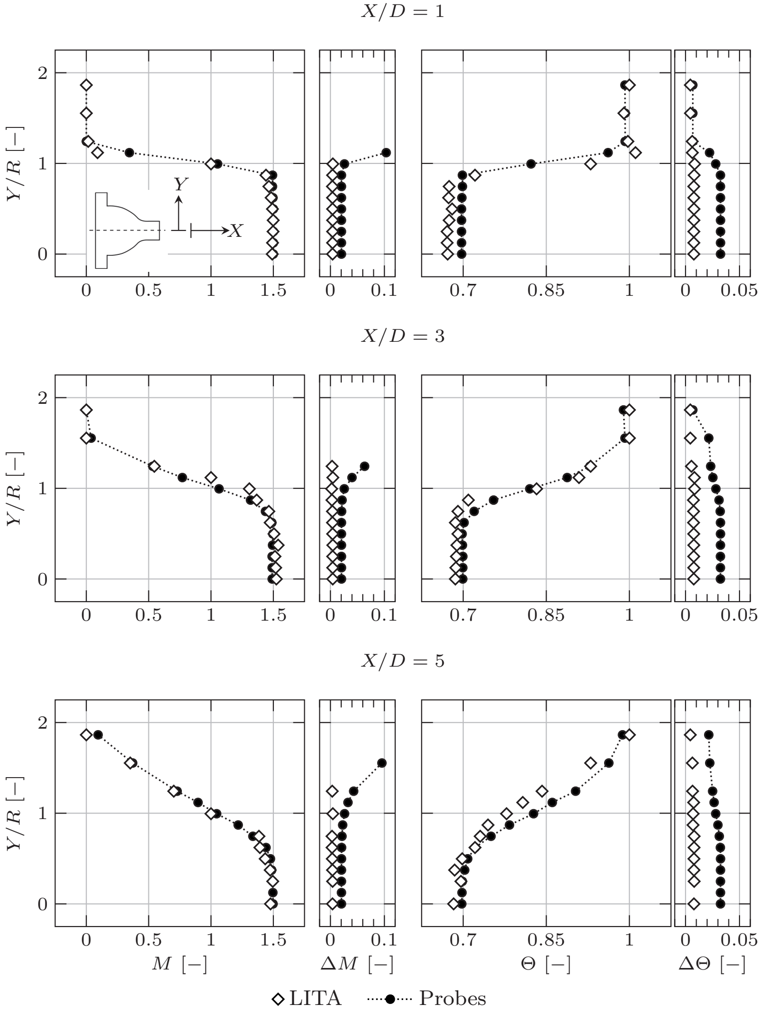

Figure 5.6: Mach number and temperature distributions together with their associated measurement uncertainties for the cold free jet

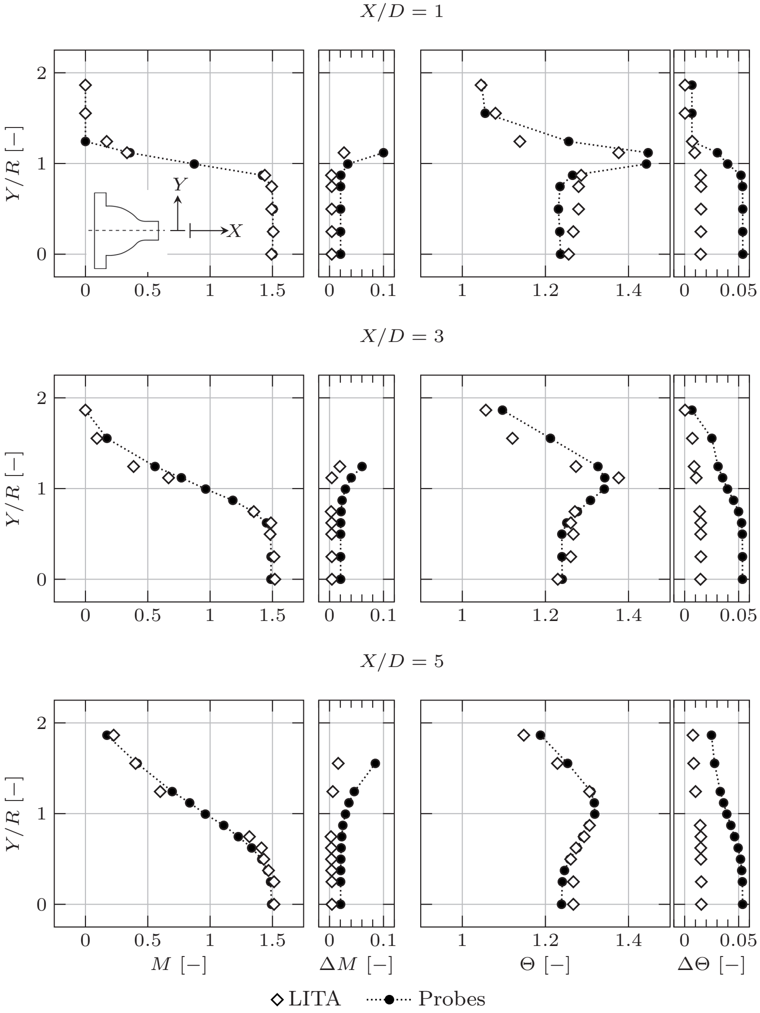

Figure 5.7: Mach number and temperature distributions together with their associated measurement uncertainties for the heated free jet

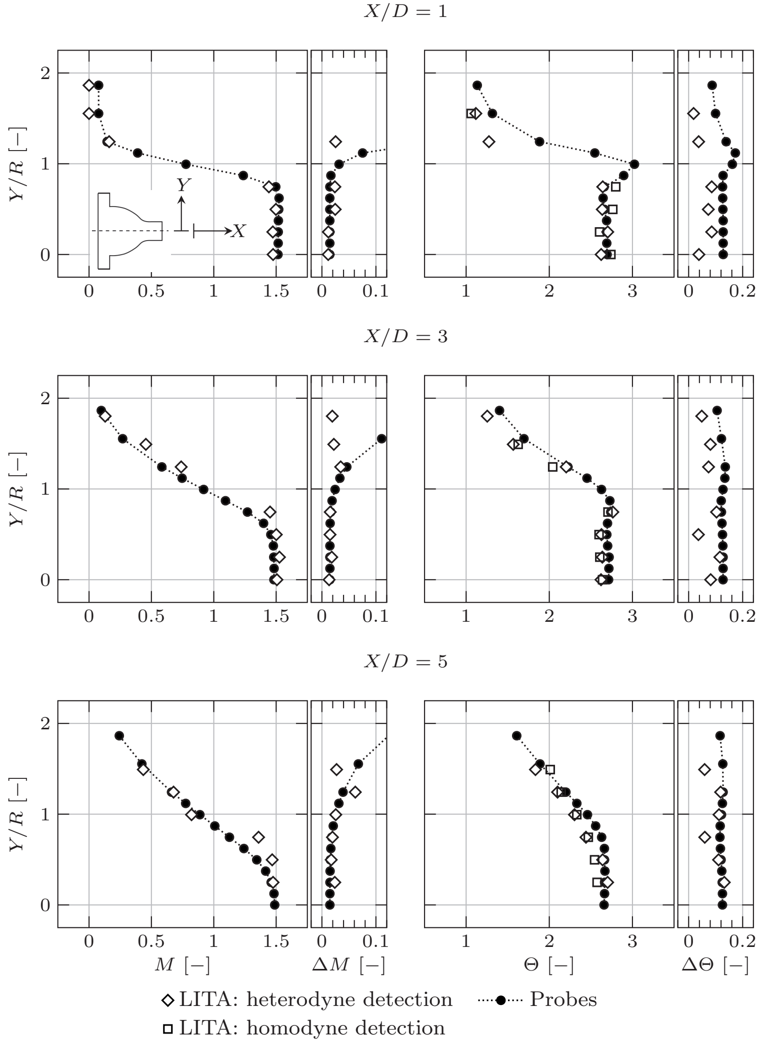

Figure 5.8: Mach number and temperature distributions together with their associated measurement uncertainties for the hot free jet

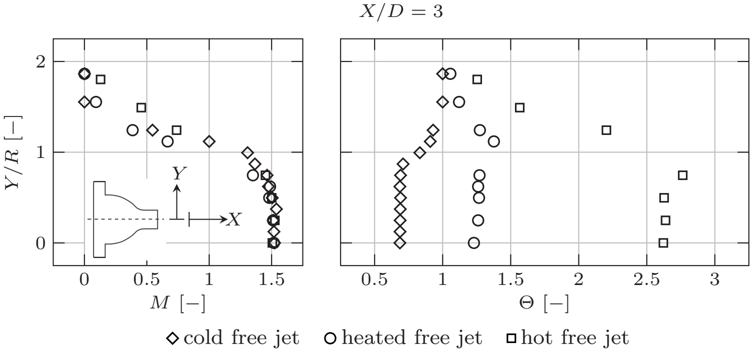

Figure 5.9: Mach number and temperature distributions compared at $X/D = 3$ for the cold, heated and hot free jets

found in regions, where the flow field features steep gradients. Keeping this in mind, a meaningful comparison between both techniques is only possible for the core flow.

Table 5.3 lists all parameters measured at $X/D = 3$, $Y/R = 0$ for all free jets. The overall deviations stay within 2.5 % and 4 % for Mach number and static temperature, which provides a more quantitative comparison in addition to the profiles presented in the figures. Looking at the absolute values, the deviation in temperature seems more than proportional for the hot case. However, this is set in perspective by stating the probe's uncertainty at this position, which is approximately 40 K. As mentioned above, homodyne signals were recorded for the hot jet and are included in figure 5.8 and table 5.3. These signals are

	cold jet	heated jet	hot jet
M_{Probe}	1.491	1.487	1.480
$M_{LITA,heterodyne}$	1.524	1.519	1.506
T_{Probe}	205.5 K	365.8 K	791.3 K
$T_{LITA,heterodyne}$	201.7 K	362.9 K	765.6 K
$T_{LITA,homodyne}$	n/a	n/a	770.8 K

Table 5.3: Comparison of probe and LITA measurements at $X/D = 3$, $Y/R = 0$ for the cold, heated and hot free jets

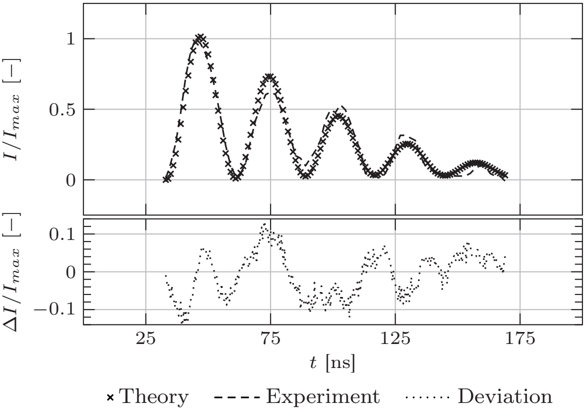

Figure 5.10: Comparison of recorded and theoretical signals for the hot free jet: $X/D = 3$, $Y/R = 0$

post-processed using the theoretical model fit. To improve signal quality, the recorded signals were averaged before fitting. For this reason, no information on the variation of the homodyne measurements is given in figure 5.8. However, a good agreement is found between both the heterodyne and homodyne LITA measurements and the probes. The comparison between the experimental and theoretical signals as illustrated in figure 5.10 shows deviations less than 15 % as for the measurements in the static argon atmosphere. That demonstrates that, even under harsh test conditions, LITA signals are of sufficient quality to apply the fitting procedure. To avoid confusion about the similar frequency of the signal here and in figure 5.1, the reader should be reminded that a 1000 mm instead of the 700 mm focusing lens is used for the hot jet. Therefore, the fringe spacing is larger and the same frequency represents a by the factor of 10/7 higher speed of sound in this case.

5.4 Summary

As the valdiation included several objectives, a short summary is presented for this chapter. The following statements were verified:

I. LITA is capable of very accurate speed of sound measurements.

II. LITA velocimetry is verified for sub- and supersonic flows.

III. Both post-processing approaches are demonstrated and are shown to provide comparable results: The frequency analysis requires less computational effort and is better suited for low quality signals. The potential of the theoretical model is to include additional measurement parameters in the future.

IV. It is shown that the presented LITA setup is competitive to the state of the art that is found in literature. The literature review shows that the presented reference cases are not only valuable as validation for the following applications, but also represent a contribution to the current state of the art itself.

V. A comprehensive study of large-scale, supersonic free jets at different temperature levels is presented to verify LITA against an established measurement technique.

VI. The presented LITA setup obtains reliable measurements not only in a laboratory environment, but also for extremely harsh environmental conditions at the test facility.

VII. The deviations of LITA to the respective references range from 0.2 % to 2.5 % for Mach number and from 0.1 % to 4 % for temperature.

VIII. These results qualify LITA as validated measurement technique for the intended applications.

CHAPTER 6

Application

The LITA technique can contribute to a variety of different fields. Therefore, the focus was set on three different applications that involve compressible flows, namely

I. a chemically reacting H_2/air free jet,

II. the flow field inside the scramjet combustion chamber,

III. shock-heated flows.

The reacting free jet outlines the combustion diagnostics aspect and represents the original application. However, the potential of LITA with respect to the scramjet combustor became clear quickly, and the test campaign was extended to accommodate such experiments. Here, the focus is to obtain detailed experimental data sets used for CFD validation and to characterize the shock system in a supersonic channel flow. This led to the last application, where the motivation is to include another challenging test facility, i.e. a shock tube. Here, the objective is to obtain multiple flow quantities of the post-shock flow field from a single-shot experiment.

6.1 Chemically Reacting Free Jet

The need for a large-scale combustion jet experiment and the challenges involved have already been outlined in section 1.2.4 together with the motivation of this thesis. LITA is suited for combustion diagnostics, but this has been mainly demonstrated for laboratory burners, for instance by Hell [77] and others [12, 72, 81]. Its use for turbulent diffusion flames, as generated at the ITLR combustion test facility, was the focus of the PhD thesis of Hell [77]. The results are summarized in [78], where time-averaged speed of sound measurements obtained for several radial planes downstream of the nozzle exit are presented. First considerations leading to the present work were made by the author during his contribution to [78].

As a consequence, the current work focuses on providing time-resolved measurements to include information on the fluctuating part of the flow field. Such experiments are only possible with the current, improved setup of the LITA technique. Furthermore, simultaneous flow velocity measurements were conducted to supplement the speed of sound data. LITA velocimetry in a reacting free jet is a general new aspect, also with respect to literature.

Experimental Setup

The reacting free jet was generated using the mixing nozzle described in section 3.2.2. The flow parameters are equal to those used in [78] and listed in table 6.1. Hydrogen was injected at an equivalence ratio[1] of $\Phi = 0.4$ with respect to the main air flow in the coaxial nozzle. The choice of equivalence ratio follows the previous considerations detailed in [77], as this ratio results in the most stable and best reproducible flame. It should be noted that the nozzle was operated slightly below its design pressure ratio. This is consistent with previous work and compulsory, as the temperature required for autoignition of the hydrogen is only reached for a reduced air mass flow due to limitations of the heating system. For the optical setup, the 1000 mm focusing lens was used to account for the high speed of sound expected within the combustion zone. Both homodyne and heterodyne signals were recorded. The reaction zone is the only situation in this thesis, where LITA signals arise from thermalization. This is caused by the resonance of the excitation laser with the products of the combustion process, probably dominated by the weak transition lines of H_2O present within the linewidth of the laser. Outside of the reaction zone, signals are purely based on electrostriction again. An interesting aspect to note is that – although temperatures in the reaction zone are higher than for the hot free jets in section 5.3 – LITA signals are stronger here, as the thermal grating is contributing. Homodyne signals were processed using the theoretical model. Recorded and analytical signals show good agreement, comparable to the examples shown in chapter 5. The frequency analysis was used for the heterodyne signals. The flow quantities obtained are presented as arithmetic mean together with the sample standard deviation of the mean to distinguish

---

[1] The equivalence ratio represents the ratio of the fuel and oxidizer mass flows normalized by its stoichiometric value: $\left(\dot{m}_{H_2}/\dot{m}_{O_2}\right) / \left(\dot{m}_{H_2}/\dot{m}_{O_2}\right)_{\text{stoichiometric}}$

	T_t [K]	p_t [kPa]	$\dot{m}$ [kg s^{-1}]
co-flow	1317	284	$187 \cdot 10^{-3}$
injection (H_2)	330	138	$2.19 \cdot 10^{-3}$
ambient	288	95.8	–

Table 6.1: Flow parameters for the reacting free jets

between the mean and fluctuating parts of the unsteady flow field. Out of the possible frequencies listed in table 4.2 for resonant heterodyne signals, only Ω_v and Ω_a are always dominant against the noise in the spectrum and, hence, used to determine the flow velocity and speed of sound, respectively. For some measurement positions, also a weak contribution at Ω_{-a+v} is found. A comparison of the derived flow quantities with the ones using Ω_{-a+v} yield reasonable agreement with deviations within the variation of the measurements.

Results

Figure 6.1 shows a photographic image of the resulting flame. The schematic of the combustion zone shows that reaction starts approximately at $X/D = 7.5$ and reaches up to $X/D = 11$. In radial direction, it extends to $Y/R \approx 1$. The dimensions of the reaction zone is based on OH^*-chemiluminescence images obtained for [78]. Here, the natural emission of excited hydroxide produced in the combustion process is used as indicator for the schematic in figure 6.1. The intensity of the emission is represented by the isolines. This defines the region of interest for the LITA measurements.

Figure 6.2 shows the speed of sound profiles at $X/D = 8$, $X/D = 10$ and $X/D = 12$. All measurements were obtained with homodyne detection. For the $X/D = 8$ plane, the speed of sound profile is also shown for a non-reacting free jet where air instead of hydrogen was used for the center jet at comparable inlet conditions. For air injection, a typical self-similar flow profile is found. As the gas composition remains unchanged, the flat speed of sound profile indicates a homogeneous temperature distribution close to the center line. The initially cold center jet has gained enough heat from the hot co-flow to compensate the temperature difference, which suggests good mixing of the two jets. As the inlet conditions of the center nozzle were comparable for air and hydrogen injection, this is seen as an indication for the mixing in case of the reacting free jet.

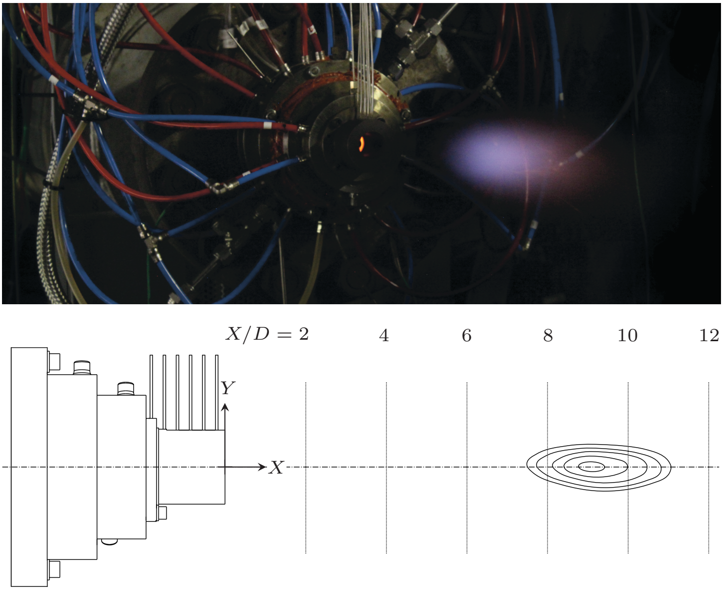

Figure 6.1: Photography of the flame (top) and a schematic view of the reaction zone (bottom)

For hydrogen injection, the combustion starts at the center line, which causes a substantial increase in the measured speed of sound. It should be noted that temperature and speed of sound are independent for the reacting jet, as the mixing of air and hydrogen as well as the combustion process change the gas composition. Towards the outer region of the jet, the values return to the same level as for the non-reacting jet, since combustion takes only place at the center. The heat release and chemical reaction cause large fluctuations in the speed of sound. Hence, the combustion zone is also visible from the variations in the measurement in addition to a higher mean value. Similar to the averaged speed of sound, the fluctuations return to the non-reacting level as the reaction zone is exited in radial direction.

For $X/D = 10$, the flow field near the center line is more homogeneous with fluctuations comparable to the non-reacting case. This indicates a less intense combustion and is consistent with the OH^* image where the combustion peak is seen at $X/D \approx 9$. The only sharp increase with respect to the first plane is

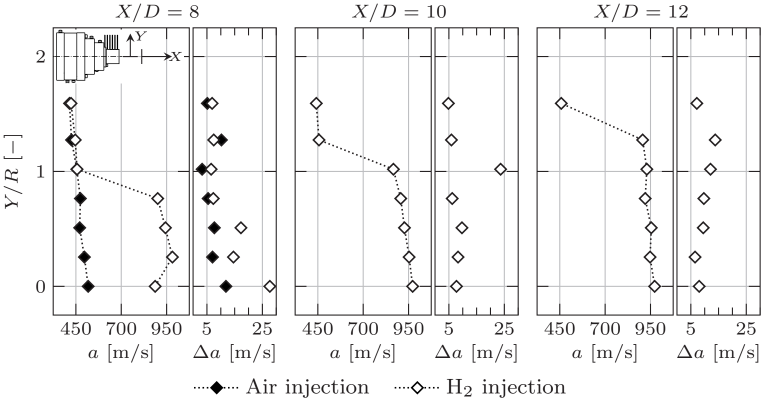

Figure 6.2: Mean and fluctuating parts of the speed of sound profiles at different axial positions in the reacting free jet

found at $Y/R = 1$. Reaching the same level of fluctuations as at $X/D = 8$ for the center line, the start of combustion may be assumed. This is supported as the position matches the maximum radial extension of the reaction zone found for the OH^* image.

The fluctuations decrease as measurements are obtained further downstream at $X/D = 12$. A slight raise is only visible where intense combustion takes place in $X/D = 10$. In general, the main reaction is decaying and the released energy is received by the flow field. Going through the plots from left to right the region of high fluctuations sweeps from the center line to the outer region of the free jet, which correlates with the OH^* image.

The measurements were repeated for $X/D = 10$ using heterodyne detection. Figure 6.3 shows the speed of sound, flow velocity and Mach number distributions that are obtained simultaneously from a single measurement. For the speed of sound, the profile obtained with homodyne detection is added. The comparison shows close agreement in both the arithmetic mean and the standard deviation of the mean of the measurements. Hence, the results are reproducible for both detection schemes. The comparison also eliminates the ambiguity in the assignment of the beat frequencies, as Ω_a is stated explicitly.

The velocity profiles follow the shape of the speed of sound distribution. The maximum velocity is found for the center behind the combustion zone. The

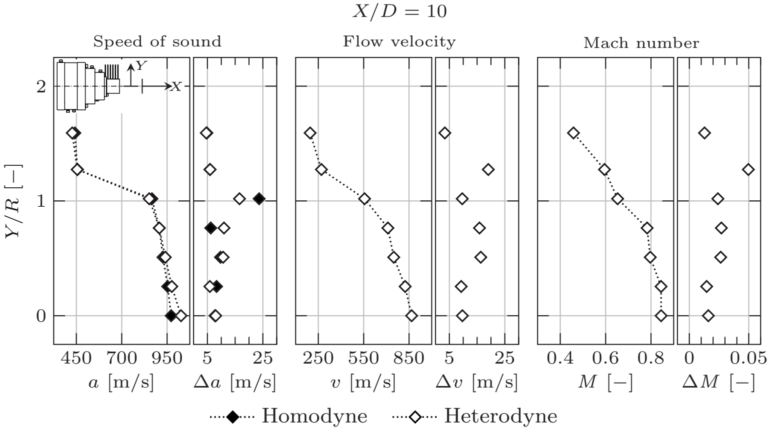

Figure 6.3: Mean and fluctuating parts of the speed of sound, flow velocity and Mach number profiles at $X/D = 10$ in the reacting free jet

fluctuation level increases in radial direction, where measurements are taken inside the shear layer region.

Similar to the velocity profile, the Mach number also shows the typical profile of the self-similar flow regime. The flow remains subsonic throughout the entire profile, including the combustion zone. This is, however, expected given the great distance to the nozzle exit, but the clear classification as subsonic combustion is only possible with the new setup using heterodyne detection.

This represents the first velocity measurements that are obtained for the reacting free jet experiment at ITLR. Furthermore, it is not known to the author that LITA velocimetry has been reported for such an experiment before. Given that suitable reference experiments of this kind are rare as outlined in section 1.2.4, the motivation to obtain more experimental data sets for CFD validation is clear. Furthermore, it proves the potential of LITA in obtaining such data.

6.2 Scramjet Combustion Chamber Flows

The need for experimental data is not limited to the free jet experiment. For the combustion chamber, experimental data are also crucial for the characterization of the flow field and the validation of CFD computations. So far, data acquisition for the ITLR combustor included qualitative visualization of the flow field and the reaction zone via schlieren and visual imaging or OH^* chemiluminescence.

Quantitative data are restricted to wall pressure distributions, which are commonly used to validate numerical computations. However, the pressure taps are often widely spaced and located only along the symmetry plane of the channel. This limits the accuracy to which the flow field is represented. Using the ITLR combustor as an example, it has been shown that certain flow features in the middle of the channel are not reproduced in the wall pressure distribution [51].

This highlights the need for the data sets that can be obtained with LITA. The following experiments were conducted to overcome this lack and provide quantitative data of the flow inside the ITLR combustor for the first time. As said above, this is particularly desirable for CFD validation, but also for detailed studies of the flow field resulting from the injection. Both objectives are pursued in the following. The investigations include the two injection schemes used at ITLR, namely strut and wall injection.

Experimental Setup

An identical LITA setup was applied for both injection schemes using the 700 mm lens. Signals were obtained with heterodyne detection and are processed with frequency analysis to derive temperature and flow Mach number. Measurements were obtained in vertical direction to present flow profiles at different axial positions relevant to the investigated injection scheme.

6.2.1 Strut Injection

Strut injection is a promising concept, as it allows to inject the fuel directly into the center and parallel to the main flow field. The strut injector used at ITLR is shown in figure 6.4. It is 86 mm long and 40 mm wide, with a maximum height of 7 mm. The first half of the strut is shaped as a wedge with a sharp leading edge. The trailing edge is lobed to introduce streamwise vortices that increase the mixing of the fuel and main flow [59]. Fuel is injected into the main flow via five horizontal slots in the trailing edge. Small Laval nozzles are integrated at the exit to accelerate the fuel to a nominal injection Mach number of 2.

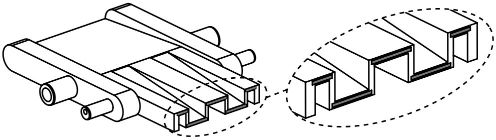

Figure 6.4: Schematic view of the strut injector (adapted from [51])

The main objective of this investigation is to provide more sophisticated data sets to validate the OpenFOAM solver developed by Dröske [40]. For this reason, the experiments were conducted in the modular supersonic channel built for this validation instead of the original combustion chamber. As said in section 3.3.3, the geometry of the two channels is identical except for the constant cross section of the new channel. This change in design has, however, negligible implications for the presented results.

The inlet nozzle of the channel accelerates the main flow up to Mach 2.5. The trailing edge of the strut is 461.5 mm downstream of the nozzle throat. Measurements were obtained for two vertical planes along the symmetry plane of the channel. The first plane is located 75.5 mm upstream of the strut leading edge and the second 28.5 mm downstream of the trailing edge (see sketch in figure 6.5). Two sets of measurements were obtained for the second plane, one for the distorted main flow only and another with the air injection activated. At each measurement position approximately 30 signals were recorded. Additional experimental conditions are listed in table 6.2.

Figure 6.5 illustrates the obtained Mach number and temperature profiles together with the numerical predictions provided by Dröske [40]. For each measurement position, the mean value and the variation expressed as one standard deviation of the mean of the measurements is shown. Details concerning the developed solver and numerical setup are given in [40].

For the undistorted flow upstream of the strut injector, the characteristic flow field of a fully developed turbulent channel flow is found. Experimental and

	T_t [K]	p_t [kPa]	M [-]
main flow	500	700	2.5
injection	300	700	2.0

Table 6.2: Experimental conditions: strut injection

numerical profiles match well for both Mach number and static temperature. The slight asymmetry in the experimental profiles is caused by small imperfections in the manufacturing and alignment of the channel modules, resulting in weak shocks that originate at the joints [40].

The flow field downstream of the strut features a velocity deficit in the wake of the strut if no air is injected. This is resolved in both the experiment and the simulation. While the simulation generally predicts higher velocity, the

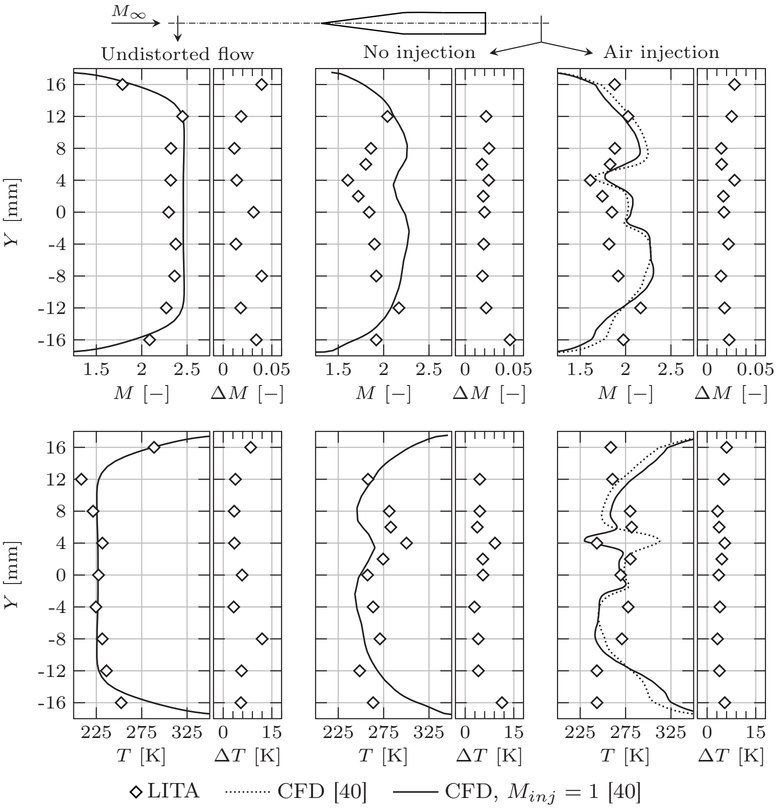

Figure 6.5: Flow profiles upstream and downstream of the strut injector: LITA measurements in comparison to numerical predictions

shape of the profile matches the experimental data. This is consistent with the temperature profiles as higher temperatures are found in the experiments.

Once the air injection is activated, the predicted velocities decrease, but remain higher than the measured values. However, a slightly better agreement between the simulation and the experiment is found. For the static temperature, the LITA measurements show a local temperature dent at $Y = 4\,\mathrm{mm}$. The position coincides with the cooler injection jet originating from the middle slot in the strut. This temperature drop is not observed for the initial simulation (dotted line), which used the nominal injection Mach number of 2 for the internal flow in the strut. This follows the original design of the strut injector, where small Laval nozzle accelerate the injected fluid. However, these nozzles are likely to degrade due to thermal stress during the experiment. Previous studies, e.g. in [181], accounted for this effect by setting the injection Mach number to unity. This approach was used in the second simulation (solid lines in figure 6.5). Now the corresponding temperature profile also exhibits the pronounced temperature drop due to the increased injection mass flow for the sonic exit condition.

This clearly shows the benefit of quantitative data sets for validation. Details as the degradation of the injector and the resulting variation of the injection Mach number would not have been detected with the measurement techniques used so far at ITLR. However, it is important to take this into consideration, especially when the combustion is simulated, as the varying fuel mass flow will have significant influence on the reaction. The validation of more advanced numerical solvers like the one presented requires more sophisticated experimental data sets which can be provided by the LITA technique.

6.2.2 Wall Injection

The second investigated injection scheme is wall injection. In the experiments, air is injected from port holes in the top and bottom wall. This results in two injection jets that penetrate into the supersonic main flow and create a distinct shock pattern. This work is motivated by the publication of Herring et al. [84] where an oblique shock originating from a solid wedge model is investigated. As their focus is the comparison of LITA with a second Doppler-based velocimetry technique, the shock discontinuity is probed with rather coarsely spaced measurements in one direction. Furthermore, the flow field features only a single oblique shock in contrast to the more complicated shock system presented here. For these experiments, the actual combustion chamber as described in section 3.3.2 is used together with the Mach 2 inlet nozzle. The axial position of the injection hole is consistent with the trailing edge of the strut injector in the combustor at 513 mm downstream of the nozzle throat. The experimental conditions are summarized in table 6.3.

Figure 6.6 shows a schlieren image of the resulting flow field. As the flow field is symmetric to the center line, the upper part is replaced by a schematic view of the schlieren image to highlight prominent flow features found in the schlieren image. The schematic view corresponds to figure 2.4 in chapter 2. Bow shocks (solid line) form in front of the top and bottom injection jets. The shocks extend towards the center and intersect at the center line. They further propagate to the opposite wall, where the reflection is observed as a typical shock bifurcation [101]. The bow shocks frame the mixing zone of the injection and the main flow. Details in the jet are difficult to see, but the overall evolution of the jet is identified. After the shock intersection the flow field accelerates. This is best seen along the center line, where the brightness gradually increases from the intersection point towards the right border of the image. The increase in brightness corresponds to the change in gas density associated with the acceleration of the flow. Towards the wall, this region of accelerating gas is bordered by an expansion fan (dotted lines). The fan probably originates in the mixing region, but is only clearly visible after the bow shock from the opposite wall has passed.

It should be mentioned that the schlieren image was recorded for an unheated main flow to avoid distortions due to the heating of the windows. However, the effect on the shock positions is negligible, so that a good qualitative illustration of the flow field is provided by the schlieren image.

To provide a scale of reference, an object with known dimensions was placed in the picture. This allows to illustrate the measurement positions for LITA in the schematic view as red grid lines. Starting from the center line, measurements were taken every 2 mm towards the wall. Such flow profiles are obtained for several planes downstream of the injection point at an increment of 10 mm in axial direction. In comparison to section 6.2.1 a finer grid was possible for the same number of points, as measurements were only taken in one direction due

	T_t [K]	p_t [kPa]	M [-]
main flow	500	400	2.0
injection	292	1500	1.0

Table 6.3: Experimental conditions: wall injection

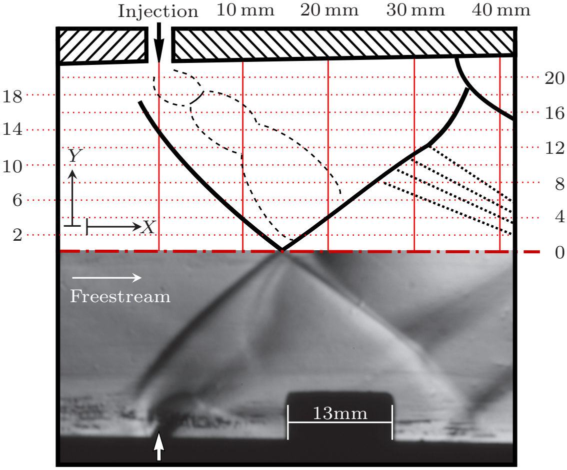

Figure 6.6: Visualization of the flow field for top and bottom wall injection

to the symmetric flow field. Furthermore, the absence of the strut mounting provides better access to the flow field directly at the injection.

The following discussion focuses on the Mach number distribution of the flow field. The corresponding temperature field was obtained simultaneously from the measurements. Since the temperature distribution shows an analogous trend to the velocity field, it is not shown to limit the discussion to the essential. The variation in the measurement is found comparable to strut injection and is, for that same reason, not included here.

Flow Field of the Shock and Expansion System

Figure 6.7 illustrates the measured Mach number profiles. The diagrams show the profiles at the injection point as well as 10, 20, 30 and 40 mm downstream of it. Measurements of the first and last planes were repeated for the channel flow without the injection. To support the interpretation of the flow field, the schematic view as shown in figure 6.6 is added to the background. It is scaled such a way that the y-axis ticks of the plot match the vertical scale. Furthermore, the width is adjusted to align the center of each plot with the corresponding axial position. To avoid misinterpretation, it should be stressed that the measured Mach number profiles only represent the vertical distribution

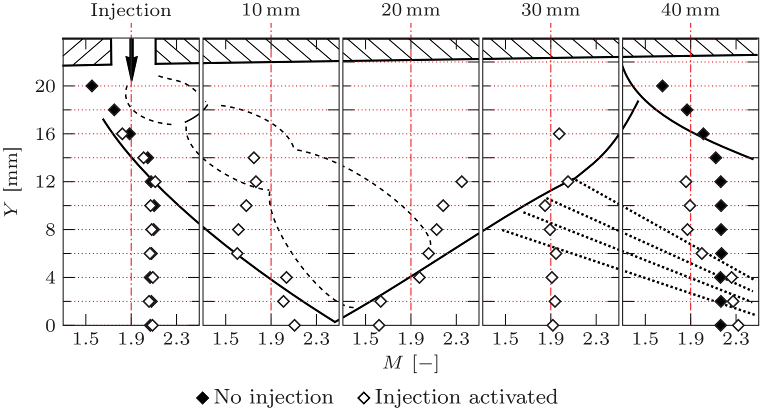

Figure 6.7: Mach number profiles measured with and without wall injection

at the discrete axial positions labeled "injection, 10 mm, 20 mm, 30 mm and 40 mm".

Without the injection (filled symbols), a fully developed velocity profile of a turbulent channel flow is found. Due to the slightly diverting cross section of the combustion chamber, the flow gradually accelerates throughout the channel. The acceleration corresponds to an increase of the center flow Mach number from 2.05 at the point of injection to 2.15 at the last plane 40 mm further downstream.

If the injection is activated (empty symbols), the velocity profile in the first plane remains unchanged. This is expected and nicely illustrates the nature of supersonic flow. As information cannot propagate upstream, the flow field at the injection plane is not yet aware of the injection. The border of this information is represented by the bow shock. This is not entirely in agreement with the schematic illustration, as this predicts a crossing of the shock front at $Y = 14\,\mathrm{mm}$. However, it should be kept in mind that the schlieren image is not taken under the same experimental conditions and is merely intended for a qualitative visualization of the flow field. Instead the LITA measurements show an unaffected flow field up to $Y = 16\,\mathrm{mm}$.

At the next plane 10 mm downstream, the center flow is still unaware of the injection. Heading towards the wall, however, a sharp drop in velocity is found, which coincides with the passing of the bow shock. Further towards the wall, the velocity profile remains constant at first, but shows a small bulge once the mixing region is reached.

The 20 mm plane features the lowest velocity at the center line, as it is directly after the intersection of the top and bottom bow shock. The velocity jumps back to higher Mach numbers once the second bow shock is passed in vertical direction. The distribution in the mixing zone shows the first half of the bulge found at the previous plane. Closer to the wall no signals could be obtained, probably due to the high turbulence level in this region. In general, a strong acceleration is found in the mixing region that results from the low velocity in the center.

The flow field of the 30 mm plane is similar to the previous plane. As the shock has migrated further towards the wall, the step increase is shifted in vertical direction. However, the difference across the shock is less than for the plane before as the center flow accelerated again. A slight additional increase in velocity is found once the measurements are taken in the expansion fan.

The effect of the expansion fan is, however, more pronounced for the 40 mm plane. Here, it causes the highest velocities observed, which exceed even those of the undistorted flow. The region outside the expansion fan features a velocity level comparable to the 30 mm plane. For the center line, the velocity increases linearly from the 20 to the 40 mm plane which correlates to the gradient in brightness of the schlieren image.

In general, the positions of the flow features observed in the LITA measurements and the schlieren image agree very well. The LITA measurements suggest a slightly less steep bow shock, which is consistent with the expectation for a higher inlet total temperature. It shows that a very detailed characterization of the flow field is possible. This is not only desirable for CFD validation, but also for experimental mixing studies, if different gases are used for the main flow and the injection.

Velocity Evolution through the Shock Front Discontinuity

Besides the velocity measurement, a major improvement of the new setup is its capability for time-resolved, single-shot measurements. Provided that it is possible to take measurements while the translation table is continuously in motion, traversing at low speed would result in a very high spatial resolution. In the following this approach is used to accurately detect the position of the shock and to resolve the step change in flow velocity in the vicinity of the shock. It should be noted that this requires an even more rigorously aligned system.

Otherwise, the laser beams pass through the windows at slightly varying angles as the system traverses, which causes severe beam steering.

For this experiment, as illustrated in figure 6.8, the translation table was set to traverse firstly in axial direction from $X = 10\,\text{mm}$ to $X = 20\,\text{mm}$. The path was vertically shifted by 1.3 mm off the center line to probe the bow shocks of the top and bottom wall injection separately. For the second part, the translation table was gradually lowered for 6 mm to pass the bow shock again and probe inside the mixing region. The path is indicated in the schematic flow field in figure 6.8 but not shown to scale for the sake of clarity.

The Mach number evolution in axial direction shows two separate shocks identified by a distinct drop in flow velocity. The Mach number at the start and ending point matches with the profiles shown in figure 6.7. Furthermore, the better spatial resolution shows that the Mach number remains approximately constant prior to the first shock. Afterwards, the flow velocity increases linearly with axial position. The velocity drops again due to the second shock, but increases at the same rate as before the second shock. The Mach numbers at the

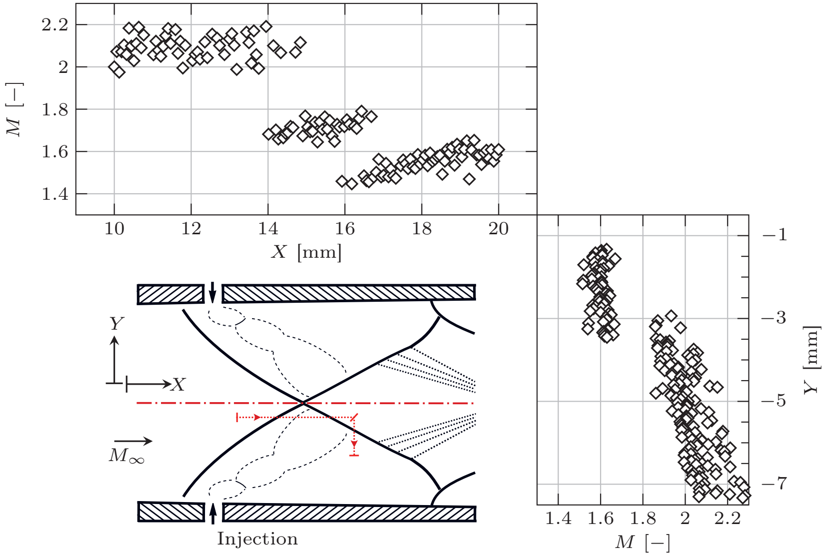

Figure 6.8: Mach number distribution through the shock front in axial and vertical directions

centerline of the 20 mm and 40 mm planes in figure 6.7 match an extrapolation based on this gradient. This suggests that the flow accelerates at a constant rate after the intersection of the bow shocks.

As for the axial direction, the Mach numbers obtained for the vertical direction compare well to the measurements at discrete vertical positions. Again, the Mach number remains constant downstream to the shock but increases instantly once the shock is passed. As for the 20 mm plane in figure 6.7, the velocity further increases towards the wall. The hypothesis of a higher turbulence level in the mixing region is supported by a visible increase of the variation in the measurements.

The presented Mach number distributions represent measurements not only close to the shock, but directly through the shock front. While the shock passage is accompanied by a step change in flow velocity, all shocks show a certain overlap region, where flow velocities at the pre- and post-shock levels are found. Although beam steering due to the shock front might cause this effect, this is ruled out as it would affect the axial and vertical directions differently. Instead it is suggested that the overlap region resolves a periodic shifting of the shock fronts. This behavior is known to exist from high-speed imaging, but has not yet been quantified. Based on the overlap region variation, a continuous shifting of the shock position of up to 1 mm is expected.

6.2.3 High Temperature Application

The previous results demonstrate the potential, but are obtained at comparatively low temperatures with respect to the combustion chamber. The next obvious step is to increase the inlet total temperature to allow for combustion experiments in the scramjet combustor.

This is very challenging for several reasons. Firstly, the signal intensity improves with increasing pressure and decreases with increasing temperature, as investigated in more detail in section 6.3.2. Estimating the applicability of LITA for combustion experiments in the scramjet combustor, the expected temperature level would be comparable to the reacting free jet experiments in section 6.1. In contrast to a free jet, however, the static pressure level in the combustion chamber is well below ambient, which causes even lower signal intensities. To mitigate this penalty, the Mach 2 instead of the Mach 2.5 nozzle is selected for these experiments, as this results in about 20 % higher static pressure for the respective design conditions at the inlet.

Secondly, windows are required for ducted flows to provide optical access. This limits the output power of the excitation laser to the damage threshold of the windows, which is below the setting used for the reacting free jet. Moreover, refractions of the beam at the glass surface causes additional stray light. The 700 mm instead of the 1000 mm lens used for the free jet is chosen to increase the spatial separation of the beams for a given distance. However, this also results in a finer fringe spacing, which is prone to diffuse more quickly due to turbulence.

Thirdly, there are practical implications for these experiments. For the free jet, it is possible to traverse the LITA measurement point out of the jet and adjust the beam paths to restore a strong signal. The available range of the translation table prevents the same approach for the combustion chamber. Therefore, it is essential that the initial alignment sustains over the entire heat up period of the facility. Otherwise, the test day has to be cancelled as the time required to cool the facility down, realign and restart the heating again exceeds the allowed operation time per day. This represented the biggest constraint, although it would be easy to address in a future campaign, for instance by extending the range of the translation table or shorten the heat up time for a refurbished heater.

For the given reasons, a full investigation of the injection at hot conditions was not pursued. Instead the following is seen as feasibility study to demonstrate that measurements at these conditions are possible, yet require a more rigorous preparation than possible within this experimental campaign. Measurements in the flow without injection were obtained in the symmetry plane at the axial position of the injection, hence 513 mm downstream of the nozzle throat. The inlet total temperature was gradually increased starting from 300 K up to 1250 K, which represents the nominal inlet condition for a combustion experiment. As stated above, the Mach 2 nozzle is used at its design inlet total pressure of 400 kPa.

Figure 6.9 shows the measured static temperature versus the respective total temperature at the inlet. The LITA measurements are compared to static temperatures calculated with the isentropic flow equation 2.4. For this purpose, the flow Mach number at the measurement position is used together with the ratio of specific heats γ found again via an iterative procedure. Measured and calculated temperatures agree well at first, but show a distinct trend to deviate for an increasing inlet total temperature. The lower diagram in figure 6.9 shows this deviation with respect to the 95 % confidence interval of the measurement. The comparison shows that the deviation becomes statistically significant as temperature increases. This is expected, as the isentropic equations assume

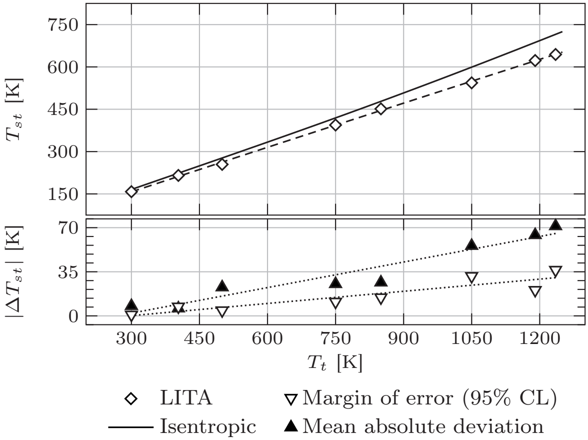

Figure 6.9: Static temperature at $X = 513\,\mathrm{mm}$ for increasing total temperature at inlet

adiabatic walls and a constant total temperature. Instead the walls are water cooled in the experiment, which causes a heat loss through the cooled walls even in the center flow for increasing total temperature. Therefore, it is demonstrated that LITA measurements are also possible for the design inlet conditions of a combustion experiment in the scramjet combustor. The uncertainty of less than 6 % for the 95 % confidence level shows that LITA is a competitive diagnostic tool for such experiments if the aforementioned practical implications of the translation table and test facility are addressed.

6.3 Shock-Heated Flows

The investigation in section 6.2.2 already shows the potential of LITA for shock detection and resolving the discontinuity in flow properties associated with the shock. This suggests to apply the LITA technique for shock tube facilities, where shock waves are used to establish the desired experimental conditions. Quantitative measurements are challenging due to high temperature and pressure environments. In addition, the very short test duration of such impulse facilities requires fast-response techniques. This implies a precise timing between the test facility, the measurement technique and the data acquisition. Acquiring multiple flow properties is desirable as turn-around times and operational costs may be considerable.

The application of LITA in a shock tube experiment follows the original intentions of Cummings and co-workers to develop LITA for measurements in CalTech's T5 shock tunnel [89]. This ambition, however, has not yet been fulfilled for various reasons and it is, hence, the first time to the author's knowledge that non-resonant, heterodyne LITA is used to determine multiple flow quantities in different post-shock flows.

Experimental Setup

Table 6.4 lists the 12 investigated nominal conditions. The test matrix included the test cases argon (cases C1-C6) and nitrogen (C7-C12) at different flow conditions. It was intended to create flow conditions at four temperature levels for different pressures to provide a reasonable variety in test conditions for the LITA measurements. This included measurements in the post-shock flows after both the incident (state 2) and reflected shock wave (state 5).

To generate the conditions in table 6.4, a constant Mach number of the incident shock was aspired for each set of experiments, namely 1.96 for He/Ar-Ar and 1.67 for N_2/N_2 experiments. He/Ar represents a 80%/20% mixture of both gases, which corresponds to the original design conditions of the shock tube [165]. Assuming ideal gas behavior for Ar and N_2, the pressure and temperature behind the incident and the reflected shock can be calculated based on the shock Mach number and the inviscid one-dimensional shock theory as introduced in section 2.4.

Heterodyne and homodyne detection was chosen for the LITA setup together with a 700 mm focusing lens. A pressure rise at the first pressure transducer triggered the LITA system and the data acquisition. This ensures that the measurement was always taken at the same time relative to the shock wave. Different time delays were used to trigger the measurement slightly after the incident or reflected shock pass-by. The axial position was 51.5 mm from the end wall for all experiments, which coincides with the position of the last pressure transducer of the test section. Post-processing was conducted via the frequency analysis. Similar to the free jets, the conversion of the speed of sound into static temperature must account for the temperature and – due to the high pressures in this application – pressure dependency of γ. Hence, $\gamma(T,p)$ was found in an iterative procedure using the RefProp database [109] for the given speed of sound.

Case	Driver	Test gas	State	M_s [-]	p_{th} [MPa]	T_{th} [K]
C1	He/Ar	Ar	2	1.96	0.2	600
C2	He/Ar	Ar	2	1.96	0.7	600
C3	He/Ar	Ar	2	1.96	1.4	600
C4	He/Ar	Ar	5	1.96	0.5	980
C5	He/Ar	Ar	5	1.96	2.0	980
C6	He/Ar	Ar	5	1.96	4.3	980
C7	N_2	N_2	2	1.67	0.1	425
C8	N_2	N_2	2	1.67	0.5	425
C9	N_2	N_2	2	1.67	1.0	425
C10	N_2	N_2	5	1.67	0.3	570
C11	N_2	N_2	5	1.67	1.2	570
C12	N_2	N_2	5	1.67	2.5	570

Table 6.4: Design conditions for shock tube experiments

6.3.1 Shock Tube Experiments

Table 6.5 and figure 6.10 contain a summary of the Mach numbers and temperatures obtained with LITA, their corresponding theoretical values and the relative deviation of both. Furthermore, the derived shock Mach number $M_{s,exp}$ on which basis the theoretical values are calculated is included. The pressure p_{exp} was recorded by the transducer located at the same axial position as the LITA measurement and in the same moment as the excitation laser was fired. Figure 6.10 visualizes the different temperature levels (i.e. pressure) behind the incident and reflected shock. The dashed lines refer to the design values in table 6.4. Deviations between theoretical and measured values are given relative to the calculation to allow for a comparison at all temperature levels.

Small inaccuracies in the target filling pressures caused the shock Mach number to deviate from its aspired value. However, a reasonable agreement with the design value was achieved. Furthermore, it must be noted that the speed of sound conversion inherently assumes thermodynamic equilibrium. This is not necessarily the case. Especially for nitrogen, higher temperatures would result in a non-equilibrium thermodynamic state due to vibration relaxation. This would falsify the temperature derived from the speed of sound. For the investigated cases, however, the contribution is sufficiently low to justify the assumption [52].

Case	$M_{s,exp}$ [-]	p_{th} [MPa]	p_{exp} [MPa]	$M_{2,th}$ [-]	$M_{2,meas}$ [-]	T_{th} [K]	T_{meas} [K]	δ_M [%]	δ_T [%]
C1	1.958	0.16	0.14	0.763	0.764	600.0	605.5	0.14	0.92
C2	1.980	0.68	0.63	0.770	0.763	607.9	590.0	-0.97	-2.95
C3	1.984	1.42	1.32	0.770	0.761	611.4	582.0	-1.11	-4.80
C4	1.972	0.51	0.48	-	-	991.4	963.5	-	-2.81
C5	1.971	2.06	2.04	-	-	992.9	980.6	-	-1.24
C6	1.973	4.35	4.17	-	-	999.5	991.7	-	-0.77
C7	1.681	0.11	0.11	0.754	0.760	426.9	435.1	0.68	1.94
C8	1.658	0.44	0.42	0.735	0.725	422.4	419.9	-1.37	-0.59
C9	1.672	0.94	0.90	0.745	0.743	426.2	430.0	-0.24	0.90
C10	1.665	0.29	0.28	-	-	569.9	550.2	-	-3.45
C11	1.666	1.17	1.16	-	-	571.9	576.2	-	0.77
C12	1.671	2.44	2.44	-	-	575.9	596.9	-	3.66

Table 6.5: Mach number and temperature of the post-shock flows: LITA measurements in comparison to analytical predictions

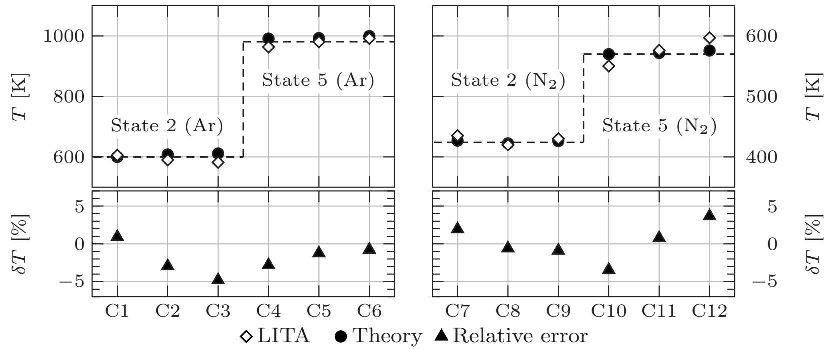

Figure 6.10: Post-shock temperatures: LITA measurements in comparison to analytical predictions

The LITA measurements agree well with the predicted values. The maximum deviation of both post-shock temperatures is within 4.8 %. The Mach number of the flow field induced by the incident shock is measured within 1.4 % of the shock wave theory. Both values are typical for the range determined in the LITA validation.

It should be noted that the true values may also differ from those predicted by the shock wave theory. This is due to non-idealities such as boundary layer effects or shock attenuation. To quantify this deviation independently from the LITA measurement, the experimental pressure p_{exp} measured with a piezo transducer – i.e. a second technique – is included in table 6.5. Compared to predicted values, lower values are found for the measured pressure in all experiments. As pressure and temperature are coupled, an analogous comparison would apply for temperature. This would be consistent with the LITA measurements, as a tendency for too low measured temperature is found. Hence, the exact magnitude of δ_T (and also δ_M) is an interplay between the LITA measurement uncertainty and the inaccuracy of the thermodynamic state value prediction.

Another aspect is the single-shot nature of a shock tube experiment. This differs from the other experiments presented so far, where the test time allows to record multiple signals for the same condition. To reveal variations between two subsequent experiments, measurements were repeated for selected conditions, where the signal-to-noise ratio is expected to be lowest. Further selection criteria are that both test gases and both flow states are represented. A more detailed discussion on the selection process may be found in [50].

The obtained results are illustrated in figure 6.11. For all measurements, the maximum deviation of the flow Mach number and the temperature after the incident shock is $\delta_{max,M2}<1.1\,\%$ and $\delta_{max,T2}<5.5\,\%$, respectively. Averaging could be used to equalize the effect of individual experiments, in which case these values reduce to $\overline{\delta}_{M2}<0.4\,\%$ and $\overline{\delta}_{T2}<0.2\,\%$. For the reflected shock, the

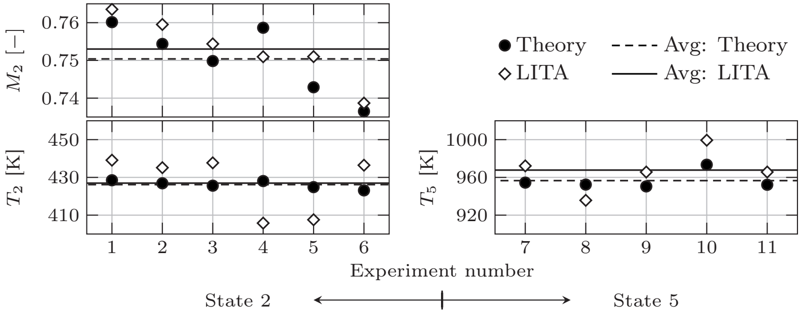

Figure 6.11: Repeated measurements of M_2 and T_2 for condition C7 and of T_5 for condition C4

maximum deviation in temperature is $\delta_{max,T5}$<2.7 % which again reduces to $\overline{\delta}_{T5}$<1.1 % for the averaged values.

This shows that the overall deviation is in the same order as for the complete test matrix and identifies random scattering as main contributor to uncertainty. This is further supported as averaging yields a better agreement, as it is expected for a random variation in the measurement. Although the number of experiments is not sufficient for a statistical analysis, it allows an estimate for the shot-to-shot variation. The sample standard deviation calculates to 1.7 % for Mach number and 3.4 % for temperature behind the incident shock wave. For the post reflected shock temperature, it is 2.7 %. Although a larger number of samples is desirable, this must be seen with respect to the operational costs of the shock tube. Based on an analysis of Gurland and Tripathi [66], the number of samples used represents a good compromise between accuracy and experimental effort, especially since the values are comparable to what is found for the validation in chapter 5.

This assessment evidently proves the applicability of LITA for single-shot measurements in shock-heated flows. The experiments provide the foundation for a further use of LITA as a diagnostic tool in shock tube experiments. It also shows the potential of the technique for other applications with highly transient flow phenomena, where a combined measurement of temperature and velocity is desirable.

6.3.2 Signal Dependency on Pressure and Temperature

Given that signals were recorded for a range of pressures and temperatures, their influence on the LITA signal intensity is analyzed. This is desirable to estimate the applicability of LITA at experimental conditions other than those investigated here. To allow for a meaningful comparison, all signals were scaled with respect to the intensities of the input beams. It should be noted that the excitation beams are not resonant with a molecular absorption line. Therefore, the dependency found applies only to the optical reflectivity of the acoustic grating and will differ in case that thermal gratings contribute to the signal.

Generally, the signal intensity increases with pressure and decreases with temperature. For pressure, a square-dependency is usually accepted and shown for different setups, for instance by Cummings [19]. In contrast to pressure, little is reported on the temperature dependency [83].

The shock tube experiments feature four temperature levels at different pressures. Figure 6.12 shows the amplitude of the first signal oscillation for each experiment. Using the square dependency for pressure, a quadratic fit of the form $c(T)p^2$ is fitted to the experimental data. The coefficient $c(T)$ represents the temperature dependency. In a similar approach, the $c(T)$ of each fit is plotted versus temperature for figure 6.12. A power function represents the best approximation of the observed trend.

For quiescent test gas, a T^{-3} dependency is reported [33, 60, 121], while a faster decay (i.e. $T^{-4.25}$) was found by Schlamp et al. [153] for measurements in a supersonic jet due to turbulent convection and other effects. For these experiments, the signal intensity scales with $T^{-3.4}$, which is in between the reported values. Given that a moving fluid is present for state 2 and a resting gas for state 5 together with the limited number of experiments, this agreement is reasonable.

The $p^2 T^{-3.4}$ dependency found is seen as an estimate for the performance of the LITA setup under different experimental conditions. This quantifies the subjective observation of very low signal-to-noise ratios found for the combustion chamber at hot inlet conditions. Based on this dependency for the observed static temperature of ≈650 K and static pressure of 50 kPa, one must expect a reduction in signal intensity by a factor of ≈50 with respect to ambient conditions. This is an important aspect for the design of future experiments.

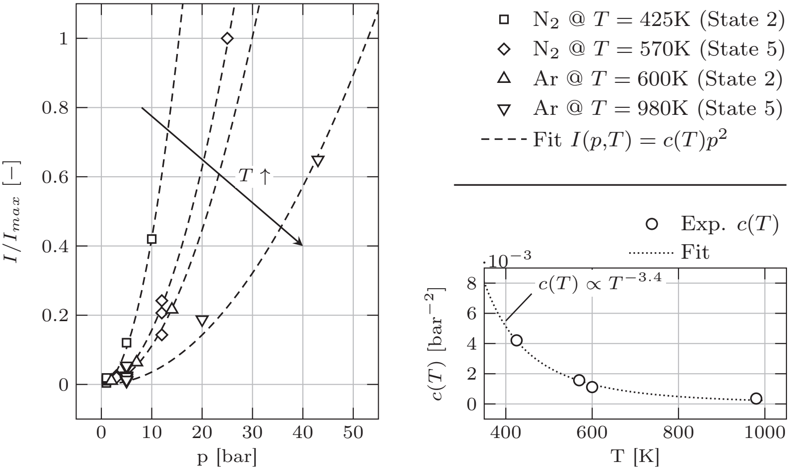

Figure 6.12: Pressure and temperature dependency of the signal intensity

A second benefit is associated with confident knowledge of the $p-T$ dependency. As the temperature can be derived separately from the frequency of the signal oscillations, it potentially allows pressure measurements. For quantitative pressure measurements, however, more detailed experiments focusing on this aspect are required to quantify parasitic effects like, for instance, stray light or the stability of the laser power, which falsify the measurement.

6.4 Summary

LITA is applied to several flow fields with different purposes. The main subjects and contributions in this chapter are summarized in the following:

I. Time-resolved speed of sound, flow velocity and Mach number measurements are presented for the reacting free jet experiment. With LITA velocimetry, subsonic combustion is proven for this experiment.

II. LITA is applied to the scramjet combustor models. Comprehensive data sets are obtained for strut and wall injection. The experimental data are used to validate the predictions of a new numerical solver developed at ITLR. Furthermore, it demonstrates the potential of characterizing discontinuities in a supersonic flow field.

III. Measurements are demonstrated in a scramjet combustion chamber for the hot inlet conditions of a combustion experiment. However, practical limitations restricted a full investigation of the resulting flow field.

IV. LITA is used for off-body measurements in a shock tube facility. Its applicability for shock-heated flows is proven.

V. The temperature and pressure dependency of the LITA signal is investigated. The derived relationship allows to estimate the performance of a given LITA setup for the expected conditions in future experiments.

CHAPTER 7

Conclusion

Within the present thesis, the laser based measurement technique LITA was applied for the investigation of compressible and reacting flows. LITA classifies as seedless and non-intrusive technique. It is capable of obtaining multiple flow properties from a remote, single-shot point measurement. These features make LITA an important diagnostic tool, especially for supersonic flow research.

LITA has already been used at ITLR in the past to conduct time-averaged speed of sound measurements in free jet experiments. On the basis of this existing system, a new setup was developed. This includes a continuous laser system to achieve time-resolved, single-shot measurements. Furthermore, the setup was extended for velocity measurements. In combination with the speed of sound, this results in a direct measurement of the flow Mach number. The required modifications had implications on the available output power of the laser system used here, and, hence, the signal intensity and lifetime. This was successfully compensated by a rigorous alignment and timing of the incoming beams to achieve effective grating formation. Furthermore, controlled beam manipulation allowed measurements in confined test channels, which further distinguishes the present setup from previous work and was the third objective pursued for the technical development.

Prior to its application, the new setup was validated. Three reference cases were investigated, in which the thermodynamic standard data base, numerical predictions and a second, established measurement technique served as validation reference for the LITA measurements. Three objectives were pursued: Firstly, it was demonstrated that very accurate speed of sound measurements are possible with LITA. For well-defined thermodynamic conditions, the measurement uncertainty with respect to the standard data base was within 0.1%.

Secondly, LITA velocimetry was verified for sub- and supersonic ducted flows. Measurements were obtained for a Mach number range from 0.25 to 1.2. Flow velocity and temperature were measured simultaneously and compared to a numerical simulation of the flow field. Both measured quantities yield good agreement with the predicted values within the uncertainty of measurement and prediction. Two separate post-processing approaches were used. For the frequency analysis, the flow quantities are derived from dominant frequencies in the signals. The second approach uses an analytical expression to describe the recorded LITA signal in time and intensity. Both approaches yielded comparable results. The frequency analysis allows a fast and robust interpretation of the LITA signals. The theoretical model has the potential to include more flow quantities in the measurement.

Thirdly, a comprehensive study of large-scale, supersonic free jets was presented to compare LITA to conventional, intrusive probe measurements. Three different inlet total temperatures were evaluated, ranging from 300 K to 1100 K. Reference data were obtained via pitot and total temperature probes. This included the development and manufacturing of new, high-temperature resistant probes required for the hot free jet. Experiments for the second and third cases were conducted at the combustion test facility at ITLR. Here, the harsh environmental conditions negatively affect the LITA measurements. For these experiments, the deviations of LITA from the respective reference range from 0.2 to 2.5 % for Mach number and from 0.1 to 4 % for temperature. Where possible, the performance found was compared to the state of the art published in literature, which showed that either comparable or better results are obtained with the present system.

The validated technique was used in three different applications. The first application was a chemically reacting H_2/air free jet. Time-resolved speed of sound, flow velocity and Mach number measurements are presented for the reaction zone. Speed of sound profiles are shown at three different axial positions downstream of the nozzle exit in comparison to a non-reacting jet with air injection. The evolution of the combustion zone was represented in both the mean and fluctuating parts of the speed of sound. The dimensions of the reaction zone found on basis of these results were consistent with OH^*-chemiluminescence images. LITA velocimetry allowed a clear classification of the experiment as subsonic combustion.

The potential of the LITA setup was also used for the model channels of a scramjet combustor. Here, detailed experimental data sets were obtained from the two injection systems used at ITLR, namely strut and wall injection. This was desirable, as it firstly allowed a thorough validation of an advanced numerical solver developed in a partner project. Secondly, it was possible to resolve the flow field and the shock system resulting from wall injection where the cross jet distorts the supersonic main flow. As the measurement volume was gradually traversed through the shock front, the step change in flow quantities was precisely resolved. Furthermore, measurements were demonstrated in a scramjet combustion chamber at the hot inlet conditions ($T_t \approx 1250\,\mathrm{K}$) of a combustion experiment. However, practical limitations, which at the time being could not be resolved, restricted a full investigation of the resulting flow field.

For the last application, LITA was applied to a shock tube facility. Temperatures and flow Mach numbers behind the incident and reflected shock wave were obtained. In total, the experimental conditions included pressures between 0.1 and 4.3 MPa and temperatures between 420 and 1000 K. The thorough assessment evidently proved the applicability of LITA for shock-heated flows. Furthermore, it allowed to investigate the dependency of the LITA signal intensity on temperature and pressure. As a result, the relationship derived witin the current work allows to extrapolate the performance of the LITA system for the expected conditions in future experiments.

Future prospects may include a closer investigation of the reacting free jet to provide data sets for more axial positions. In addition, the practical implications for the combustion chamber should be addressed. Data sets as obtained for the reacting free jet would then be possible for the scramjet combustor as well. The direct measurement of the flow Mach number in the combustion zone would verify whether supersonic combustion is present in the experiments.

The LITA setup might be further extended. In the author's opinion, quantitative pressure measurements are the most promising aspect. Another suggestion would be to focus on the interpretation of the signal decay rates to obtain the transport properties of the test gas. Furthermore, the spectroscopic features of LITA might be pursued to include absolute concentration measurements of the individual species. This is an important aspect regarding the speed of sound to temperature conversion.

LITA is a promising diagnostic tool that can contribute to many applications in aerospace flows. Giving a concrete example involves the very last experiments conducted, but not documented here. There, LITA was successfully used to probe a heated, high pressure n-hexane jet, which was injected into an inert atmosphere using a common rail diesel injection system. These first results represent a well-founded motivation to pursue LITA for trans- and supercritical fluid injection studies.

Bibliography

[1] Akhmanov, S. and Nikitin, S. *Physical Optics*. Oxford University Press, 1997.

[2] Allen, M. G. 'Diode Laser Absorption Sensors for Gas-dynamic and Combustion Flows'. In: *Meas. Sci. Technol.* 9.4 (Apr. 1998), pp. 545–562. ISSN: 1361-6501. DOI: `10.1088/0957-0233/9/4/001`.

[3] Anderson, J. *Modern Compressible Flow with historical Perspective*. McGraw-Hill, 2004.

[4] Baab, S., Lamanna, G., and Weigand, B. 'Combined Elastic Light Scattering and Two-Scale Shadowgraphy of Near-Critical Fuel Jets'. In: *26th ILASS Americas in Portland, OR, USA, 2014*. 2014.

[5] Baer, D. S. et al. 'Scanned- and Fixed-Wavelength Absorption Diagnostics for Combustion Measurements using Multiplexed Diode Lasers'. In: *AIAA Journal* 34.3 (Mar. 1996), pp. 489–493. ISSN: 1533-385X. DOI: `10.2514/3.13094`.

[6] Balla, R. J. and Miller, C. A. *Signal Analysis Algorithms for Optimized Fitting of Nonresonant Laser Induced Thermal Acoustics Damped Sinusoids*. Tech. rep. Nasa TR-2008-215327, 2008.

[7] Baurle, R. 'Modeling of High Speed Reacting Flows: Established Practices and Future Challenges'. In: *42nd AIAA Aerospace Sciences Meeting and Exhibit*. 2004.

[8] Bivolaru, D. et al. 'Simultaneous CARS and Interferometric Rayleigh Scattering'. In: *25th AIAA Aerodynamic Measurement Technology and Ground Testing Conference* (June 2006). DOI: `10.2514/6.2006-2968`.

[9] Boyce, R. et al. 'SCRAMSPACE: Scramjet-based Access-to-Space Systems'. In: *17th AIAA International Space Planes and Hypersonic Systems and Technologies Conference* (Apr. 2011). DOI: `10.2514/6.2011-2297`.

[10] Boyd, R. W. *Nonlinear Optics*. Boston: Academic Press, 1992, XIII, 439 S. ISBN: 0-12-121680-2.

[11] Brieschenk, S., O'Byrne, S., and Kleine, H. 'Laser-Induced Plasma Ignition Studies in a Model Scramjet Engine'. In: *Combust. Flame* 160.1 (Jan. 2013), pp. 145–148. ISSN: 0010-2180. DOI: `10.1016/j.combustflame.2012.08.011`.

[12] Brown, M. S. et al. 'Analysis of Transient-Grating Signals for Reacting-Flow Applications'. In: *Appl. Opt.* 42.3 (Jan. 2003), p. 566. ISSN: 1539-4522. DOI: `10.1364/ao.42.000566`.

[13] Bühler, M. N. et al. 'Design of a Focusing Schlieren Setup for Use in a Supersonic Combustion Chamber'. In: *30th International Symposium on Shock Waves.* Tel Aviv, Israel, 2015.

[14] Cheng, T. S., Wehrmeyer, J. A., and Pitz, R. W. *Laser Raman Diagnostics in Subsonic and Supersonic Turbulent Jet Diffusion Flames.* Tech. rep. NASA-TM-189544, 1991.

[15] Cheng, T. S. et al. 'Raman Measurement of Mixing and Finite-rate Chemistry in a Supersonic Hydrogen-air Diffusion Flame'. In: *Combust. Flame* 99.1 (Oct. 1994), pp. 157–173. ISSN: 0010-2180. DOI: `10.1016/0010-2180(94)90087-6`.

[16] Cohen, L. S. and Guile, R. N. *Investigation of the Mixing and Combustion of Turbulent, Compressible Free Jets.* NASA CR-1473. 1969.

[17] Cummings, E. B. *Techniques of Single-shot Thermometry by Degenerate Four-Wave Mixing.* Tech. rep. GALCIT FM 92-2, 1992.

[18] Cummings, E. B. 'Laser-Induced Thermal Acoustics: Simple Accurate Gas Measurements'. In: *Opt. Lett.* 19 (1994), pp. 1361–1363. DOI: `10.1364/OL.19.001361`.

[19] Cummings, E. B. 'Laser-Induced Thermal Acoustics'. PhD thesis. California Institut of Technology, 1995.

[20] Cummings, E. B., Leyva, I. A., and Hornung, H. G. 'Laser-Induced Thermal Acoustics (LITA) Signals from Finite Beams'. In: *Appl. Opt.* 34 (1995), pp. 3290–3302. DOI: `10.1364/AO.34.003290`.

[21] Cummings, E. B. et al. 'Measurement of Gas-phase Sound Speed and Thermal Diffusivity over a Broad Pressure Range using Laser-Induced Thermal Acoustics'. In: *Opt. Lett.* 20.14 (July 1995), p. 1577. ISSN: 1539-4794. DOI: `10.1364/ol.20.001577`.

[22] Curran, E. T. ‘Scramjet Engines: The First Forty Years’. In: *J. Propul. Power* 17.6 (Nov. 2001), pp. 1138–1148. ISSN: 1533-3876. DOI: `10.2514/2.5875`.

[23] Curran, E. T. and Murthy, S. N. B. ‘High-Speed Flight Propulsion Systems’. In: *Progress in Astronautics and Aeronautics* (Jan. 1991). DOI: `10.2514/4.866104`.

[24] Cutler, A. D. and Magnotti, G. ‘CARS Spectral Fitting with Multiple Resonant Species using Sparse Libraries’. In: *J. Raman Spectrosc.* 42.11 (Apr. 2011), pp. 1949–1957. ISSN: 0377-0486. DOI: `10.1002/jrs.2948`.

[25] Cutler, A. D. and White, J. ‘An Experimental and CFD Study of a Supersonic Coaxial Jet’. In: *39th Aerospace Sciences Meeting and Exhibit* (Jan. 2001). DOI: `10.2514/6.2001-143`.

[26] Cutler, A. D. et al. ‘Supersonic Coaxial Jet Experiment for CFD Code Validation’. In: *30th Fluid Dynamics Conference* (June 1999). DOI: `10.2514/6.1999-3588`.

[27] Cutler, A. D. et al. ‘Supersonic Coaxial Jet Experiment for Computational Fluid Dynamics Code Validation’. In: *AIAA Journal* 44.3 (Mar. 2006), pp. 585–592. ISSN: 1533-385X. DOI: `10.2514/1.5781`.

[28] Cutler, A. D. et al. ‘Development of Supersonic Combustion Experiments for CFD Modeling’. In: *45th AIAA Aerospace Sciences Meeting and Exhibit* (Jan. 2007). DOI: `10.2514/6.2007-978`.

[29] Cutler, A. D. et al. *Supersonic Combustion Jet Experiments for Code Development and Validation.* 55th JANNAF Propulsion Meeting. 2008.

[30] Cutler, A. D. et al. ‘Dual-Pump CARS Measurements in the University of Virginia’s Dual-Mode Scramjet: Configuration A’. In: *50th AIAA Aerospace Sciences Meeting and Exhibit* (2012).

[31] Cutler, A. D. et al. ‘Dual-Pump CARS Measurements in the University of Virginia’s Dual-Mode Scramjet: Configuration C’. In: *51st AIAA Aerospace Sciences Meeting including the New Horizons Forum and Aerospace Exposition* (Jan. 2013). DOI: `10.2514/6.2013-335`.

[32] Dancey, C. ‘The Turbulent Flow Field Downstream of an Axisymmetric Mach 2 Supersonic Burner - LDA Measurements’. In: *32nd Joint Propulsion Conference and Exhibit* (July 1996). DOI: `10.2514/6.1996-3073`.

[33] Danehy, P. M. ‘Population- and Thermal-Grating Contributions to Degenerate Four-Wave Mixing’. PhD thesis. Stanford University, 1995.

[34] Danehy, P. M. et al. ‘The Effects of Collisional Quenching on Degenerate Four-Wave Mixing’. In: *Appl. Phys. B* 57.4 (Oct. 1993), pp. 243–248. ISSN: 1432-0649. DOI: `10.1007/bf00325202`.

[35] Danehy, P. M. et al. *Simultaneous Temperature and Velocity Measurements in a Large-Scale, Supersonic, Heated Jet.* 55th JANNAF Propulsion Meeting. Newton, MA, 2006.

[36] Danehy, P. M. et al. *Spectroscopic Measurement Techniques for Aerospace Flows.* Tech. rep. NF1676L-18752, 2014.

[37] Demtröder, W. *Laserspektroskopie: Grundlagen & Techniken.* Springer Verlag, 2007.

[38] Dessornes, O. and Scherrer, D. ‘Tests of the JAPHAR Dual Mode Ramjet Engine’. In: *Aerosp. Sci. Technol* 9 (3 2005), pp. 211–221. DOI: `10.1016/j.ast.2005.01.007`.

[39] Dreizler, A., Dreier, T., and Wolfrum, J. ‘Thermal Grating Effects in Infrared Degenerate Four-Wave Mixing for Trace Gas Detection’. In: *Chem. Phys. Lett.* 233.5-6 (Feb. 1995), pp. 525–532. ISSN: 0009-2614. DOI: `10.1016/0009-2614(94)01486-f`.

[40] Dröske, N. C. ‘Investigation of Heat Transfer inside a Scramjet Combustion Chamber’. PhD thesis. Institute of Aerospace Thermodynamics, University of Stuttgart, 2016 (submitted).

[41] Eckbreth, A. C. *Laser Diagnostics for Combustion Temperature and Species.* Tunbridge Wells: Abacus Pr., 1988, XXIV, 414 S. ISBN: 0-85626-344-3.

[42] Eggers, T., Novelli, P., and Haupt, M. ‘Design Studies of the JAPHAR Experimental Vehicle for Dual Mode Ramjet Demonstration’. In: *10th AIAA/NAL-NASDA-ISAS International Space Planes and Hypersonic Systems and Technologies Conference* (Apr. 2001). DOI: `10.2514/6.2001-1921`.

[43] Eichler, H.-J., Günter, P., and Pohl, D. W. *Laser-Induced Dynamic Gratings.* Berlin: Springer, 1986, XI, 256 S. ISBN: 3-540-15875-8.

[44] Einecke, S., Schulz, C., and Sick, V. ‘Measurement of Temperature, Fuel Concentration and Equivalence Ratio Fields using Tracer LIF in IC Engine combustion’. In: *Appl. Phys. B* 71.5 (Nov. 2000), pp. 717–723. ISSN: 1432-0649. DOI: `10.1007/s003400000383`.

[45] Evans, J. S., Schexnayder Jr, C. J., and Beach Jr, H. L. *Application of a two-dimensional Parabolic Computer Program to Prediction of Turbulent Reacting Flows.* Tech. rep. NASA TM-1169, 1978, p. 20463.

[46] Fond, B. et al. 'Simultaneous Temperature, Mixture Fraction and Velocity Imaging in Turbulent Flows using Thermographic Phosphor Tracer Particles'. In: *Opt. Express* 20.20 (Sept. 2012), p. 22118. ISSN: 1094-4087. DOI: `10.1364/oe.20.022118`.

[47] Förster, F. J. and Weigand, B. 'Characterization of a Heterodyne LITA Setup for Simultaneous Flow Velocity and Speed of Sound Measurements'. In: *19th AIAA International Space Planes and Hypersonic Systems and Technologies Conference* (June 2014). DOI: `10.2514/6.2014-2506`.

[48] Förster, F. J. et al. 'Laser-Induced Thermal Acoustics (LITA) Measurements in a Scramjet Combustion Chamber: A Research Plan'. In: *Proceedings of 21th ISABE Conference.* 2013.

[49] Förster, F. J. et al. 'Design and Validation of an Uncooled Pitot Probe for Hot, Supersonic Flow Investigations'. In: *30th International Symposium on Shock Waves.* 2015.

[50] Förster, F. J. et al. 'Temperature and Velocity Determination of Shock-Heated Flows with Non-resonant Heterodyne Laser-Induced Thermal Acoustics'. In: *Appl. Phys. B* 121.3 (Sept. 2015), pp. 235–248. ISSN: 1432-0649. DOI: `10.1007/s00340-015-6217-7`.

[51] Förster, F. J. et al. 'Analysis of Flame Characteristics in a Scramjet Combustor with Staged Fuel Injection Using Common Path Focusing Schlieren and Flame Visualization'. In: *Combust. Flame* (2016 (*accepted paper*)).

[52] Fowler, R. and Guggenheim, E.A. *Statistical Thermodynamics.* Cambridge University Press, 1960.

[53] Freeman, J. et al. *The NASA Hyper-X Program.* Tech. rep. 1997.

[54] Fry, R. S. 'A Century of Ramjet Propulsion Technology Evolution'. In: *J. Propul. Power* 20.1 (Jan. 2004), pp. 27–58. ISSN: 1533-3876. DOI: `10.2514/1.9178`.

[55] Gaffney, R. and Cutler, A. D. 'CFD Modeling Needs and What Makes a Good Supersonic Combustion Validation Experiment'. In: *JANNAF 40th Combustion Meeting.* 2005.

[56] Gaisbauer, U. and Weigand, B. ‘Research Training Group GRK 1095/2: Aero-Thermodynamic Design of a Scramjet Propulsion System’. In: *Proceedings of 20th ISABE Conference*. 2011.

[57] Gerlinger, P. ‘Investigation of an Assumed PDF Approach for Finite-rate Chemistry’. In: *40th AIAA Aerospace Sciences Meeting Exhibit* (Jan. 2002). DOI: `10.2514/6.2002-166`.

[58] Gerlinger, P., Nold, K., and Aigner, M. ‘Influence of Reaction Mechanisms, Grid Spacing, and Inflow Conditions on the Numerical Simulation of Lifted Supersonic Flames’. In: *Int. J. Numer. Meth. Fluids* (2009). ISSN: 1097-0363. DOI: `10.1002/fld.2076`.

[59] Gerlinger, P., Schneider, F., and Aigner, M. ‘Numerical Investigation of Mixing Enhancement by Streamwise Vorticity in Supersonic Combustors’. In: *17th International Symposium on Air Breathing Engines*. Munich, Germany, 2005. ISABE 2005-1019.

[60] Govoni, D. E. et al. ‘The Non-resonant Signal in Laser-Induced Grating Spectroscopy of Gases’. In: *Chem Phys Lett* 216.3 (1993), pp. 525–529.

[61] Goyne, C. P. et al. ‘Test Gas Vitiation Effects in a Dual-Mode Scramjet Combustor’. In: *J. Propul. Power* 23.3 (2007), pp. 559–565. DOI: `10.2514/1.24663`.

[62] Goyne, C., Cresci, D., and Fetterhoff, T. ‘Short Duration Propulsion Test and Evaluation (Hy-V) Program’. In: *16th AIAA/DLR/DGLR International Space Planes and Hypersonic Systems and Technologies Conference* (Oct. 2009). DOI: `10.2514/6.2009-7296`.

[63] Goyne, C. et al. ‘Velocity Measurement in a Dual-mode Supersonic Combustor using Particle Image Velocimetry’. In: *10th AIAA/NAL NASDA ISAS International Space Planes and Hypersonic Systems and Technologies Conference* (Apr. 2001). DOI: `10.2514/6.2001-1761`.

[64] Grant, I. ‘Particle image velocimetry: A review’. In: *Proceedings of the Institution of Mechanical Engineers, Part C: Journal of Mechanical Engineering Science* 211.1 (Jan. 1997), pp. 55–76. ISSN: 2041-2983. DOI: `10.1243/0954406971521665`.

[65] Günther, R. *Verbrennung und Feuerungen*. Springer Verlag, 1974.

[66] Gurland, J. and Tripathi, R. C. ‘A simple Approximation for Unbiased Estimation of the Standard Deviation’. In: *Am. Stat.* 25.4 (1971), pp. 30–32.

[67] Hallion, R. P. *The Hypersonic Revolution, Volume I: From Max Valier to Project Prime*. Tech. rep. ASC-TR-95-5010, 1995.

[68] Hancock, R. D. et al. 'Dual-pump Coherent Anti-Stokes Raman Scattering Measurements of Nitrogen and Oxygen in a Laminar Jet Diffusion Flame'. In: *Appl. Opt.* 36.15 (May 1997), p. 3217. ISSN: 1539-4522. DOI: `10.1364/ao.36.003217`.

[69] Hanson, R. K. and Davidson, D. F. 'Recent Advances in Laser Absorption and Shock Tube Methods for Studies of Combustion Chemistry'. In: *Prog. Energ. Combust.* 44 (2014), pp. 103–114. DOI: `10.1016/j.pecs.2014.05.001`.

[70] Hanson, R. K. and Jeffries, J. B. 'Advances in Laser-based Sensors for Combustion Systems'. In: *6th Symposium on Smart Control of Turbulence*. 2005.

[71] Hanson, R. K., Seitzman, J.M., and Paul, P.H. 'Planar Laser-Fluorescence Imaging of Combustion Gases'. In: *Appl. Phys. B* 50.6 (June 1990), pp. 441–454. ISSN: 1432-0649. DOI: `10.1007/bf00408770`.

[72] Hart, R. C., Balla, R. J., and Herring, G. C. 'Observation of H_20 in a Flame by Two-colour Laser-Induced-Grating Spectroscopy'. In: *Meas. Sci. Technol.* 8.8 (Aug. 1997), pp. 917–920. ISSN: 1361-6501. DOI: `10.1088/0957-0233/8/8/013`.

[73] Hart, R. C., Balla, R. J., and Herring, G. C. 'Optical Measurement of the Speed of Sound in Air over the Temperature Range 300-650 K'. In: *The Journal of the Acoustical Society of America* 108.4 (Oct. 2000), pp. 1946–1948. ISSN: 0001-4966. DOI: `10.1121/1.1289671`.

[74] Hart, R. C., Balla, R. J., and Herring, G. C. 'Simultaneous Velocimetry and Thermometry of Air by use of Non-resonant Heterodyned Laser-Induced Thermal Acoustics'. In: *Appl Opt* 40.6 (Feb. 2001), p. 965. ISSN: 1539-4522. DOI: `10.1364/ao.40.000965`.

[75] Hart, R. C., Herring, G. C., and Balla, R. J. 'Common-path Heterodyne Laser-Induced Thermal Acoustics for Seedless Laser Velocimetry'. In: *Opt. Lett.* 27.9 (May 2002), p. 710. ISSN: 1539-4794. DOI: `10.1364/ol.27.000710`.

[76] Hart, R. C., Herring, G. C., and Balla, R. J. 'Pressure Measurement in Supersonic Air Flow by Differential Absorptive Laser-Induced Thermal Acoustics'. In: *Opt. Lett.* 32.12 (June 2007), p. 1689. ISSN: 1539-4794. DOI: `10.1364/ol.32.001689`.

[77] Hell, A. 'Validierung der Lasermesstechnik Laser-induzierte Thermische Akustik für die Anwendung in turbulenten, chemisch reagierenden Überschallfreistrahlen'. PhD thesis. Institute of Aerospace Thermodynamics, University of Stuttgart, 2012.

[78] Hell, A., Förster, F. J., and Weigand, B. 'Validation of Laser-Induced Thermal Acoustics for Chemically Reacting H_2/air Free Jets'. In: *J. Raman Spectrosc.* (2016). ISSN: 0377-0486. DOI: `10.1002/jrs.4859`.

[79] Hemmerling, B., Kozlov, D. N., and Stampanoni-Panariello, A. 'Temperature and Flow Velocity Measurements by use of Laser-Induced Electrostrictive Gratings'. In: *Opt. Lett.* 25.18 (Sept. 2000), p. 1340. ISSN: 1539-4794. DOI: `10.1364/ol.25.001340`.

[80] Hemmerling, B. et al. 'Rocket Nozzle Cold-gas Flow Velocity Measurements using Laser-Induced Gratings'. In: *J. Raman Spectrosc.* 33.11-12 (2002), pp. 912–918. ISSN: 1097-4555. DOI: `10.1002/jrs.946`.

[81] Hemmerling, B. et al. 'Diagnostics of Water-containing Gas Mixtures using Thermal Laser-Induced Gratings'. In: *Chem. Phys.* 320.2-3 (Jan. 2006), pp. 103–117. ISSN: 0301-0104. DOI: `10.1016/j.chemphys.2005.06.048`.

[82] Herring, G. C. 'Mach-Number Measurement with Laser and Pressure Probes in Humid Supersonic Flow'. In: *AIAA Journal* 46.8 (Aug. 2008), pp. 2107–2109. ISSN: 1533-385X. DOI: `10.2514/1.36107`.

[83] Herring, G. C. *Temperature and Pressure Dependency of Signal Amplitudes for Electrostriction Laser-Induced Thermal Acoustics.* Tech. rep. Nasa TR-2015-218762, 2015.

[84] Herring, G. C., Meyers, J. F., and Hart, R. C. 'Shock-strength Determination with Seeded and Seedless Laser Methods'. In: *Meas. Sci. Technol.* 20.4 (Feb. 2009). ISSN: 1361-6501. DOI: `10.1088/0957-0233/20/4/045304`.

[85] Herring, G. C. et al. *Prospects for Nonlinear Laser Diagnostics in the Jet Noise Laboratory.* Tech. rep. NASA/TM-2007-214893, 2007.

[86] Hiller, B. and Hanson, R. K. 'Simultaneous Planar Measurements of Velocity and Pressure Fields in Gas Flows using Laser-Induced Fluorescence'. In: *Appl. Opt.* 27.1 (Jan. 1988), p. 33. ISSN: 1539-4522. DOI: `10.1364/ao.27.000033`.

[87] Högenauer, E. and Koelle, D. 'Sänger - The German Aerospace Vehicle Program'. In: *National Aerospace Plane Conference* (July 1989). DOI: `10.2514/6.1989-5007`.

[88] Hooker, S. *Not much of an engineer*. Crowood, 1985.

[89] Hornung, H. G. et al. 'Recent Results from Hypervelocity Research in T5'. In: *18th AIAA Aerospace Ground Testing Conference* (1994). DOI: `10.2514/6.1994-2523`.

[90] Hruschka, R., O'Byrne, S., and Kleine, H. 'Comparison of Velocity and Temperature Measurements with Simulations in a Hypersonic Wake Flow'. In: *Exp. Fluids* 51 (2011), pp. 407–421. DOI: `10.1007/s00348-011-1039-9`.

[91] Itoh, K. et al. 'Hypersonic Aerothermodynamic and Scramjet Research using High Enthalpy Shock Tunnel'. In: *Shock Waves* 12 (2002), pp. 93–98. DOI: `10.1007/s00193-002-0147-0`.

[92] Jackson, K., Gruber, M., and Barhorst, T. 'The HIFiRE Flight 2 Experiment: An Overview and Status Update'. In: *45th AIAA/ASME/-SAE/ASEE Joint Propulsion Conference Exhibit* (Aug. 2009). DOI: `10.2514/6.2009-5029`.

[93] Jenkins, L. N. et al. 'Application of Laser-Induced Thermal Acoustics to a High-lift Configuration'. In: *Optical Diagnostics for Fluids, Solids, and Combustion II* (Nov. 2003). Ed. by Farrell, Patrick V. et al. DOI: `10.1117/12.507732`.

[94] Jourdren, C. and Dessornes, O. 'One Strut Scramjet Chamber Studies in the Frame of the PREPHA Program'. In: *8th AIAA International Space Planes and Hypersonic Systems and Technologies Conference* (Apr. 1998). DOI: `10.2514/6.1998-1560`.

[95] Kasal, P. 'Räumlich hochauflösende Flammendiagnostik mit Hilfe der Spontanen Ramanspektroskopie'. PhD thesis. Institute of Aerospace Thermodynamics, University of Stuttgart, 1988.

[96] Kasal, P. and Algermissen, J. *SFB85/B3: Experimentelle und theoretische Untersuchungen zur stossinduzierten Verbrennung von Wasserstoff im Überschall-Luftstrom*. Tech. rep. 1983.

[97] Kasal, P. and Algermissen, J. 'Raman-spektroskoptische Temperaturmessungen in schrägstossinduzierten Wasserstoff/Luft-Überschallflammen'. In: *Z. Flugwiss. Weltraumforsch.* (1989).

[98] Kasal, P. et al. 'Supersonic Combustion: Fundamental Investigations of Aerothermodynamic Key Problems'. In: *11th AIAA/AAAF International Conference*. Orleans, France, 2002.

[99] Kiefer, J. and Ewart, P. 'Laser Diagnostics and Minor Species Detection in Combustion using Resonant Four-Wave Mixing'. In: *Progress in Energy and Combustion Science* 37.5 (2011), pp. 525–564. ISSN: 0360-1285. DOI: `10.1016/j.pecs.2010.11.001`.

[100] Kiefer, J. et al. 'Local Fuel Concentration Measurements for Mixture Formation Diagnostics using Diffraction by Laser-Induced Gratings in Comparison to Spontaneous Raman Scattering'. In: *J. Raman Spectrosc.* 39.6 (2008), pp. 711–721. ISSN: 1097-4555. DOI: `10.1002/jrs.1965`.

[101] Kleine, H. et al. 'Bifurcation of a Reflected Shock Wave in a Shock Tube'. In: *Shock Waves* (1992).

[102] Koelle, D. E. 'Launch Cost Analyses for Reusable Space Transportation Systems (Sänger II)'. In: *Acta Astron.* 19.2 (Feb. 1989), pp. 191–197. ISSN: 0094-5765. DOI: `10.1016/0094-5765(89)90101-x`.

[103] Kouchi, T. et al. 'Focusing-schlieren Visualization in a Dual-mode Scramjet'. In: *Exp. Fluids* 56.12 (Nov. 2015). ISSN: 1432-1114. DOI: `10.1007/s00348-015-2081-9`.

[104] Kozlov, D. N. 'Simultaneous Characterization of Flow Velocity and Temperature Fields in a Gas Jet by Use of Electrostrictive Laser-Induced Gratings'. In: *Appl. Phys. B* 80 (2005), pp. 377–387.

[105] Kozlov, D. N., Hemmerling, B., and Stampanoni-Panariello, A. 'Measurement of Gas Jet Flow Velocities using Laser-Induced Electrostrictive Gratings'. In: *Appl. Phys. B* 71.4 (Oct. 2000), pp. 585–591. ISSN: 1432-0649. DOI: `10.1007/s003400000377`.

[106] Lackner, M. et al. 'Demonstration of Methane Spectroscopy using a Vertical-Cavity Surface-Emitting Laser at 1.68 μm with up to 5 MHz Repetition Rate'. In: *Meas. Sci. Technol.* 14.1 (Dec. 2002), pp. 101–106. ISSN: 0957-0233. DOI: `10.1088/0957-0233/14/1/315`.

[107] Lagen, N. and Seiner, J. M. 'Evaluation of Water Cooled Supersonic Temperature and Pressure Probes for Application to 1366 K Flows'. In: *36th International Instrumentation Symposium*. 1990, pp. 349–365.

[108] Legge, H. and Dettleff, G. 'Pitot Pressure and Heat-Transfer Measurements in Hydrazine Thruster Plumes'. In: *J. Spacecraft* (1986). DOI: `10.2514/3.25812`.

[109] Lemmon, E., Huber, M., and McLinden, M. 'NIST Standard Reference Database 23: Reference Fluid Thermodynamic and Transport Properties-REFPROP, Version 9.1'. In: (2013).

[110] Lempert, W. R. and Adamovich, I. V. 'Coherent Anti-Stokes Raman Scattering and Spontaneous Raman Scattering Diagnostics of Nonequilibrium Plasmas and Flows'. In: *J. Phys. D: Appl. Phys.* 47.43 (Oct. 2014), p. 433001. ISSN: 1361-6463. DOI: `10.1088/0022-3727/47/43/433001`.

[111] Lengelle, G. and Verdier, C. *Gas Sampling and Analysis in Combustion Phenomena*. AGARD-AG-168. 1973.

[112] Li, H., Wehe, S. D., and McManus, K. R. 'Real-time Equivalence Ratio Measurements in Gas Turbine Combustors with a Near-infrared Diode Laser Sensor'. In: *Proceedings of the Combustion Institute* 33.1 (2011), pp. 717–724. ISSN: 1540-7489. DOI: `10.1016/j.proci.2010.05.114`.

[113] Li, H. et al. 'Near-infrared Diode Laser Absorption Sensor for Rapid Measurements of Temperature and Water Vapor in a Shock Tube'. In: *Appl. Phys. B* 89.2-3 (Sept. 2007), pp. 407–416. ISSN: 1432-0649. DOI: `10.1007/s00340-007-2781-9`.

[114] Li, Y., Roberts, W., and Brown, M. 'Investigation of Gaseous Acoustic Damping Rates by Transient Grating Spectroscopy'. In: *AIAA Journal* 40.6 (June 2002), pp. 1071–1077. ISSN: 1533-385X. DOI: `10.2514/2.1790`.

[115] Liu, J.T.C. et al. 'Near-infrared Diode Laser Absorption Diagnostic for Temperature and Water Vapor in a Scramjet Combustor'. In: *Appl. Opt.* 44.31 (Nov. 2005), p. 6701. ISSN: 1539-4522. DOI: `10.1364/ao.44.006701`.

[116] Lorin, R. 'Le Propulseur à échappement et l'Aéroplane à Grande Vitesse'. In: *L'Aérophile* (1908), pp. 332–336.

[117] MacKinnon, H. et al. 'Advances in Aerodynamic Probes for High-Enthalpy Applications'. In: *24th AIAA Aerodynamic Measurement Technology and Ground Testing Conference* (June 2004). DOI: `10.2514/6.2004-2594`.

[118] Magnotti, G., Cutler, A., and Danehy, P. 'Development of a Dual-Pump CARS System for Measurements in a Supersonic Combusting Free Jet'. In: *50th AIAA Aerospace Sciences Meeting including the New Horizons Forum and Aerospace Exposition* (Jan. 2012). DOI: `10.2514/6.2012-1193`.

[119] Makowka, K. ‘Numerically Efficient Hybrid RANS/LES of Supersonic Combustion’. PhD thesis. Lehrstuhl für Thermodynamik, Technische Universität München, 2015.

[120] McKienzie, R. L. ‘Progress in Laser Spectroscopic Techniques for Aerodynamic Measurements - An Overview’. In: *AIAA Journal* 31.3 (Mar. 1993), pp. 465–477. ISSN: 1533-385X. DOI: `10.2514/3.11353`.

[121] Meier, A. and Schlamp, S. ‘Improved Signal Intensity for Transient Grating Spectroscopy Using a PIV Laser’. In: *25th AIAA Aerodynamic Measurement Technology and Ground Testing Conference* (June 2006). DOI: `10.2514/6.2006-2973`.

[122] Melling, A. ‘Tracer Particles and Seeding for Particle Image Velocimetry’. In: *Meas. Sci. Technol.* 8.12 (Dec. 1997), pp. 1406–1416. ISSN: 1361-6501. DOI: `10.1088/0957-0233/8/12/005`.

[123] Mizukaki, T. and Matsuzawa, T. ‘Application of Laser-Induced Thermal Acoustics in Air to Measurement of Shock-Induced Temperature Changes’. In: *Shock Waves* 19.5 (July 2009), pp. 361–369. ISSN: 1432-2153. DOI: `10.1007/s00193-009-0218-6`.

[124] Möbus, H., Gerlinger, P., and Brüggemann, D. ‘Comparison of Eulerian and Lagrangian Monte Carlo PDF Methods for Turbulent Diffusion Flames’. In: *Combust. Flame* 124.3 (Feb. 2001), pp. 519–534. ISSN: 0010-2180. DOI: `10.1016/s0010-2180(00)00207-8`.

[125] Möbus, H., Gerlinger, P., and Brüggemann, D. ‘Scalar and Joint Scalar-Velocity-Frequency Monte Carlo PDF Simulation of Supersonic Combustion’. In: *Combust. Flame* 132.1-2 (Jan. 2003), pp. 3–24. ISSN: 0010-2180. DOI: `10.1016/s0010-2180(02)00428-5`.

[126] Murakami, E. and Papamoschou, D. ‘Mixing Layer Characteristics of Coaxial Supersonic Jets’. In: *6th Aeroacoustics Conference and Exhibit* (June 2000). DOI: `10.2514/6.2000-2060`.

[127] Neracher, M. and Hubschmid, W. ‘Heterodyne-detected Electrostrictive Laser-Induced Gratings for Gas-flow Diagnostics’. In: *Appl. Phys. B* 79.6 (Sept. 2004), pp. 783–791. ISSN: 1432-0649. DOI: `10.1007/s00340-004-1632-1`.

[128] O’Byrne, S. et al. ‘Dual-Pump Coherent Anti-Stokes Raman Scattering Measurements in a Supersonic Combustor’. In: *AIAA Journal* 45.4 (Apr. 2007), pp. 922–933. ISSN: 1533-385X. DOI: `10.2514/1.26768`.

[129] Oertel, H. *Stossrohre*. Springer Verlag, 1966.

[130] Palmer, R.E. *The CARSFT Computer Code for Calculating Coherent Anti-Stokes Raman Spectra: User and Programmer Information.* Tech. rep. SAND89-8206, 1989.

[131] Paul, P. H. and Farrow, R. L. 'Gas-phase Thermal-Grating Contributions to Four-Wave Mixing'. In: *J. Opt. Soc. Am. B* 12 (1995), pp. 384–392. DOI: `10.1364/JOSAB.12.000384`.

[132] Paul, P. H. et al. 'Collisional Quenching Corrections for Laser-Induced Fluorescence Measurements of NO A2 $\Sigma+$'. In: *AIAA Journal* 32.8 (Aug. 1994), pp. 1670–1675. ISSN: 1533-385X. DOI: `10.2514/3.12158`.

[133] Paull, A. and Stalker, R. 'Scramjet Testing in the T4 Impulse Facility'. In: *8th AIAA International Space Planes and Hypersonic Systems and Technologies Conference* (Apr. 1998). DOI: `10.2514/6.1998-1533`.

[134] Philippe, L. C. and Hanson, R. K. 'Laser Diode Wavelength-Modulation Spectroscopy for Simultaneous Measurement of Temperature, Pressure, and Velocity in Shock-heated Oxygen Flows'. In: *Appl. Opt.* 32.30 (Oct. 1993), p. 6090. ISSN: 1539-4522. DOI: `10.1364/ao.32.006090`.

[135] Porro, A. R. 'Pressure Probe Designs for Dynamic Pressure Measurements in a Supersonic Flow Field'. In: *ICIASF 2001 Record, 19th International Congress on Instrumentation in Aerospace Simulation Facilities* (). DOI: `10.1109/iciasf.2001.960277`.

[136] Roberts, W. T. 'Titanium'. In: *Endeavour* 7.4 (Jan. 1983), pp. 189–193. ISSN: 0160-9327. DOI: `10.1016/s0160-9327(83)80042-8`.

[137] Rolls Royce. *The Jet engine.* John Wiley & Sons, 2015.

[138] Rondeau, M. and Jorris, T. 'X-51A Scramjet Demonstrator Program: Waverider Ground and Flight Test'. In: *44th International / SETP Southwest Flight Test Symposium.* 2013.

[139] Rosenko, E. 'Anwendung elektrostriktiver Gitter auf nichtreaktive, turbulente Hochgeschwindigkeits-Freistrahlen'. PhD thesis. Institute of Aerospace Thermodynamics, University of Stuttgart, 2009.

[140] Roshani, B. et al. 'Simultaneous Measurements of Fuel Vapor Concentration and Temperature in a Flash-boiling Propane Jet using Laser-Induced Gratings'. In: *J. Raman Spectrosc.* 44.10 (May 2013), pp. 1356–1362. ISSN: 0377-0486. DOI: `10.1002/jrs.4315`.

[141] Roy, S., Gord, J. R., and Patnaik, A. K. 'Recent Advances in Coherent Anti-Stokes Raman Scattering Spectroscopy: Fundamental Develop-

ments and Applications in Reacting Flows'. In: *Progress in Energy and Combustion Science* 36.2 (Apr. 2010), pp. 280–306. ISSN: 0360-1285. DOI: `10.1016/j.pecs.2009.11.001`.

[142] Rozouvan, S. and Dreier, T. 'Polarization-dependent Laser-Induced Grating Measurements'. In: *Opt. Lett.* 24.22 (Nov. 1999), p. 1596. ISSN: 1539-4794. DOI: `10.1364/ol.24.001596`.

[143] Saleh, B. E. and Teich, M. C. *Grundlagen der Photonik*. Weinheim: Wiley-VCH, 2008, XXIII, 1406 S. ISBN: 3-527-40677-8.

[144] Sander, T., Altenhöfer, P., and Mundt, C. 'Development of Laser-Induced Grating Spectroscopy for Application in Shock Tunnels'. In: *J. Thermophys. Heat Transfer* 28.1 (Jan. 2014), pp. 27–31. ISSN: 1533-6808. DOI: `10.2514/1.t4131`.

[145] Sander, T., Altenhöfer, P., and Mundt, C. 'Temperature Measurements in a Shock Tube Using Laser-Induced Grating Spectroscopy'. In: *J. Thermophys. Heat Transfer* 30.1 (Jan. 2016), pp. 62–66. ISSN: 1533-6808. DOI: `10.2514/1.t4556`.

[146] Sandvik Group. *Kanthal Appliance Heating Alloy Handbook*. 2011.

[147] Scarano, F. 'Overview of PIV in Supersonic Flows'. In: *Particle Image Velocimetry*. Ed. by Schröder, A. and Willert, C. Springer, 2008, pp. 445–463. DOI: `10.1007/978-3-540-73528-1_24`.

[148] Schlamp, S. 'Laser-Induced Thermal Acoustic Velocimetry'. PhD thesis. California Institut of Technology, 2000.

[149] Schlamp, S., Cummings, E. B., and Hornung, H. G. 'Beam Misalignments and Fluid Velocities in Laser-Induced Thermal Acoustics'. In: *Appl. Opt.* 38.27 (Sept. 1999), p. 5724. ISSN: 1539-4522. DOI: `10.1364/ao.38.005724`.

[150] Schlamp, S., Cummings, E. B., and Sobota, T. 'Laser-Induced Thermal-Acoustic Velocimetry with Heterodyne Detection'. In: *Opt. Lett.* 25.4 (Feb. 2000), p. 224. ISSN: 1539-4794. DOI: `10.1364/ol.25.000224`.

[151] Schlamp, S. and Sobota, T. 'Measuring Concentrations with Laser-Induced Thermalization and Electrostriction Gratings'. In: *Exp. Fluids* 32.6 (Apr. 2002), pp. 683–688. ISSN: 1432-1114. DOI: `10.1007/s00348-002-0419-6`.

[152] Schlamp, S. et al. 'Experimental Considerations for Laser-Induced Thermal Acoustics in Compressible Turbule'. In: *33rd AIAA Fluid*

Dynamics Conference and Exhibit (June 2003). DOI: `10.2514/6.2003-3454`.

[153] Schlamp, S. et al. 'Transient Grating Spectroscopy in a Hot Turbulent Compressible Free Jet'. In: *J. Propul. Power* 21.6 (Nov. 2005), pp. 1008–1018. ISSN: 1533-3876. DOI: `10.2514/1.13794`.

[154] Schultz, I. A. et al. 'Spatially Resolved Water Measurements in a Scramjet Combustor Using Diode Laser Absorption'. In: *J. Propul. Power* 30.6 (Nov. 2014), pp. 1551–1558. ISSN: 1533-3876. DOI: `10.2514/1.b35219`.

[155] Seeger, T. et al. 'Time-resolved Measurement of the Local Equivalence Ratio in a Gaseous Propane Injection Process using Laser-Induced Gratings'. In: *Opt. Express* 14.26 (2006), p. 12994. ISSN: 1094-4087. DOI: `10.1364/oe.14.012994`.

[156] Segal, C. *The Scramjet Engine.* Processes and Characteristics. Cambridge University Press, 2009. ISBN: 978-0521838153.

[157] Smart, M. K., Hass, N. E., and Paull, A. 'Flight Data Analysis of the HyShot 2 Scramjet Flight Experiment'. In: *AIAA Journal* 44.10 (Oct. 2006), pp. 2366–2375. ISSN: 1533-385X. DOI: `10.2514/1.20661`.

[158] Smyth, K. C. and Crosley, D. R. 'Detection of Minor Species with Laser Techniques'. In: *Applied Combustion Diagnostics.* Ed. by Kohse-Hoinghaus, K. and Jeffries, J.B. Taylor and Francis, 2002.

[159] Springer, R. et al. 'Conventional/Laser Diagnostics to Assess Flow Quality in a Combustion-heated Facility'. In: *35th AIAA/ASME/SAW -ASEE Joint Propulsion Conference and Exhibit.* 1999.

[160] Stalker, R. 'A Study of the Free-Piston Shock Tunnel'. In: *AIAA Journal* 5.12 (1967), pp. 2160–2165. DOI: `10.2514/3.4402`.

[161] Stampanoni-Panariello, A., Hemmerling, B., and Hubschmid, W. 'Temperature Measurements in Gases using Laser-Induced Electrostrictive Gratings'. In: *Appl. Phys. B* 67.1 (July 1998), pp. 125–130. ISSN: 1432-0649. DOI: `10.1007/s003400050484`.

[162] Stampanoni-Panariello, A. et al. 'Gas Phase Diagnostics by Laser-Induced Gratings I. Theory'. In: *Appl. Phys. B* 81.1 (June 2005), pp. 101–111. ISSN: 1432-0649. DOI: `10.1007/s00340-005-1852-z`.

[163] Stampanoni-Panariello, A. et al. 'Gas Phase Diagnostics by Laser-Induced Gratings II. Experiments'. In: *Appl. Phys. B* 81.1 (June 2005), pp. 113–129. ISSN: 1432-0649. DOI: `10.1007/s00340-005-1853-y`.

[164] Stevens, R. and Ewart, P. 'Single-shot Measurement of Temperature and Pressure using Laser-Induced Thermal Gratings with a Long Probe Pulse'. In: *Appl. Phys. B* 78.1 (Jan. 2004), pp. 111–117. ISSN: 1432-0649. DOI: `10.1007/s00340-003-1282-8`.

[165] Stotz, I. 'Shock Tube Study on the Disintegration of Fuel Jets at Elevated Pressures and Temperatures'. PhD thesis. Institute of Aerospace Thermodynamics, University of Stuttgart, 2011.

[166] Stotz, I. et al. 'Design of a Double Diaphragm Shock Tube for Fluid Disintegration Studies'. In: *Rev. Sci. Instrum.* 79.12 (2008). ISSN: 0034-6748. DOI: `10.1063/1.3058609`.

[167] Sung, C. J. et al. 'Chemical Kinetics and Self-Ignition in a Model Supersonic Hydrogen-Air Combustor'. In: *AIAA Journal* 37.2 (Feb. 1999), pp. 208–214. ISSN: 1533-385X. DOI: `10.2514/2.715`.

[168] Sur, R. et al. 'Scanned-Wavelength-Modulation-Spectroscopy Sensor for CO, CO_2, CH_4 and H_2O in a High-pressure Engineering-scale Transport-reactor Coal Gasifier'. In: *Fuel* 150 (June 2015), pp. 102–111. ISSN: 0016-2361. DOI: `10.1016/j.fuel.2015.02.003`.

[169] Swan, W. 'On the Prismatic Spectra of the Flames of Compounds of Carbon and Hydrogen'. In: *Transactions of the Royal Society of Edinburgh* 21.03 (Jan. 1857), pp. 411–429. ISSN: 0080-4568. DOI: `10.1017/s0080456800032233`.

[170] Tedder, S. et al. 'CARS Temperature and Species Concentration Measurements in a Supersonic Combustor with Normal Injection'. In: *43rd AIAA Aerospace Sciences Meeting and Exhibit* (Jan. 2005). DOI: `10.2514/6.2005-616`.

[171] Tedder, S. et al. 'Characterization of a Combined CARS and Interferometric Rayleigh Scattering System'. In: *45th AIAA Aerospace Sciences Meeting and Exhibit* (Jan. 2007). DOI: `10.2514/6.2007-871`.

[172] Tedder, S. et al. 'CARS Temperature Measurements in a Combustion-Heated Supersonic Jet'. In: *47th AIAA Aerospace Sciences Meeting including The New Horizons Forum and Aerospace Exposition* (Jan. 2009). DOI: `10.2514/6.2009-524`.

[173] Tedeschi, G., Gouin, H., and Elena, M. 'Motion of Tracer Particles in Supersonic Flows'. In: *Exp. Fluids* 26.4 (Mar. 1999), pp. 288–296. ISSN: 1432-1114. DOI: `10.1007/s003480050291`.

[174] Tegeler, C., Span, R., and Wagner, W. ‘A New Equation of State for Argon Covering the Fluid Region for Temperatures From the Melting Line to 700 K at Pressures up to 1000 MPa’. In: *J. Phys. Chem. Ref. Data* 28.3 (1999), p. 779. ISSN: 0047-2689. DOI: `10.1063/1.556037`.

[175] Teukolsky, S. and Press, W. H. *Numerical Recipes*. 1986.

[176] Thorlabs. *APD210 - High-Speed Si Avalanche Photodetector*. 2008.

[177] Thorlabs. *APD110x Series Avalanche Photodetectors*. 2011.

[178] Tollmien, W. ‘Berechnung turbulenter Ausbreitungsvorgänge’. In: *Ztschr. i. angew. Math. und Mech.* (1926).

[179] Tropea, C., Yarin, A., and Foss, J.F. *Springer Handbook of Experimental Fluid Mechanics*. Springer, 2007.

[180] van Oudheusden, B. W. ‘PIV-based Pressure Measurement’. In: *Meas. Sci. Technol.* 24.3 (Jan. 2013). ISSN: 1361-6501. DOI: `10.1088/0957-0233/24/3/032001`.

[181] Vellaramkalayil, J. J. ‘Experimental and Numerical Investigations of Different Injection Schemes in a Supersonic Combustion Chamber’. PhD thesis. Institute of Aerospace Thermodynamics, University of Stuttgart, 2014.

[182] Voland, R. T., Huebner, L. D., and McClinton, C. R. ‘X-43A Hypersonic vehicle technology development’. In: *Acta Astron.* 59.1-5 (July 2006), pp. 181–191. ISSN: 0094-5765. DOI: `10.1016/j.actaastro.2006.02.021`.

[183] Wagner, S. *SFB259: Hochtemperaturprobleme rückkehrfähiger Raumtransportsysteme*. Tech. rep. DFG, 2001.

[184] Walker, D. J. W., Williams, R. B., and Ewart, P. ‘Thermal Grating Velocimetry’. In: *Opt. Lett.* 23.16 (Aug. 1998), p. 1316. ISSN: 1539-4794. DOI: `10.1364/ol.23.001316`.

[185] Walker, S. and Rodgers, F. ‘The Hypersonic Collaborative Australia/United States Experiment (HyCAUSE)’. In: *AIAA/CIRA 13th International Space Planes and Hypersonics Systems and Technologies Conference* (May 2005). DOI: `10.2514/6.2005-3254`.

[186] Waltrup, P., Anderson, G., and Stull, F. ‘Supersonic Combustion Ramjet (SCRAMJET) Engine Development in the United States’. In: *3rd International Symposium on Air Breathing Engines*. 1976.

[187] Webber, M. E. et al. ‘In situ Combustion Measurements of CO, CO_2, H_2O and Temperature using Diode Laser Absorption Sensors’. In: *Pro-*

ceedings of the Combustion Institute 28.1 (Jan. 2000), pp. 407–413. ISSN: 1540-7489. DOI: `10.1016/s0082-0784(00)80237-4`.

[188] Weigand, B. and Gaisbauer, U. 'An Overview on the Structure and Work of the DFG Research Training Group GRK 1095: Aero-Thermo-dynamic Design of a Scramjet Propulsion System'. In: *16th AIAA/DLR/DGLR International Space Planes and Hypersonic Systems and Technologies Conference* (Oct. 2009). DOI: `10.2514/6.2009-7276`.

[189] Weigand, B., Köhler, J., and von Wolfersdorf, J. *Thermodynamik kompakt.* Springer, 2013. ISBN: 978-3-642-37232-2.

[190] Williams, B. et al. 'High precision In-cylinder Gas Thermometry using Laser Induced Gratings: Quantitative Measurement of Evaporative Cooling with Gasoline/Alcohol Blends in a GDI Optical Engine'. In: *Combust. Flame* 161.1 (Jan. 2014), pp. 270–279. ISSN: 0010-2180. DOI: `10.1016/j.combustflame.2013.07.018`.

[191] Williams, S. et al. 'Laser-Induced Thermal Grating Effects in Flames'. In: *Opt. Lett.* 19.21 (Nov. 1994), p. 1681. ISSN: 1539-4794. DOI: `10.1364/ol.19.001681`.

[192] Witzel, O. et al. 'VCSEL-based, High-speed, in situ TDLAS for In-cylinder Water Vapor Measurements in IC Engines'. In: *Opt. Express* 21.17 (Aug. 2013), p. 19951. ISSN: 1094-4087. DOI: `10.1364/oe.21.019951`.

[193] Wohler, A. 'Mischungsuntersuchungen in einer beschleunigten kompressiblen Düsenströmung unter Verwendung verschiedener Injektorgeometrien'. PhD thesis. Institute of Aerospace Thermodynamics, University of Stuttgart, 2014.

[194] Wohler, A. et al. 'Mixing Processes in a Compressible Accelerated Nozzle Flow with Blunt-Body Wakes'. In: *AIAA Journal* 52.3 (Mar. 2014), pp. 559–568. ISSN: 1533-385X. DOI: `10.2514/1.j052493`.

[195] Yoo, J. et al. 'Planar Laser-Induced Fluorescence Imaging in Shock Tube Flows'. In: *Exp. Fluids* 49 (2010), pp. 751–759. DOI: `10.1007/s00348-010-0876-2`.

APPENDIX A

Intrusive Measurement Techniques

A.1 Pitot and Total Temperature Probes

Commercial Probes

The commercial pitot and total temperature probes are provided by DLR and shown in figure A.1. They are manufactured from stainless steel. The absence of a cooling system restricts the operation to moderately heated flows of 500 K to 600 K in total temperature. Both probe heads are 5 mm in diameter. For the pitot probe, the sensing opening is 0.5 mm in diameter with a pipe connecting the probe head to the piezoelectric pressure transducer. For the total temperature probe, the head is designed to isentropically decelerate the flow to zero velocity. A type K thermocouple is integrated into the probe head to measure the resulting total temperature.

Kanthal Probes

For the hot free jet, alternative probes are required that can withstand the high total temperatures. Steel probes such as described above would require a cooling system [108, 117] which increases the complexity of the measurement system and reduces the overall measurement accuracy. Alternatively, materials with better heat resistance must be used as, for instance, reported by Springer et al. [159]. Here, a hybrid design with a temperature resistant silicon carbide probe tip and a water cooled support structure is used.

A high performance ferritic iron-chromium-aluminum alloy (FeCrAl alloy) distributed by the Sandvik Group under the trade name Kanthal-A1 is suggested

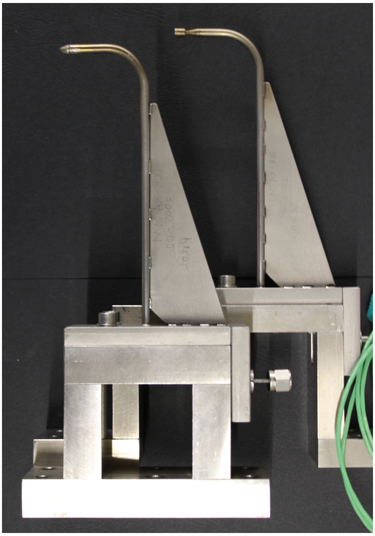

Figure A.1: Commercial pitot (left) and total temperature probes (right)

as a material for this work. Designed for electrical heating elements in industrial furnaces, Kanthal-A1 is certified for the use at temperatures up to 1673 K and has good mechanical properties even for elevated temperatures [146], which remove the need for a cooling system. Furthermore, it allows a standard manufacturing process because of the good machinability of a metallic material.

Kanthal-A1 is already available at the institute as it is used for the electrical heater system of the facility. For simplicity, the probe design is tailored to the material already available at ITLR. A second design constraint is for the probe tip to be congruent with the reference probe to minimize any deviations due to the probe's shape.

Figure A.2 shows the schematics of the two probes. For the pitot probe, the tip is turned down to an outer diameter of 5 mm and a cone identical to the DLR probe. The total temperature probe has a slightly larger head compared to its commercial counterpart as only 8 mm Kanthal tubes are available at ITLR. A type K thermocouple is inserted in the middle. A second, ceramic tube is installed to shield the thermocouple against the heat radiation of the hot Kanthal tube. Little holes in the centering parts allow the air to escape

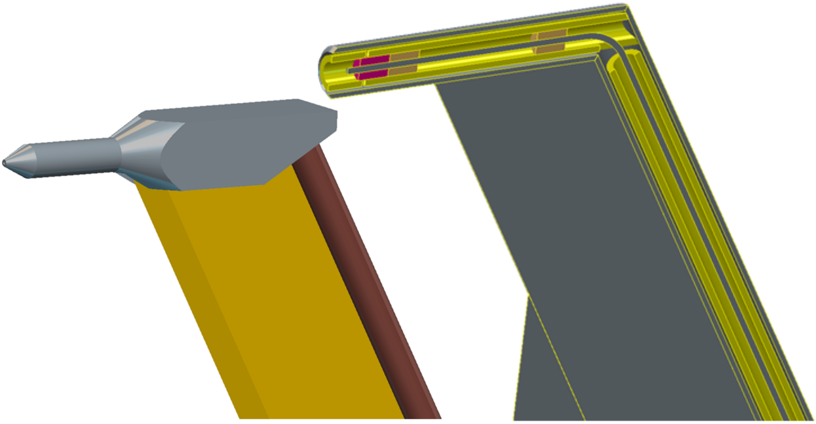

Figure A.2: Kanthal pitot (left) and total temperature probes (right)

backwards through the probe. For both probes, a support structure is made from 3 mm thick strip of Kanthal material.

The manufacturing process consists only of standard machining techniques, namely milling, turning and drilling. The material shows a brittle behavior due to its almost crystalline structure. After machining, the probes are put into a high-temperature oven to oxidize the surface of the probes, as only this oxide layer ensures the high temperature resistance of Kanthal.

For the pitot probe, a second feature of this layer is found, which makes the oxidation a compulsory step for any pressure probe made from Kanthal. After machining, the probe head is not sealed, but permeable to air. The oxide layer reduces this leakage. Eight cycles in the oven are required for the probe to be completely air-tight, resulting in a total oxidation time of 40 hours at 1200 K.

A.2 Data Processing

The pitot pressure is converted into Mach number using the Rayleigh-Pitot and isentropic flow equations for super- and subsonic flow regimes, respectively. The Mach number and the measurements of the total temperature probe can then be used to calculate the static temperature.

The air is assumed as an ideal gas with a given ratio of specific heat capacities γ. As the pressure at the nozzle is matched to the ambient pressure, the static pressure inside the jet is set to be constant and equal to the ambient pressure ($p_{static} = p_\infty$). Under these assumptions, the total pressure can be converted into the flow Mach number using the isentropic flow equation for the subsonic flow regime

$$\frac{p_t}{p_\infty} = \left(1 + \frac{\gamma - 1}{2} M^2\right)^{\frac{\gamma}{\gamma-1}} \tag{A.1}$$

and the Rayleigh-Pitot equation for the supersonic flow regime

$$\frac{p_t}{p_\infty} = \left(\frac{\gamma + 1}{2} M^2\right)^{\frac{\gamma}{\gamma-1}} \left(\frac{2\gamma}{\gamma + 1} M^2 - \frac{\gamma - 1}{\gamma + 1}\right)^{\frac{1}{1-\gamma}} . \tag{A.2}$$

A recovery factor is introduced to correct the measured temperature:

$$r = \frac{T_{meas} - T_{st}}{T_t - T_{st}} \tag{A.3}$$

Using flow Mach number and total temperature, the static temperature is derived according to the isentropic flow equation, namely

$$T_{st} = \frac{T_t}{1 + \frac{\gamma-1}{2} M^2} = \frac{T_{meas}}{1 + r\frac{\gamma-1}{2} M^2} \tag{A.4}$$

It should be noted that γ is a function of T_{st}. Typically, temperature gradients are negligible and γ is assumed constant, e.g. $\gamma = 1.4$. This is not the case for the free jets, and in particular for the hot jet, where temperature decreases significantly in radial direction through the shear layer. To avoid an additional source of error, the temperature dependence of γ is included here. As the static temperature is initially unknown, $\gamma(T_{st})$ and, hence, T_{st} is also found via the iterative process described in 4.2.3.

A.3 Uncertainty Analysis

The measurement uncertainty is based on the full scale error of the devices. A first-order Taylor series expansion of equation A.1,A.2 and A.4 is applied to account for error propagation.

Uncertainties in Mach numbers arise due to errors in the measurements of the total pressure at the probe tip and the ambient pressure. Both quantities are treated as independent and normally distributed parameters. The full scale errors are $\Delta p_t = \pm 4\,\mathrm{kPa}$ and $\Delta p_\infty = \pm 1\,\mathrm{kPa}$ for the total pressure transducer and the ambient pressure gauge.

Partial derivation of equation A.1 and A.2 with respect to both parameters yields the absolute uncertainty in the Mach number ΔM for the subsonic (equation A.5) and supersonic (equation A.6) flow regime.

$$\Delta M = \frac{1 + \frac{\gamma-1}{2} M^2}{\gamma M} \sqrt{\left(\frac{\Delta p_t}{p_t}\right)^2 + \left(\frac{\Delta p_\infty}{p_\infty}\right)^2} \tag{A.5}$$

$$\Delta M = \frac{M\left(M^2 - \frac{\gamma-1}{2\gamma}\right)}{2M^2 - 1} \sqrt{\left(\frac{\Delta p_t}{p_t}\right)^2 + \left(\frac{\Delta p_\infty}{p_\infty}\right)^2} \tag{A.6}$$

Uncertainty in the static temperature arises due to the aforementioned error in the Mach number, the measurement of the total temperature and the used recovery factor. Independent and normally distributed variation is assumed for all parameters. For the thermocouple, the tolerance class II results in an error ΔT_{meas} of $\pm 2.5\,\mathrm{K}$ or $\pm 0.75\,\%\, T_{meas}$. Uncertainty in the recovery factor is estimated to $\Delta r = 0.1$ [139]. The partial derivation of equation A.4 yields

$$\begin{aligned} \Delta\Theta &= \frac{\Delta T_{st}}{T_{st}} \qquad \text{(A.7)} \\ &= \sqrt{\left(\frac{\Delta T_{meas}}{T_{meas}}\right)^2 + \left(\frac{r\frac{\gamma-1}{2}M^2}{1 + r\frac{\gamma-1}{2}M^2}\frac{\Delta r}{r}\right)^2 + \left(\frac{r(\gamma+1)M^2}{1 + r\frac{\gamma-1}{2}M^2}\frac{\Delta M}{M}\right)^2}. \end{aligned}$$

For the supersonic core flow of the investigated free jets, the overall uncertainty of probes is $\pm 1.5\,\%$ for Mach number and $5\,\%$ for static temperature. These values remain approximately constant for all jets.

APPENDIX B

Validation of Kanthal Probes

Although the Kanthal probes mimic the geometry of the commercial probes, a separate validation is conducted to ensure that both probe sets yield interchangeable results. As the commercial probes are restricted in operation temperature, the validation is conducted for the heated free jet at an inlet total temperature of $T_t = 550\,\mathrm{K}$. This validation is an extension to the work presented in [49].

All probes are mounted on the translation table and subsequently traversed into the free jet. The same total pressure transducer was used for both pitot probes to ensure that deviations in readings are only due to the probes themselves. Radial profiles are obtained at three planes downstream of the nozzle exit at $X/D = 1$, 3 and 5, hence analogously to measurements presented in section 5.3.

Figure B.1 shows the profiles obtained for both probe sets for $X/D = 1$ and $X/D = 5$. To allow for a direct comparison, the measured quantities p_t and T_t are used instead of the derived Mach number and static temperature.

Measurements with both probe types agree well, especially for the core flow. Deviations are only found for the total temperature measured in the shear layer. This is expected as the larger probe head of the Kanthal temperature probe increases the spatial averaging of the measurement. This is further supported as the readings of pitot probes, which feature an identical geometry, match also for the shear layer region.

In terms of derived Mach number and static temperature, the deviation of Mach number and temperature is less than 1 % for the core flow at all axial positions. For the fully developed shear layer at $X/D = 5$, these values increase to 5 % and 10 %. This shows that the new Kanthal probes achieve a similar

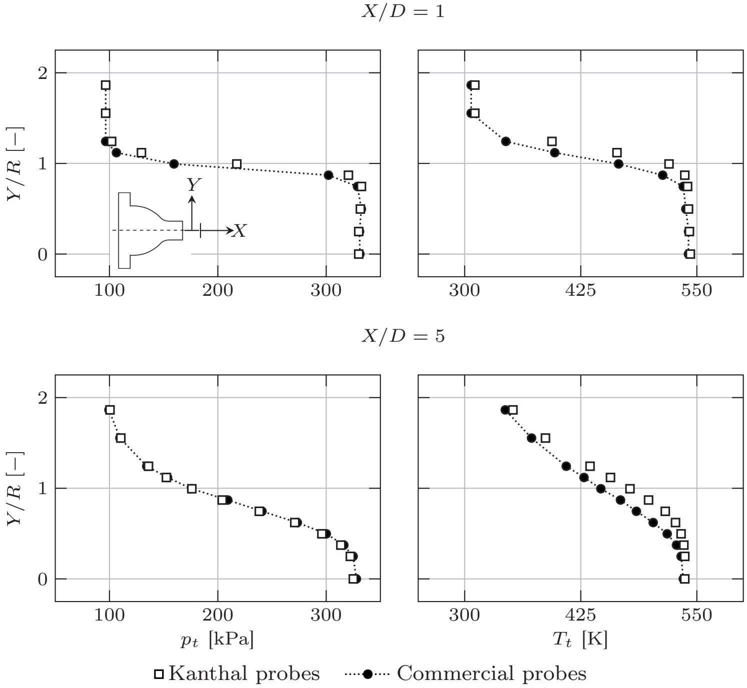

Figure B.1: Measured total pressure and total temperature at different axial positions: Comparison of Kanthal and commercial probes

performance as the commercial probes. Therefore, reference measurements for LITA are now possible for the hot jet and at the same level of confidence as for their less temperature resistant counterparts.

APPENDIX C

Additional Measurement Techniques

C.1 Pressure Measurement System

The rack mounted pressure sensor array is used for steady-state measurements. This involves total pressure measurements at the nozzle plenum and static wall pressure distribution for the test channels. Several pressure modules are available to accommodate different pressure ranges (Scanivalve Corp., DSA3016; range: 0 … 200 kPa, 0 … 700 kPa). The full scale error is ±0.05 %. To protect the pressure system from the harsh environmental conditions, it is located in a separate control room. Plastic tubes connect the pressure taps to the sensing device. Due to the length of the tubes, fast pressure changes are damped. Therefore, only steady-state measurements are feasible.

C.2 Schlieren System

Schlieren imaging allows to visualize the density gradient in the flow field, for instance due to a shock or expansion system. A schematic of the setup used is shown in figure C.1.

Light from a point source is collimated via a first convex lens. These parallel light rays pass through the test section and are focused by a second lens. The knife edge is positioned in the focal point of the second lens. The light is deflected by small variations in density as it passes the test section. Depending on the amount and angle of this deflection, the light rays are blocked by the knife edge. The passing light is recorded by the camera. The light-intensity of the resulting image reflects the variation of the density field. This conventional

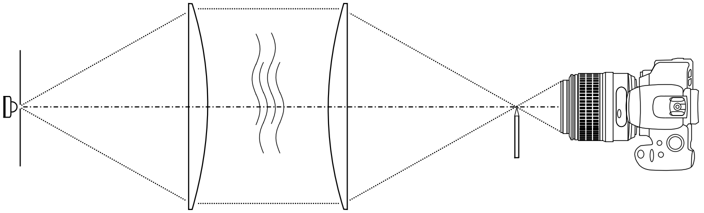

Figure C.1: Optical setup of a conventional schlieren system

setup shown here is further developed into a focusing schlieren system as described in [13, 51].

Curriculum Vitae

Felix Johannes Förster

born on the 31st of March, 1986
in Karlsruhe, Germany

Work Experience

05/2016	**Postdoctoral research associate** Department of Physics: Atomic and Laser Physics (ALP), University of Oxford, United Kingdom
05/2011 – 03/2016	**Research associate** Institute of Aerospace Thermodynamics (ITLR), University of Stuttgart, Germany
04/2012 – 10/2012	**Temporary research associate** School of Engineering and Information Technology (SEIT), University of New South Wales, Canberra, Australia
04/2008 – 04/2010	**Student research assistant** Institute of Aircraft Propulsion Systems (ILA), University of Stuttgart, Germany

Education

10/2005 – 04/2011	**University of Stuttgart** graduated as Diplom-Ingenieur in Aerospace Engineering	Stuttgart, Germany
	Durham University Research Thesis	Durham, United Kingdom
	Rolls-Royce Deutschland Internship	Dahlewitz, Germany
09/1996 – 06/2005	**Bismarck Gymnasium** Abitur	Karlsruhe, Germany